

Deterministic tunnel barriers in 1D quantum electronic systems

Inauguraldissertation

zur
Erlangung der Würde eines Doktors der Philosophie
vorgelegt der
Philosophisch-Naturwissenschaftlichen Fakultät
der Universität Basel

von

Frederick Thomas

Basel, 2020

Genehmigt von der Philosophisch-Naturwissenschaftlichen Fakultät
auf Antrag von
Prof. Dr. Christian Schönenberger
Prof. Dr. Stefano Roddaro
Prof. Dr. Szabolcs Csonka
Prof. Dr. Dominik Zumbühl

Basel, 23.06.2020

Prof. Dr. Martin Spiess
Dekan

Contents

1. Introduction	1
2. Quantum transport in mesoscopic systems	5
2.1. Quantum transport in one-dimensional quantum wires	5
2.1.1. Quasielectrons in the reservoirs	6
2.1.2. Transverse modes in the leads	7
2.1.3. Tunnel barriers as scatters	8
2.1.4. Conductance in a quantum wire	11
2.2. Quantum Dots	12
2.2.1. Single electron tunneling	12
2.2.2. Coulomb blockade diamonds	15
2.3. Double quantum dots	16
2.3.1. Double quantum dot stability diagram	18
2.3.2. Bias triangles	20
2.4. Superconductivity	21
2.4.1. Andreev reflection and the proximity effect	22
3. Indium Arsenide Nanowires and Carbon nanotubes	25
3.1. InAs nanowires	25
3.2. Carbon nanotubes	28
3.3. Summary	32
4. Device fabrication and measurement setup	35
4.1. Electrostatic gate-defined tunnel barrier devices	35
4.1.1. Carbon nanotube devices	37
4.1.2. InAs nanowire devices	39
4.2. Integrated tunnel barrier devices	41
4.3. Cryogenic measurement setup	44
5. Electrostatic gate-defined tunnel barriers in carbon nanotubes and InAs nanowires	47
5.1. Electrostatic gate-defined tunnel barriers	47
5.2. Electrostatic gate-defined tunnel barrier devices	49
5.3. Formation of tunnel barriers	49
5.4. Single quantum dots	50
5.5. Double quantum dots	51
5.6. Discussion	55

6. Integrated tunnel barriers in InAs/InP heterostructure nanowires	57
6.1. Principles of integrated tunnel barriers	57
6.2. Integrated tunnel barrier device	61
6.3. Characterization of the quantum dot	62
6.4. Resonance line shapes	64
6.5. Properties of the tunnel barriers	68
6.6. Conclusion	70
7. Spectroscopy of the local density of states in nanowire leads	73
7.1. Devices and characterization	76
7.2. Lead states	80
7.3. Lead state slopes	82
7.4. Broadening of lead states	87
7.5. Conclusion	91
8. Spectroscopy of the superconducting proximity effect	93
8.1. Device and characterization	94
8.2. Sequential tunneling regime	96
8.3. Cotunneling regime	100
8.4. Summary and discussion	101
9. Summary and Outlook	103
Bibliography	107
A. Fabrication Recipes	123
A.1. Bottom gate structures	123
A.2. Carbon nanotube stamps	124
A.3. Integrated tunnel barrier devices	126
B. Additional data of InAs/InP heterostructure nanowires with short InP segments	129
C. Additional data of InAs/InP heterostructure nanowires	131
D. Additional data of spectroscopy of the local density of states in nanowire leads	133
Curriculum Vitae	135
Publications	137
Acknowledgements	139

1 Introduction

Physics is often divided between the macroscopic world and the microscopic world. The macroscopic world contains things that we can see or touch and is governed by Newtonian physics, while the microscopic world, governed by quantum mechanics, contains the building blocks of nature such as quarks or atoms. Bridging the macroscopic and microscopic world is the mesoscopic world which addresses fundamental physical problems that arise when the dimensionality of a macroscopic object is reduced and the interaction and motion of electrons in solid materials such as metals, semiconductors, and superconductors play a crucial role. Fueled by demand for smaller and more powerful electronics from simple household appliances and electronics to quantum information technology, mesoscopic physics has become one of the most exciting forefronts of experimental physics.

One example of this are quantum bits, qubits, which are the basis of quantum information technology where the information is carried by a superposition of quantum states. Realizations of qubits in low dimensional semiconductors based on topologically protected particles [1], such as Majorana bound states [2–9] or parafermions [10–13], have been at the forefront of research over the past decade. These rely on combining one-dimensional semiconducting wires with strong spin-orbit coupling and proximity-induced superconductivity.

Two material systems that have attracted significant attention over the past two decades as possible qubit platforms are carbon nanotubes (CNTs) and III-V semiconducting nanowires (NWs). CNTs are often described by being a true one-dimensional mesoscopic system due to their exceptionally small diameters, micrometer long lengths, and variable band gaps [14, 15]. Over the past two decades, metallic and semiconducting CNTs have been used to investigate charge transport in various device architectures [16–33]. On the other hand, semiconducting NWs have received significant amount of attention due to their strong spin-orbit interaction and possibilities for scalability [34]. Significant progress has been made in the synthesis and band structure engineering of III-V semiconductor nanowires, such as InAs or InSb NWs. For example, directly grown complex nanowire geometries such as crosses [35–37] and networks [34, 38] have become feasible, as well as with in situ grown epitaxial superconducting shells [39–41] for hybrid devices [42, 43]. Furthermore, quantum

dots can be induced into nanowires by tunnel barriers that further confine the quasi one-dimensional NW. For example by electrostatic gating [42, 44–47], modification of the crystal phase [48–51], or by introducing a larger band gap material in radial [52, 53] and axial [49, 54, 55] NW heterostructures.

Several theoretical proposals suggest using quantum dots as tunnel spectrometers in hybrid systems to probe the lifetime [56, 57], parity [58], or spin texture [59] of the topological states. In ideal tunnel spectroscopy measurements, the properties of the tunnel barriers can be fully disentangled from the investigated sub-system and be directly compared to textbook transport experiments of an ideal quantum wire defined by its reservoirs, leads, and scattering regions. For this reason, tunnel barriers with deterministic properties are highly sought after and would bring one-dimensional tunnel spectroscopy measurements to the next level of control that could be used to unambiguously differentiate trivial Andreev bound states from topological states [60]. For example, energetically large and spatially well-defined tunnel barriers with a known potential profile form quantum dots that can be understood in great detail [48, 61], which then can be weakly coupled to electronic states in the nanowire leads without greatly changing their properties. Furthermore, by knowing the precise location of the quantum dot, the region over which the voltage drops in the system can be determined. For a high quality tunnel spectrometer, very narrow line widths are required in order for the resolution to not be fully determined by the features being probed. Therefore, the resolution of such a tunnel spectrometer is directly related to the tunnel barriers by how strong they confine the quantum dot.

Recent studies have shown that InAs NWs with crystal-phase defined tunnel barriers result in well-defined QDs [48], and have been used to probe the evolution of the superconducting proximity gap in an adjacent NW segment [50]. However, their relatively low and long tunnel barriers [48, 62] limit their spectroscopic range, while the large charge carrier concentrations in the zinc-blende sections make studies of few mode quantum systems challenging. Therefore, finding a suitable system with energetically larger deterministic tunnel barriers is still an on-going investigation.

Aim of this thesis

The aim of this thesis is to form large deterministic tunnel barriers in a one-dimensional system that result in spatially and energetically well-defined quantum dots for systematic tunnel spectroscopy experiments. For example, to probe quasi bound states in the lead regions coupled to normal metal and superconducting reservoirs. To tackle this problem, two types of tunnel barriers are studied in this thesis: electrostatic gate-defined tunnel barriers in CNTs and InAs NWs, and in-situ grown tunnel barriers in InAs/InP heterostructure NWs.

Outline of this thesis

Chapter 2 begins with an introduction to relevant theoretical concepts for the experiments presented in this thesis. A theoretical description of a device consisting of reservoirs, leads, and tunnel barriers is discussed in-depth. In addition, single and double quantum dots are introduced, as well as superconductivity. In **Chapter 3**, CNTs and InAs NWs are introduced as two realizations of one-dimensional semiconductors used in this thesis. For each system, their growth and electrical properties are thoroughly described. The fabrication processes and measurement setup of electrostatic gate-defined and in situ grown tunnel barrier devices is explained in **Chapter 4**. In **Chapter 5**, the results of locally tunable electrostatic gate-defined tunnel barrier devices in carbon nanotubes and InAs nanowires is presented. We demonstrate that electrostatic gates result in tunnel barriers that are energetically and spatially ill-defined making them difficult for tunnel spectroscopy measurements. **Chapter 6** takes the other approach to forming deterministic tunnel barriers by inducing band offsets in the nanowire by forming a InAs/InP heterostructure nanowire. An in-depth analysis of InAs/InP heterostructure nanowire demonstrating their broad electrical tunability, as well as a comprehensive characterization of the InP tunnel barriers, is presented. Afterwards, we implement the QD formed by the integrated tunnel barriers in an InAs/InP heterostructure NW as a tunnel probe to investigate the quasi zero-dimensional nanowire lead states coupled to normal metal and superconducting reservoirs in **Chapter 7** and **Chapter 8**, respectively. To conclude, a short summary of the thesis and outlook of possible future experiments is presented in **Chapter 9**.

2 Quantum transport in mesoscopic systems

This chapter provides the theoretical foundations for the experiments presented in this thesis. We begin with a description of an ideal one-dimensional quantum wire by taking a scattering approach to describe transport through the system. Then we introduce the physical phenomena of single quantum dots: single electron tunneling, Coulomb blockade, and Coulomb blockade diamonds. Afterwards, a brief introduction to superconductivity is presented and we conclude with transport processes at a normal-superconductor interface. This chapter serves as an introduction to quantum transport in mesoscopic systems, however interested readers should refer to Refs. [63–66] for a more thorough treatment.

2.1. Quantum transport in one-dimensional quantum wires

One-dimensional quantum wires are mesoscopic systems with diameters comparable to their Fermi wavelength, λ_F . If the length scales of the system is on the order of λ_F , the wave-particle duality of electrons becomes key and their kinetic energies in the transverse directions become quantized. In modern semiconductors, typical values of λ_F are in the range of 10 nm to 100 nm, depending on the doping. With the development of nanofabrication over the past decades, electronic devices on the scale of a few nanometers to a few micrometers can be fabricated. In this thesis, we investigate charge transport through such quasi one-dimensional electronic devices.

Quantum transport in one-dimensional quantum wires is often described by a series of scattering processes. For example, an electron impinges on a potential barrier and is either reflected or transmitted with probability T . The conductance through the system is given by the transmission of charge carriers through the system [65]. To demonstrate this, we consider a long one-dimensional rectangular semiconductor with lengths, L_x, L_y, L_z , as illustrated in Fig. 2.1(a). We assume that the wire is extended in the x-direction and energetically quantized in the y- and z-direction, i.e. $L_y, L_z \approx \lambda_F \ll L_x$.

One important quantity of a wire is how far electrons transverse the wire before being scattered described by the mean free path length, L_e . If $L_x \gg L_e$, then electrons will experience scattering events in the wire. In this limit, the quantum wire is called diffusive and electronic transport is governed by the

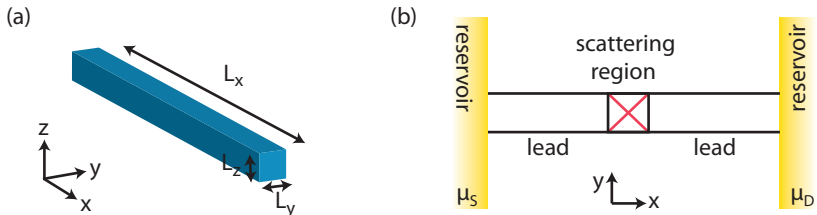


Figure 2.1. One-dimensional quantum wire: (a) Illustration of a 1D semiconductor quantum wire with length, L_x , and widths, L_y, L_z . The wire is extended in the x -direction and energetically quantized in the y - and z -direction: $L_y, L_z \approx \lambda_F \ll L_x$, where λ_F is the Fermi wavelength. (b) Structure of a two terminal one-dimensional quantum wire. Electrons travel from one reservoir (yellow) to the other via waveguide-like lead segments and are either reflected at the interface of a scattering region (red) or transmitted into the opposite lead segment. Figure adapted from Refs. [63, 64].

Drude model [65]. In the opposite limit, $L_x \ll L_e$, the system is in the so-called quasiballistic regime where electrons scatter at the boundaries of the wire and/or by diffusive processes [65].

In this section, we take a scattering approach to describe quasiballistic coherent electron transport in a one-dimensional quantum wire where the conductance can be fully described by the Landauer-Büttiker formalism [65]. An illustration of such a system is shown in Fig. 2.1(b). In view of the experiments reported in this thesis, we divide the system into three regions: the reservoirs with electrochemical potentials $\mu_{S/D}$ (Sect. 2.1.1), waveguide-like lead segments (Sect. 2.1.2), and the potential barriers as a scattering region (Sect. 2.1.3), and discuss charge transport through the system.

2.1.1. Quasielectrons in the reservoirs

Quantum transport begins with the source of charge carriers: the reservoirs. Neglecting any screening effects for large electron densities, the reservoirs are bulk metals where the electrons are confined to a crystal lattice and are made up of many electrons that interact with each other via Coulomb repulsion. However, these are not the electrons that contribute to electron transport. Instead, we focus on weakly interacting charged excitations of all the electrons in the reservoir, so-called quasielectrons or quasiparticles. This can be understood as a renormalization of the system where the interaction with the crystal is taken into account. First, consider that the reservoir is in the ground state then by adding one charge carrier, the system is driven into an excited state corresponding to the creation of one quasielectron with a quasimomentum,

spin $1/2$, effective mass m^* , and $\mu_{S/D}$.

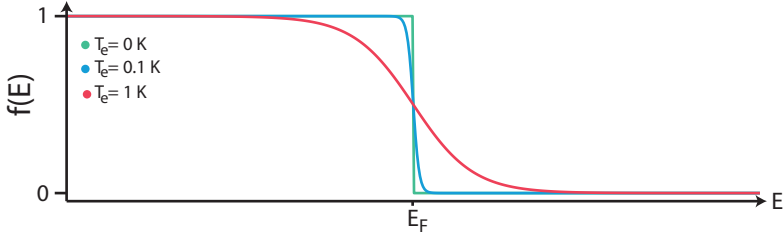


Figure 2.2. Fermi-Dirac distribution of the reservoirs: Fermi-Dirac distribution for temperature $T_e = 0$ K (green), 0.1 K (blue), and 1 K (red). Figure adapted from Refs. [63–65]

If the quasielectrons are in a thermal equilibrium state they can be characterized at a given electrochemical potential, $\mu_{S/D}$, and temperature, T_e , which is set by the Fermi-Dirac distribution [63–65]:

$$f(E) = \frac{1}{1 + e^{(E - \mu_{S/D})/k_B T_e}} \quad (2.1)$$

The Fermi-Dirac distribution for $T_e = 0$ K, 0.1 K, and 1 K is shown in Fig. 2.2. It has a value of $f(E) = 1$ for energies below μ , decays exponentially with energy, and equals $1/2$ at for $E_F = \mu_{S/D}$. The 10% - 90% width is given by $4k_B T_e$. For $T_e = 0$, it equals a step function at $\mu_{S/D}$.

2.1.2. Transverse modes in the leads

Electrons in the reservoirs then tunnel from eigenstates in the reservoirs into eigenstates of the lead segments. The leads are typically assumed to be semi-infinite waveguide-like regions of hard-wall transverse confinement between the reservoirs and the scattering region. The waveguide can be understood as impenetrable walls perpendicular to the y and z directions guiding electrons along the x -direction. Therefore, when a wave is reflected from these walls, the wave vector, $k_{y,z}$, will change sign ($k_{y,z} \rightarrow -k_{y,z}$), as illustrated in Fig. 2.3(a). Since the hard-wall confinement of the waveguides repels the electron in the transverse directions, the walls must be nodes of the standing wave. This only happens when k_y and k_z become quantized, i.e. $k_{y,z} \propto n$, where n is called the transverse mode. The wave function of an electron in the waveguide is given by: $\Psi_{k_x, n}(x, y, z) = \psi_{k_x}(x)\Phi_n(y, z)$. This gives rise to a quantization of the transverse motion of electrons. The transverse wave functions are illustrated in Fig. 2.3(a).

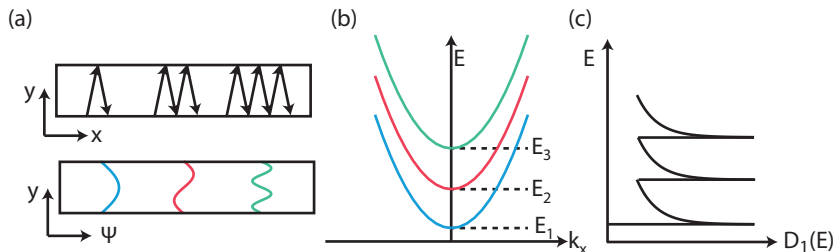


Figure 2.3. Transverse modes and density of states of a one-dimensional quantum wire: (a) Classical particle trajectories reflecting at the impenetrable walls of the rectangular waveguide and corresponding wave functions for the transverse directions. (b) Dispersion relation for three discrete parabolic subbands: E_1 (blue), E_2 (red), and E_3 (green). (c) One-dimensional density of states of the quantum wire, $D(E)$. Figure adapted from Refs. [63–65].

Along the x -direction, the electron wavefunction is not confined and forms a plane wave, $\phi_{k_x} = e^{ik_x x}$. Therefore, an electron in a given transverse mode (subband) only has one degree of freedom. This gives rise to an energy dispersion parabolic in k_x , while quantization along the y - and z -directions creates quantized energy modes of subband energy E_n . Within the channel, the dispersion reduces to n discrete parabolic subbands, $E_n(k_x)$, each with two-fold degeneracy due to spin [63–65]:

$$E_n(k_x) = \frac{\hbar^2 k_x^2}{2m^*} + E_n, \quad (2.2)$$

where m^* is the effective mass and E_n is the band bottom. The dispersion relations for $E_{1,2,3}(k_x)$ are illustrated in Fig. 2.3(b). For zero temperature, the integer number of occupied modes, M , below the Fermi energy, E_F , is given by: $M = \sum_{n=1}^N \theta(E_F - E_n)$, where θ is the Heaviside function. The density of states within this region is given by: $D(E) = \sum_{n=1}^N \sqrt{\frac{2\pi m^*}{\hbar^2}} \frac{1}{\sqrt{E - E_n}}$. This is shown in Fig. 2.3(c) for the first three subbands.

2.1.3. Tunnel barriers as scatters

As an electron is traveling between the two reservoirs, it can experience a scattering event and either be transmitted or reflected. The interaction of the electron with the scatterer during the tunneling process can be described entirely by the transmission probability per mode, $T(E)$. This is the ratio of

the outgoing probability current density on one side of the structure and the incoming probability density on the other.

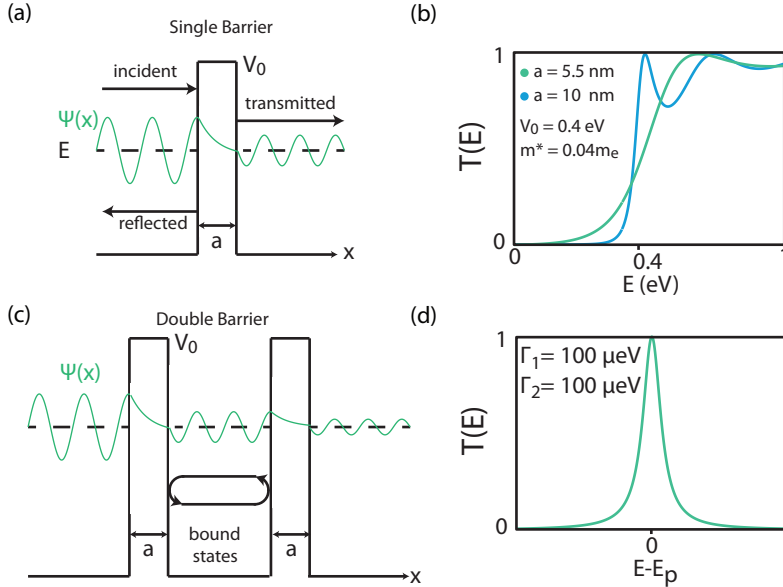


Figure 2.4. Quantum tunneling: Tunneling through a (a) single and (c) double tunnel barrier with width(s) a and height(s) V_0 . The probability amplitude of the electron wave function Ψ , with energy $E < V_0$, is exponentially reduced due to the presence of a tunnel barrier. Corresponding transmission probability, T , as a function of energy for a single (b) and double (d) tunnel barrier centered around the single particle energy E_p . Figures adapted from Refs. [63–65].

One type of scatter is a tunnel barrier. Tunnel barriers are regions of higher potential, compared to the electron energy, within the one-dimensional quantum wire that acts as a scattering region. The working principle behind tunnel barriers is quantum tunneling. Quantum tunneling is a purely quantum mechanical phenomenon where an electron, with energy E , has a nonzero probability to tunnel through a potential barrier of height, V_0 , even though $E < V_0$. In other words, the wave function of the electron extends through the potential barrier and has a finite amplitude on the opposite side. Figure 2.4(a) shows an illustration of quantum tunneling through a single tunnel barrier with finite width a and height V_0 . For simplicity, we assume that the leads on the left and right of the scattering region each consist of a single subband. An incident

particle impinges on the tunnel barrier and we would like to determine the probability that the particle tunnels through the barrier, i.e. $T(E)$. Due to the simplicity of this tunnel barrier, the Schrödinger equation can be solved for this system, resulting in [63–65]:

$$T(E) = \left[1 + \frac{V_0^2}{4E(V_0 - E)} \sinh^2(\kappa a) \right]^{-1} \quad (2.3)$$

where $\kappa = \sqrt{\frac{2m^*}{\hbar^2}(V_0 - E)}$. Figure 2.4(b) shows the relation of the transmission probability as a function of particle energy with $V_0 = 400$ meV, $a = 5.5$ nm (green) and $a = 10$ nm (blue), and effective mass $m^* = 0.04m_e$. In the case of a long tunnel barrier (blue), $T \approx 0$ for $E \ll V_0$ while $T \approx 1$ for $E \approx V_0$. This corresponds to high tunneling probability for particle energies close to the height of the tunnel barrier. However, this is different for a short barrier (green) where $T \approx 0.2$ for $E \approx V_0$ and $T(E) \approx 1$ when $E \approx 0.7 \gg V_0$. A low transmission probability, $T \ll 1$, corresponds to a high and wide tunnel barrier ($\kappa a \gg 1$). In this limit, $T \propto \exp(-2\kappa a)$. The key point is that T decays exponentially with tunnel barrier width as well as exponentially with the square root of its height V_0 . From this argument, we can deduce that the barrier decreases the amplitude of $\Psi(x)$, meaning there is a reduced, but finite, probability to find an electron on the other side of the barrier. Therefore, even though the energy of electron is smaller than the barrier height, quantum mechanics predicts that the electron can nevertheless tunnel through it with a finite probability.

By combing two tunnel barriers in series, separated by a distance, s , along the 1D system, the electron wave functions between the two tunnel barriers become confined and form quasibound states, as illustrated in Fig. 2.4(c). This is a result of self-interference of coherent electron wave functions by multiple reflections on the two barriers. This leads to a situation similar to the "particle in a box" and results in electron states with discrete energies, E_p , that are bounded between the two tunnel barriers. For $E \approx E_p$, the interference is constructive and results in the cancellation of the reflected wave to the left of the double barrier and an enhancement of the transmitted one. The transmission probability of such a system can be expressed by a Breit-Wigner function [63–65]:

$$T(E) = \frac{\Gamma_1 \Gamma_2}{(E - E_p)^2 + \frac{1}{4}(\Gamma_1 + \Gamma_2)^2} \quad (2.4)$$

where $\Gamma_i = \hbar\nu T_i$ denotes the coupling constant of barrier i with attempt frequency ν and transmission probability T_i . In the semi-classical picture, the attempt frequency $\nu = v/2s$ is the frequency at which the electron with velocity, v , hits barrier i and attempts to tunnel through. Therefore, Γ_i/\hbar represents the tunnel rate: the number of tunnel events across barrier i per

unit time. The transmission probability as a function of $E - E_p$ for $\Gamma_1 = \Gamma_2 = 100 \mu\text{eV}$ is shown in Fig. 2.4(d). At $E = E_p$, we find $T = 1$ for symmetric tunnel barriers which decays over the scale of Γ .

Tunnel barriers can be experimentally formed in many different ways: by Schottky barriers at a metal-semiconductor interface [67, 68], vacuum [69] or dielectric gap [70], by electrostatic gates (see Chapter 5), or by band offsets between different materials (see Chapter 6). They induce tunnel barriers in the one-dimensional semiconductor that the electron must tunnel through and consequently non-propagating states couple with propagating ones. This thesis tries to achieve spatially and energetically well-defined and controllable tunnel barriers that we can fully understand.

2.1.4. Conductance in a quantum wire

Now we can discuss the conductance of the quantum wire shown in Fig. 2.1(b). We first consider the case of zero temperature ($T_e = 0$). If no external voltage is applied, μ_S is aligned with μ_D and the states with positive and negative momentum are equally occupied up to the Fermi level, E_F . However, a small source-drain bias voltage, $eV_{SD} = \mu_S - \mu_D$, opens up an energy window which results in an occupation imbalance between forward and backward propagating states. The current I through the system is given by [63–65]:

$$I = e \sum_{n=1}^N \int_{\mu_D}^{\mu_S} \frac{1}{2} \rho_n(E) \nu_n(E) T_n(E) dE, \quad (2.5)$$

where $\rho_n(E) = \frac{2}{\pi} (\partial E / \partial k_x)^{-1}$ is the 1D density of states and $\nu_n(E) = \frac{1}{\hbar} (\partial E / \partial k_x)$ is the effective electron velocity. The energy dependencies of $\rho_n(E)$ and $\nu_n(E)$ cancel out resulting in a conductance $G = I/V_{SD}$ given by:

$$G = \frac{2e^2}{h} \sum_{n=1}^N T_n(E). \quad (2.6)$$

In the case of ideal transmission $T_n(E) = 1$, the conductance through the quantum wire is $G = \frac{2e^2}{h} N$ where every occupied subband contributes one conductance quantum, $G_0 = \frac{2e^2}{h}$.

The effect of finite temperature can be included by introducing the Fermi-Dirac distribution of the reservoirs (Eq. 2.1) into Eq. 2.5, resulting in:

$$G = \frac{2e^2}{h} \sum_{n=1}^N \int T_n(E) \frac{\partial f}{\partial E} dE \quad (2.7)$$

2.2. Quantum Dots

In this section, we discuss the the properties of quantum dots (QDs). QDs are semiconductor nanostructures where the motion of electrons in the conduction and valence band are confined in all three spatial dimensions. In one-dimensional systems, the electronic wave function along the radial direction is already quantized due to their small diameters. As illustrated in Fig. 2.4, by introducing two tunnel barriers into the system, a zero-dimensional island of quasibound states with a quantized energy spectrum for electrons is formed. The level spacing, δE , depends on the dispersion relation for the system, which in turn, is depends on the precise geometry of the QD.

Such nanostructures are usually very small, therefore in addition to the kinetic energy, there is also a potential energy due to the Coulomb interaction between the electrons on the island. The self capacitance of the island is small and therefore it requires a lot of energy to add an additional electron onto the island. This is called Coulomb blockade and is a universal defining feature of QD nanostructures. Quantum dots have been formed in several different types of solid state systems: electrostatic gating of two dimensional electron gases [71–73], self-assembled during growth [74–76], nanowires [6, 46–48, 50, 53, 61, 77–95], carbon nanotubes [14, 16, 18, 21, 27, 96, 97], two dimensional van-der-Waals materials [98, 99], and graphene nanoribbons [100, 101].

2.2.1. Single electron tunneling

When the island is made small enough, the Coulomb interaction between electrons is not negligible and is the dominating energy scale at low temperatures ($e^2/C \gg k_B T$). The effects of the Coulomb interactions between electrons are well described within the framework of the constant interaction model (CIM) [102]. The CIM makes two assumptions: (a) electron-electron effects do not alter the discrete energy spectrum of the QD and (b) the Coulomb interaction energy of a particle is given by a mean electric field of all other electrons, which can be described by a self-capacitance of the island, C , that is independent of the charge state. This conceptually simple model is often used to describe the physics of QDs with large electron populations, N .

Figure 2.5(a) illustrates a circuit diagram of a single QD weakly tunnel coupled to a metallic source (S) and drain (D) contact. The QD island is capacitively coupled to the source and drain reservoirs by capacitances, $C_{S/D}$, while the tunnel coupling, which allows for an exchange of particles, is described by the coupling parameters, $\Gamma_{S/D}$.

The two tunnel barriers are described by a capacitive couplings between the QD and the source and drain (D) contacts, $C_{S/D}$, with coupling strengths $\Gamma_{S/D}$. In addition, a gate electrode, with capacitance C_G tunes the electron population on the QD. The total capacitance of the island is then given by the

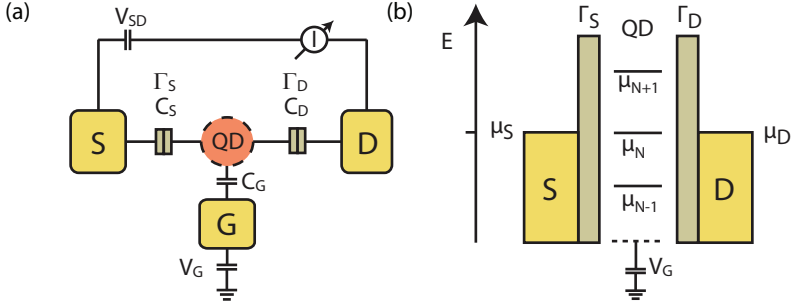


Figure 2.5. Quantum dot model: (a) Circuit diagram of a single quantum dot coupled by two tunnel barriers with capacitive, $C_{S/D}$, and tunnel coupling strengths, $\Gamma_{S/D}$, to a source (S) and drain (D) contact. A gate (G) couples capacitively with capacitance, C_G , to the QD tunes the electrochemical potential of the QD by a voltage V_G . (b) Illustration of the energy levels of a single QD with tunnel couplings $\Gamma_{S/D}$, N electrons, and electrochemical potential μ_N . Schematics adapted from Refs. [102–104].

sum over all individual capacitances: $C = C_S + C_D + C_G$. The ground state energy of the QD can be written as [105]:

$$U(N) = \frac{(Ne - Q_{\text{ext}})^2}{2C} + \sum_{j=1}^N E_j, \quad (2.8)$$

where N is the number of electrons on the QD and Q_{ext} is the voltage induced external charge on the QD given by $Q_{\text{ext}} = \sum_i C_i V_i$ with $i = S, D, G$. The first term in Eq. 2.8 is the electrostatic energy of the QD and the second term is a sum over the single particle quantum mechanical energy levels E_j of the QD due to quantum confinement.

The energy required to add the N th electron to the QD is called the electrochemical potential $\mu_N = U(N) - U(N - 1)$, i.e. the energy difference between two single particle energy levels. Combining this with Eq. 2.8 results in:

$$\mu_N = \frac{e^2}{C} \left(N - N_0 - \frac{1}{2} \right) - \frac{e}{C} \left(\sum_i C_i V_i \right) + E_N \quad (2.9)$$

This describes a ladder of energies in electron transport, as illustrated in Fig. 2.5(b). Electron transport is allowed if μ_N aligns with occupied states of the reservoirs. The difference between two consecutive electrochemical potential levels is the addition energy, E_{add} , and is given by:

$$E_{\text{add}} = \mu_{N+1} - \mu_N = \frac{e^2}{C} + \delta E, \quad (2.10)$$

where $E_C = \frac{e^2}{C}$ is the charging energy and $\delta E = E_{N+1} - E_N$ is the single particle energy spacing or level spacing. By applying a gate voltage V_G to the QD the ladder of chemical potentials can be linearly shifted positive or negative by $e\alpha_G\Delta V_G = C_G/C$, where α_G is the lever arm of the gate.

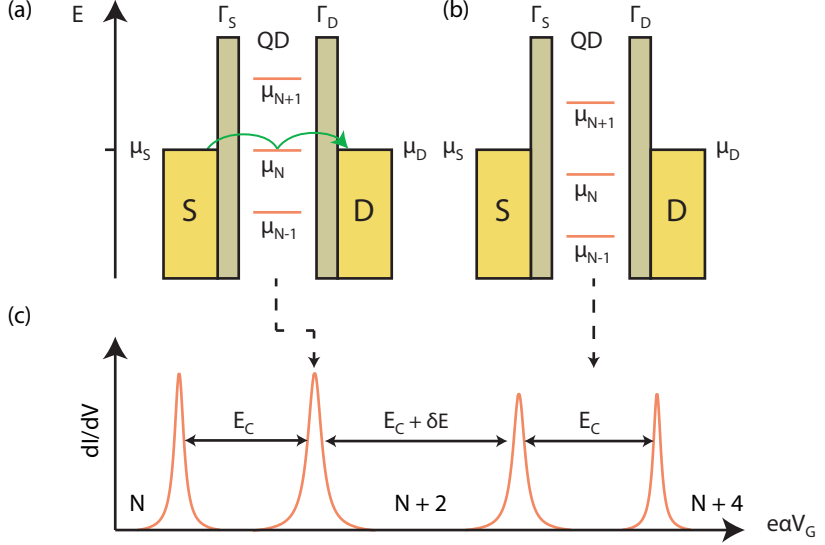


Figure 2.6. Coulomb blockade and Coulomb resonances: (a) Single electron transport is allowed via a single quantum dot (QD) energy level when the electrochemical potential of the QD is aligned with the electrochemical potential of the source and drain contacts ($\mu_N = \mu_{S/D}$). (b) Single electron transport is forbidden when $\mu_N \neq \mu_{S/D}$ and the QD is in Coulomb blockade. (c) Differential conductance dI/dV as a function of gate voltage V_G . Coulomb resonances are observed due to single electron tunneling through the QD. Schematic adapted from Refs. [102–104].

Figure 2.6 illustrates a simplified model of single electron tunneling (a) and Coulomb blockade (b) when the QD is coupled directly to metallic source and drain contacts. In (a), the electrochemical potential of the source, μ_S , and drain, μ_D , contacts are aligned with the electrochemical potential of the QD, i.e. $\mu_{S/D} = \mu_N$. In addition, in the regime, $k_B T \ll \delta E \ll E_C$, only one

energy level contributes to electron transport. This situation is referred to as single level resonant tunneling, where an electron can tunnel from the source contact onto the QD and subsequently into the drain contact. This results in a positive step-like increase in the current I for $\mu_S = \mu_D$, thus a peak in differential conductance, dI/dV . These peaks in conductance are called Coulomb blockade resonances and are illustrated in Fig. 2.6(c). Coulomb resonances are not infinitely sharp due to several effects, such as: a finite temperature of the reservoirs, how long an electron stays on the QD (lifetime broadening), and applied voltage bias. An in-depth explanation of the line shape of Coulomb blockade resonances can be found in Chapter 6.

However, if the electrochemical potential of the QD is not aligned with the electrochemical potential of the source and drain contacts, i.e. $\mu_{S/D} \neq \mu_{QD}$, electron transport is forbidden and the QD is in Coulomb blockade. Also if the level spacing is large enough that first order tunneling is not energetically favorable, the QD can be interpreted as a large tunnel barrier that the electrons cannot overcome.

In addition to Coulomb blockade resonances being separated by E_{add} , atomic-like orbitals of the QD can play a role in electron transport. The energy required for an electron to tunnel into a new orbital is $E_{\text{add}} = E_C + \delta E$, but the energy required to add the second electron to the same orbital is only $E_{\text{add}} = E_C$.

2.2.2. Coulomb blockade diamonds

Instead of applying a gate voltage to shift the electrochemical potential of the QD to be aligned with the chemical potential of the source and drain contacts to overcome Coulomb blockade, a finite source-drain bias voltage V_{SD} can also lift Coulomb blockade. This is done by opening a large enough bias window, $-eV_{SD} = \mu_S - \mu_D$, such that μ_N enters the bias window, such that Coulomb blockade is lifted and an increase in conductance is observed. By measuring the differential conductance dI/dV as a function of gate voltage V_G and source-drain bias voltage V_{SD} we observe a periodic pattern called Coulomb blockade diamonds [102], as illustrated in Fig. 2.7. In this thesis, we assume asymmetric voltage biasing, meaning the drain is kept grounded ($\mu_D = 0$) and the voltage is applied to the source contact ($\mu_S = -eV_{SD}$).

The boundaries of the Coulomb diamonds, which mark the onset of charge transport, are determined when the chemical potential of the QD is aligned with either the source or drain contact ($\mu_N = \mu_{S/D}$). When the slope of the diamond edge is positive, indicated by β_+ , the chemical potential of the QD is aligned with the source contact ($\mu_{QD} = \mu_S$), as shown in Fig. 2.7 III. In comparison, when the slope of the diamond edge is negative, indicated by β_- , the chemical potential of the QD is aligned with the drain contact ($\mu_{QD} = \mu_D$), as shown in Fig. 2.7 II. At the tip of the Coulomb diamond (Fig. 2.7 I), the

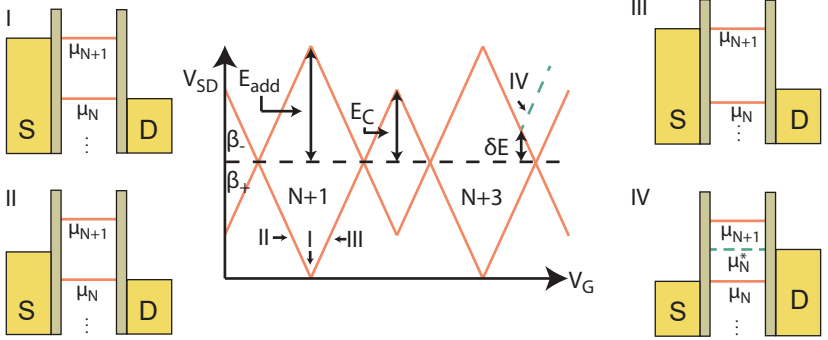


Figure 2.7. Coulomb blockade diamonds: Differential conductance dI/dV as a function of source-drain bias voltage V_{SD} and gate voltage V_G . Coulomb blockade diamonds with two fold symmetry. The energy diagrams represent different biasing conditions indicated in the Coulomb diamond schematic. Schematic adopted from Refs. [102–104, 106–108].

bias voltage is a direct measurement of the addition energy E_{add} . If a two-fold periodicity in the Coulomb diamonds is observed, this can be used to extract E_C and δE by measuring the height of two sequential Coulomb diamonds.

From the slopes of the Coulomb diamonds, β and β_+ , the gate lever arm α_G and all capacitances C_i can be determined. When the electrochemical potential of the QD is aligned to the drain ($\mu_{\text{QD}} = \mu_{\text{D}} = 0$) the slope will be negative and one finds from Eq. 2.9: $0 = -|e|\frac{C_G}{C} \Delta V_G - |e|\frac{C_S}{C} \Delta V_{SD}$. Therefore, we obtain $\beta = -\frac{C_G}{C_S}$. From the positive slope, we can similarly determine $\beta_+ = \frac{C_G}{C - C_S}$. From β and β_+ , the lever arm can be expressed as [65]:

$$\alpha_G = \frac{\beta_+ |\beta_-|}{\beta_+ + |\beta_-|} \quad (2.11)$$

Within the Coulomb diamond, the QD is in Coulomb blockade, therefore the conductance in this region is zero. However, outside of the Coulomb diamond, the electron number on the QD changes. This is due the chemical potential(s) of one or more energy levels lies within the source-drain bias window.

2.3. Double quantum dots

By introducing a third tunnel barrier in the system, two regions along the wire become energetically confined and two QDs in series are formed, known as a serial double quantum dot (DQD). For an additional QD in series, an extra

tunneling event takes place between one quantum state to another quantum state. This dot-to-dot transition is governed by selection rules based on quantum numbers such as spin and valley [109].

Fully tunable DQDs require at least five gates: three gates to form tunnel barriers and two gates to adjust the electron population on each QD. A serial DQD system can be modeled by either an electrostatic circuit diagram or quantum mechanically by a tunnel coupling between the two QDs, as shown in Fig. 2.8(a) and (b), respectively. The electrostatics are described by the Poisson equation, which we approximate by capacitances leading to the circuit diagram, and the transport and confinement by quantum mechanics.

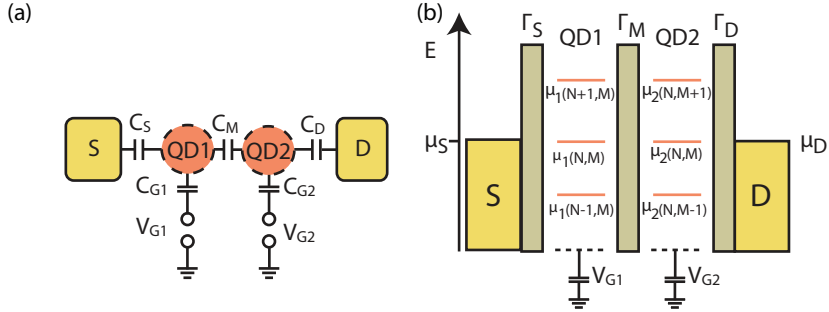


Figure 2.8. (a) Electrostatic circuit diagram of a double quantum dot (DQD): The left quantum dot, QD1, is capacitively coupled to the source (S) with capacitance, C_S , and to gate G1 with capacitance, C_{G1} , by a gate voltage V_{G1} . Similarly, the right QD, QD2, is capacitively coupled to the drain (D) contact with capacitance, C_D , and to gate G2 with capacitance, C_{G2} , by a gate voltage V_{G2} . The two QDs are coupled via a mutual capacitance C_M . (b) Electrochemical potential diagram of a DQD. The electron population on QD1 and QD2 is denoted as N and M , respectively. The electrochemical potentials of QD1, μ_1 , and QD2, μ_2 , are tuned by a voltage, V_{G1} and V_{G2} , applied to gates G1 and G2, respectively. QD1 is tunnel coupled to the source contact with coupling strength, Γ_S , and QD2 is tunnel coupled to the drain contact with coupling strength, Γ_D . QD1 and QD2 are mutually tunnel coupled with coupling strength, Γ_M . Figure adapted from Ref. [109].

First, we consider the case of the electrostatic circuit model where only the discreteness of the electron charge is taken into account. The electron population on QD1 is denoted as N and the electron population on QD2 is denoted as M . QD1 is capacitively coupled to gate G1 with capacitance C_{G1} by a gate voltage V_{G1} , as well as capacitively coupled to the source (S) contact with capacitance, C_S . Similarly, QD2 is capacitively coupled to gate

QD2 with capacitance C_{G2} by a gate voltage V_{G2} , as well as capacitively coupled to the drain (D) contact with capacitance, C_D . In addition, QD1 and QD2 are mutually coupled with capacitance, C_M .

In the quantum mechanical model, the QDs have discrete energy spectrums due to confinement. QD1 and QD2 are tunnel coupled to the source and drain contacts with coupling strengths Γ_S and Γ_D , respectively. In addition, the QD1 and QD2 are mutually coupled with coupling strength Γ_M . The electrochemical potential to add an electron onto QD1 with $N - 1$ electrons is denoted as $\mu_1(N, M)$, where M is the number of electrons on QD2. Likewise for QD2, $\mu_2(N, M)$ denotes the electrochemical potential to add an electron onto QD2 where N is the number of electrons on QD1. Therefore, resonant tunneling through the DQD system is only allowed when all of the electrochemical potentials are aligned, i.e. $\mu_S = \mu_1 = \mu_2 = \mu_D$. For finite bias, the condition for transport is given by: $\mu_S \geq \mu_1 \geq \mu_2 \geq \mu_D$ [109].

We now only consider the electrostatic picture where the two QDs being capacitively coupled and neglect quantum mechanical effects. The total capacitance of QD1(QD2), $C_{1(2)}$, is given by: $C_{1(2)} = C_{S(D)} + C_{G1(G2)} + C_M$. Cross capacitances between V_{G1} and QD2 and between V_{G2} and QD1 are neglected. We consider transport through the system for small bias voltages, $V_{SD} \approx 0$ and assume that there are only 1 or 0 electrons on QD1 or QD2.

2.3.1. Double quantum dot stability diagram

A double quantum dot stability diagram shows the charge configuration, (N, M) , of the two QDs as a function of V_{G1} and V_{G2} . The stability diagram also allows for a qualitative description of each of the quantum dots total capacitance and gate capacitance, as well as their addition energies [109]. The charge stability diagram depends on the electrostatic interaction between QD1 and QD2. Here, this is governed by C_M in this electrostatic model. Figure 2.8(a)-(c) shows the charge stability diagram for three different regimes: two fully decoupled QDs ($C_M \approx 0$), two weakly interacting QDs ($0 < C_M < C_{1(2)}$), and two strongly coupled QDs ($C_M \approx C_{1(2)}$).

First we consider the case of two decoupled QDs, $C_M \approx 0$, where electron transport through one QD is independent of the other QD. A schematic of this situation is shown in Fig. 2.9(a). To enable transport through QD1, μ_1 and μ_2 need to be aligned into bias window and to each other. Similarly for QD2, this condition must be satisfied. Therefore, $V_{G1}(V_{G2})$ changes the charge on QD1(QD2) without influencing QD2(QD1). These two processes are independent of each other leading to a charge stability diagram that takes the shape of rectangular pattern where transport is allowed at the intersecting points indicated by black points, called triple points. Electrons travel through the DQD system subsequently, resulting in two possible charge transfer processes: (1) $(1, 0) \rightarrow (0, 1) \rightarrow (0, 0) \rightarrow (1, 0)$ or (2) $(1, 0) \rightarrow (0, 1) \rightarrow (1, 1) \rightarrow (1, 0)$.

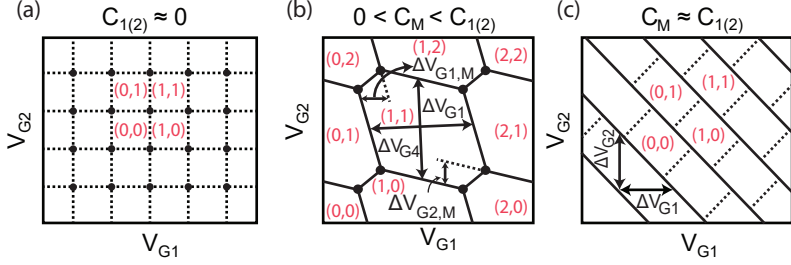


Figure 2.9. Double quantum dot stability diagrams: (a) Two fully decoupled quantum dots for $C_M \approx 0$ where transport occurs at the intersecting points indicated by black dots. (b) Increasing C_M causes a weak electrostatic interaction between the two QDs and the stability diagram evolves into a honeycomb pattern. The degeneracy points in (a) begin to split due to electrostatic interactions and form so-called triple points. The dimensions of the honeycomb pattern, ΔV_{G1} and ΔV_{G2} , can be related to the gate capacitances, C_{G1} and C_{G2} , while the shift of the triple points is related to C_M . (c) For larger C_M , the electrostatic interaction between the two QDs becomes strong and the system acts as an effective single QD. Figure adapted from Ref. [109].

For two strongly coupled QDs, these processes are degenerate.

However, this degeneracy is lifted if the two QDs are not completely decoupled and there is a small electrostatic interaction between them such that $0 < C_M < C_1, C_2$. Now there is an energetic difference between charge transfer process (1) and (2). This splits the degenerate triple points in Fig. 2.9(a) into triple points that are energetically separated. This separation between the triple points is governed by C_M . In addition, the stability diagram evolves into a honeycomb pattern, as illustrated in Fig. 2.9(b), reflecting the electrostatic interaction between the two QDs. Within one honeycomb cell the total charge on the DQD is constant. The dimensions of a honeycomb cell can be related to the gate capacitances by:

$$C_G = e/\Delta V_G, \quad (2.12)$$

where ΔV_G is the spacing. In addition, the shift of the triple points, $\Delta V_{G1(2),M}$, can be related to C_M by:

$$C_M = C_{1(2)} \cdot \Delta V_{G1(2),M}/\Delta V_{G1(2)} \quad (2.13)$$

If the electrostatic interaction between the QDs is further increased such that $C_M \approx C_1, C_2$, the two QDs will effectively form a single QD. The resulting charge stability diagram is shown in Fig. 2.9(c). Charge transport is allowed

when $E_{\text{add}}(N) = \alpha(V_{G1} + V_{G2})$, assuming equal coupling between the QD and the two gates. Therefore, the stability diagram consists of diagonal resonances when $V_{G1} = -V_{G2} + E_{\text{add}}(N)/\alpha$.

2.3.2. Bias triangles

So far, we considered transport processes for small V_{SD} , but now we consider the case of a finite bias $|V_{SD}| > 0$. Therefore, we need to keep in mind the electrochemical potential diagram shown in Fig. 2.8(b). We assume that the bias is applied to the source contact and the drain is grounded. For a finite bias, $\mu_S > \mu_D$, the triple points expand into larger triangular shaped regions, called bias triangles, as seen in Fig. 2.10. The dimensions of the bias triangle, δV_{G1} and δV_{G2} are given by [109]:

$$C_{1(2)} = \frac{C_{G1(2)}}{|eV_{SD}|} \cdot \delta V_{G1(2)} \quad (2.14)$$

Therefore by combining Eq. 2.12, 2.13, and 2.14, C_1 and C_2 , as well as C_M can be extracted from the DQD stability diagram.

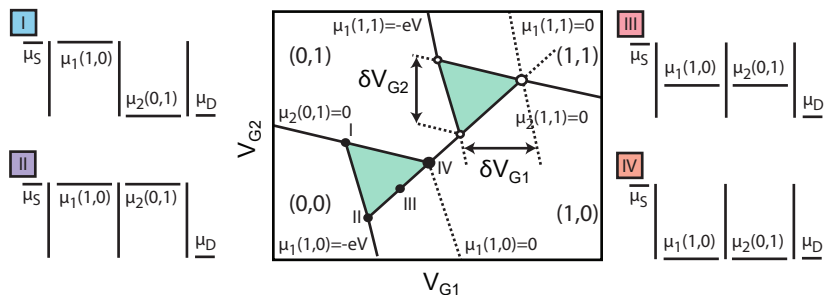


Figure 2.10. Transport through a DQD at finite bias voltage: For a finite bias voltage $|V_{SD}| > 0$, the triple points in Fig. 2.9(b) expand into bias triangles where transport is allowed through the DQD. The dimensions of the bias triangles, δV_{G1} and δV_{G2} , can be used to extract the total capacitance of QD1 and QD2. The electrochemical potential diagrams (I)-(IV) show a schematic of the electrochemical potential energies for the source contact (μ_S), QD1 (μ_1), QD2 (μ_2), and the drain contact (μ_D) at the boundaries of the bias triangle. Figure adapted from Ref. [109].

Within the bias triangle electrons can freely travel through the DQD, assuming that the energy relaxation of the QDs is fast or have a dense spectrum of excited states. The boundaries of the bias triangles are determined by the

constraints: $-|e|V_{SD} \geq \mu_1$, $\mu_1 \geq \mu_2$, and $\mu_2 \geq \mu_D$, indicated by the electrochemical potential diagrams (I)-(IV). To describe this, we follow the transport process between points (I) and (IV). At (I), the electrochemical potentials are given by $\mu_S = \mu_1 > \mu_2 = \mu_D$, thus transport is allowed. Following the border of the bias triangle between (I) and (II), V_{G2} is decreased, therefore μ_2 increases until $\mu_S = \mu_1 = \mu_2 > \mu_D$. Within this region transport is also allowed. If V_{G2} would decrease even further, then $\mu_2 > \mu_1$ and transport would be prohibited. Going from (II) to (III), both V_{G1} and V_{G2} are simultaneously increased, therefore μ_1 and μ_2 are decreased. Since $\mu_S > \mu_1 = \mu_2 > \mu_D$ holds, transport along this line is allowed until (IV) $\mu_S > \mu_1 = \mu_2 = \mu_D$ [109].

2.4. Superconductivity

In this section, we discuss the principles of superconductivity and the effects it has on electron transport in one-dimensional systems. Previously, we discussed single electron transport where electrons tunnel through the QD sequentially. However, in superconductors transport is mediated by electron pairs, i.e. Cooper pairs. This creates a competition of transport mechanisms when a superconductor is coupled to a QD. This interplay of single electron and Cooper pair transport mechanisms results in a rich field of hybrid devices where Cooper pair splitting [47, 81, 85, 93], Andreev bound states [17, 110, 111], and Majorana bound states [6, 7, 9, 42, 86] can be observed.

Superconductors are a class of materials whose electrical resistance vanishes below a critical temperature T_C , in comparison to a normal metal where the resistance decreases as a function of temperature. In a superconductor at a temperature above T_C , the electrical resistance behaves similarly to a normal metal. However, below T_C the material undergoes a phase transition into the superconducting state where the electrical resistance is zero. The first microscopic theory of superconductivity was developed in 1957 by Bardeen–Cooper–Schrieffer (BCS theory) [112], who received the Nobel prize later for their work. BCS theory can be thought of that at low temperatures, i.e. below T_C , the Fermi distribution of electrons become unstable against any net attraction. This instability results in two electrons pairing into Cooper pairs which do not follow typical Fermi-Dirac statistics, but rather Bose-Einstein statistics. The origin of the attractive potential resulting in the formation of Cooper pairs is attributed to electron-lattice interactions, however BCS theory only requires an attractive potential regardless of its origin [112]. Cooper pairs can be continuously formed from two single electrons until an equilibrium state is achieved where further pairing does not lower the energy anymore. Since Cooper pairs have total spin 0, they form a coherent bosonic ground state that can be described by a macroscopic wave function.

BCS theory further demonstrates that excitations from the ground state

to unpaired electrons (quasiparticles) requires an energy of 2Δ , where Δ is the superconducting order parameter. One can interpret this as the amount of energy to break a Cooper pair. This results in the excitation spectrum of the superconductor to have a gap of 2Δ around the Fermi level E_F . The quasiparticles energy dispersion is then given by: $E(k_x) = \sqrt{\epsilon(k_x)^2 + \Delta^2}$, where $\epsilon(k_x) = \frac{\hbar^2 k_x^2}{2m} - E_F$ is the kinetic energy of a free electron with respect to E_F [113]. From the quasiparticle dispersion relation, the density of states (DOS) of the quasiparticles can be determined and reveals a gap of size 2Δ [114]:

$$D_S(E) = D_N(\epsilon) \frac{d\epsilon}{dE} = \begin{cases} D_N(\epsilon) \cdot \frac{E}{\sqrt{E^2 - \Delta^2}}, & \text{if } |E| > \Delta. \\ 0, & \text{if } |E| < \Delta. \end{cases} \quad (2.15)$$

where D_N is the normal state DOS and is assumed to be constant. From Eq. 2.15, we clearly see that there is a gap of Δ around E_F separating the quasiparticles. If there is no tunnel barrier in the system then for subgap energies $|E| < \Delta$, the quasiparticle DOS is zero and transport is mediated only by Cooper pairs. At $|E| = \Delta$, the quasiparticle DOS diverges and for higher energies $|E| \gg \Delta$ the DOS recovers to the normal state DOS.

2.4.1. Andreev reflection and the proximity effect

In this section, we discuss the effects of electron transport at a normal - superconductor (N-S) interface, as illustrated in Figure 2.11(a) and (b). The normal metal (N) has a constant DOS, while the superconductor (S) has a superconducting gap of 2Δ .

Now we assume that an electron from the normal metal impinges on the N-S interface. If the electron has a subgap energy $|E| < \Delta$, transport through the interface is prohibited since no quasiparticle states are available at this energy and cannot form a Cooper pair at E_F . In addition, for the electron to be reflected at the interface, a momentum transfer of $2p_F$ is required. However, the tunnel barrier of height Δ formed by the superconducting gap can only transfer a momentum of $\delta p = \Delta/v_F$ which is orders of magnitude smaller than $2p_F$ [116]. To circumvent this problem, a higher order process called Andreev reflection (AR) must be considered [117]. In AR, the impinging electron is retro-reflected as a hole with opposite spin and momentum. The electron and hole form a Cooper pair in the superconductor and a total of $2e$ is transferred across the interface.

A theoretical description of such transport across an N-S interface is well described by Blonder-Tinkham-Klapwijk (BTK model) [115]. The BTK model describes the scattering potential at the N-S interface by a delta potential $V(x) = Z\hbar v_F \delta(x)$ with a dimensionless barrier strength Z . For $Z = 0$, no

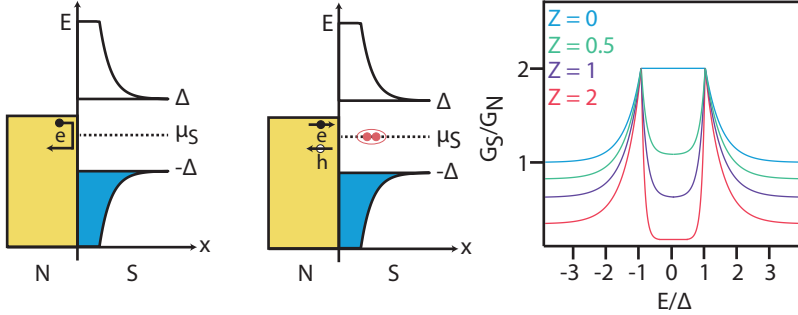


Figure 2.11. Schematic of reflection of an incident electron at an N-S interface for elastic scattering (a) and (b) Andreev reflection. (c) Normalized differential conductance G_S/G_N as a function of the superconducting gap Δ for an N-S interface based on the BTK model at $T = 0$ for different $Z = 0$ (blue), $Z = 0.5$ (green), $Z = 1$ (purple), and $Z = 2$ (red). Adapted from [103, 115].

scattering events take place and transport through the N-S interface is governed by AR for electrons with $|E| < \Delta$, as shown in Fig. 2.11(b). This results in an increase of the current by a factor of 2. Experimentally, $Z \neq 0$ due to a Fermi velocity mismatch between the two materials and elastic scattering at the N-S interface, as shown in Fig. 2.11(a). Therefore, AR becomes suppressed for increasing Z and the quasiparticle DOS begins to be observed in the superconductor for $|E| > \Delta$. The normalized differential conductance $S = G_S/G_N$ as a function of Δ for different Z values is shown in Fig. 2.11(c).

The time reversed process should also be considered. A Cooper pair can be removed from the superconductor condensate by an incoming hole and retro-reflected electron. The hole and AR hole remain phase correlated up to some distance in the normal metal and there is a non-zero probability to find a Cooper pair in the adjacent normal metal. The density of Cooper pairs decays continuously as a function of distance inside the normal metal. For a metal, this distance is on the order of the BCS coherence length ξ .

This means that the superconducting properties of the superconductor leak into the normal metal. This is called the proximity effect where the superconductor *proximitizes* the adjacent material. The reverse situation where the density of Cooper pairs is reduced in the superconductor by an adjacent normal metal is possible. This is called the inverse proximity effect.

3 Indium Arsenide Nanowires and Carbon nanotubes

In this chapter we introduce two realizations of one-dimensional quantum wires discussed in Chapter 2: indium-arsenide nanowires (InAs NWs) and carbon nanotubes (CNTs). Both systems are natural one-dimensional semiconductors due to their small diameters (few to tens of nanometers) compared to their long lengths (few microns). Furthermore, we present the growth mechanisms and electronic properties of InAs NWs and CNTs.

3.1. InAs nanowires

Semiconductor nanowires are promising one-dimensional systems for scalable electronic devices and for investigating fundamental physics on the nanometer scale. For example, they are used as possible hosts of Majorana fermions [4, 6, 42, 58, 86, 118–122] and entangled electrons [81, 93] as building blocks in topological quantum computation [5, 9, 56, 120], as well as in the fields of spintronics [123–125], magnetotransport [88, 126, 127], and thermoelectrics [128]. In addition, they are also widely used outside the realm of electron transport, such as: sensors [129–133], solar cells [134–138], and light emitting diodes [139]. InAs nanowires offer several unique characteristics such as their small band gap [140], low effective mass [141], large and tunable g-factor [46, 142, 143], high mobility [144–146], and strong spin-orbit interaction [51, 125, 147].

Nanowire growth

The main growth technique of semiconducting nanowires is based on bottom up vapor-liquid-solid (VLS) methods [148]. This includes: chemical vapor deposition (CVD) [149], molecular beam epitaxy (MBE) [150], chemical beam epitaxy (CBE) [55, 151, 152], and metal-organic vapor phase epitaxy (MOVPE) [153, 154]. The working principle behind each of these processes is similar, relying on the accumulation of gaseous atomic or metal-organic precursors inside of a metallic catalyst particle, however they mainly differ by how the gas is fed to the catalyst particle. A typical material choice for the catalyst particle of metal-assisted InAs NW growth is gold due to its inertness

to oxygen [155]. Gold particles can be randomly formed on a substrate either by: direct deposition [156], metal evaporation and subsequent annealing [157], randomly deposited using aerosol techniques [158], or by first pre patterning arrays by electron beam lithography and subsequent gold evaporation [159].

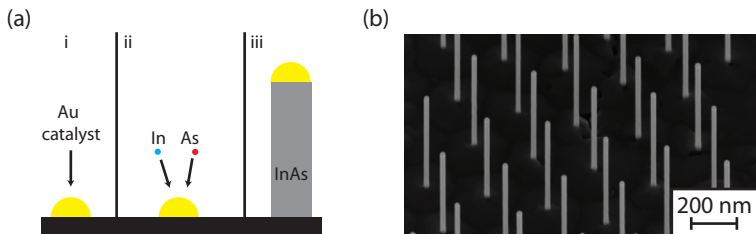


Figure 3.1. InAs nanowire growth: (a) Illustration of the vapor-liquid-solid growth process of InAs nanowires. (i) Predefined gold catalyst particles (yellow) are formed on the InAs(111)B substrate (black). (ii) In (blue) and As (red) are fed to the gold catalyst to initiate the growth of InAs (grey). (iii) The gold catalyst supersaturates and begins to grow. (b) Transmission electron microscope (TEM) image of InAs/InP heterostructure nanowires on the growth substrate. TEM image courtesy of Lucia Sorba. Figure adapted from Refs. [104, 106, 160].

During the growth process, the diameter, length, and crystal phase of the InAs NW can be fully controlled. The diameter of the NW is determined by the size of the gold catalyst particles. The length of the NW is dependent on the growth time. Despite bulk InAs exhibiting a zincblende crystal phase, typically the wurtzite crystal phase is observed in nanowires since the crystal phase is highly dependent on the nanowire diameter [161]. However, single crystal zincblende InAs can be realized in NW systems under the right growth conditions [48, 49, 162].

The InAs NWs discussed in this thesis are synthesised by VLS growth in a CBE chamber by Lucia Sorba (NEST Pisa). The growth process is illustrated in Fig. 3.1(a). A thin gold film is evaporated onto an epitaxial InAs(111)B substrate, then undergoes a thermal annealing step inside of the growth chamber to initiate the formation of randomly distributed gold nanoparticles with a diameter of 40 nm to 50 nm (i) [157]. Next, trimethylindium (TMIn) and tert-butylarsine (TBAs) are introduced into the system to initiate the growth of InAs (ii). The TMIn and TBAs feed the gold catalyst particles until they supersaturate and begin to grow (iii). This procedure has been shown to produce defect-free crystalline wurtzite InAs NWs [55]. The resulting growth chip consisting of a "forest" of InAs NWs is shown in Fig. 3.1(b).

Significant progress has been made in the bandstructure engineering of III-V semiconductor NWs. For example, directly grown complex multiple NW geometries such as crosses and networks have become feasible [35–38], as well as in situ grown epitaxial superconducting shells [39–41] for superconducting hybrid devices [6, 42, 43, 163]. In addition, heterostructure and core-shell InAs nanowires have been successfully realized in a variety of systems [48, 164–168]. One prime example are InAs/InP heterostructure nanowires where two short in-situ grown InP segments are implemented into the InAs NW during growth [54, 55, 61]. An in-depth description and analysis of InAs/InP heterostructure nanowires can be found in Chapter 6, as this is one of the main work horses of this thesis.

Electronic properties

InAs nanowires are an n-type III-IV semiconductor composed of indium (In) and arsenide (As) atoms. As illustrated in Fig. 3.2(a), the InAs NWs discussed in this thesis exhibit a hexagonal wurtzite crystal structure with a lattice constant of 4.25 Å where the In and As atoms are covalently bonded [169–171]. Figure 3.2(b) illustrates the band structure around the Γ point in the Brillouin zone. The conduction (CB) and valence (VB) band are separated by a small direct semiconducting band gap, $E_g = 477$ meV [140]. The conduction band around the Γ point can be approximated by a parabola with an effective mass $m^* = 0.04m_e$, where m_e is the mass of a free electron, assuming a wurtzite InAs crystal phase [141].

Electron transport takes place mainly at the surface of the InAs NW due to the accumulation of electrons at the surface of the NW that pins the Fermi level 200 meV above the conduction band [172, 173]. This makes InAs NWs very sensitive to any surface treatment [175–178] and electrostatic gating effects [179], however it also allows for easy electrical contact to the NW [180]. One-dimensional ballistic transport and control over the number of one-dimensional subbands have been observed in InAs NWs [181]. The spin-orbit interaction strength in InAs NWs has been found to be 250 μ eV and vectorial control over it has been demonstrated [51, 147, 182, 183]. Strong SOI and ballistic transport in one-dimensional semiconductors are necessary in the formation of a helical gap; a spin-orbit induced Zeeman gap essential for the creation of topological superconductors with induced Majorana bound states. The first signatures of a helical gap in an InAs NW have been reported by Heedt et. al. [184].

Due to their small diameter, the electron wave function is constrained in the radial direction. As discussed in Sect. 2.1.2, the electron states become quantized and form transverse modes. To visualize the transverse modes in an InAs NW, we assume a hexagonal confinement potential and numerically solve the Schrödinger equation using Matlab 2D finite element solver for the

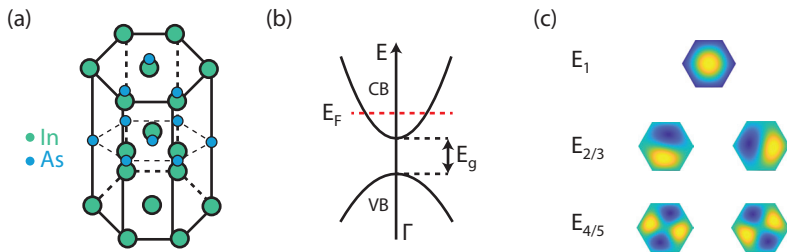


Figure 3.2. Properties of InAs nanowires: (a) In (green) and As (blue) form an InAs wurtzite crystal structure with a lattice constant of 4.25 \AA . (b) Electron band structure around the Γ point. The conduction (CB) and valence (VB) band are separated by a small band gap $E_g = 477 \text{ meV}$ [140]. The Fermi level, E_F is positioned 200 meV above the conduction band [172, 173]. (c) Analytically calculated wave functions of the five lowest subbands for a nanowire with hexagonal confinement. We find orbital degeneracies between E_2 and E_3 and between E_4 and E_5 . Figures adapted from Refs. [106, 174].

wave functions. The wave functions of the lowest five subbands are shown in Fig. 3.2(c). The main difference compared to a parabolic confinement potential is the subband energy spacing. In Sect. 2.1.2, we showed that the subband spacing is constant for rectangular confinement. Now, it is possible to have additional orbital energy degeneracies, for example, between E_2 and E_3 and between E_4 and E_5 .

3.2. Carbon nanotubes

Single-wall carbon nanotubes (CNTs) are often referred to as a prime example of a one-dimensional semiconductor due to their extremely small diameters on the scale of (1 nm to 2 nm) and micron long lengths [14, 185]. CNTs are a highly versatile material system with highly sought after electronic, thermal, and mechanical properties that have been used over the past two decades to investigate transport processes such as: quantum dots [16, 18, 21, 22, 27, 30, 97, 186–188], spin transport [31, 32, 189, 190], Andreev bound states [17, 33, 191–195], and Cooper pair splitting [93, 196]. Metallic CNTs with uncorrelated electrons are a perfectly ballistic system with room temperature mean free path length of a several hundreds of nanometers [197, 198]. Furthermore, CNTs also exhibit semiconducting features with a band gap inversely proportional to its diameter, allowing for easily tunable electron and hole charge carrier transport [19, 199]. In addition, CNTs synthesized from ^{13}C atoms have been proposed as hosts of helical spin-ordering where the electrons and nuclear spins

of the system become helically ordered for temperatures below a few millikelvin [200]. CNTs are extremely stiff with tensile strengths in the tens of gigapascals without significant weight [201, 202].

All of these properties aspects make CNTs a fascinating system to study fundamental one-dimensional physics, as well as industry driven aspects of CNTs. This section serves as an introduction to single-wall carbon nanotubes starting from their growth and the basis of graphene to their electronic properties.

Carbon nanotube growth

The most common method of CNT synthesis is via chemical vapor deposition (CVD), as illustrated in Fig. 3.3(a). A substrate is prepared with a layer of metallic nanoparticles and catalyst support particles mixture. The substrate is then placed into the center of the CVD oven and heated to a growth temperature set by the nanoparticle/catalyst mixture. A precursor hydrocarbon gas is then passed through the CVD oven and into a bubbler. Due to the high temperature, the metal nanoparticles initiate the decomposition of the hydrocarbon and the growth of CNTs.

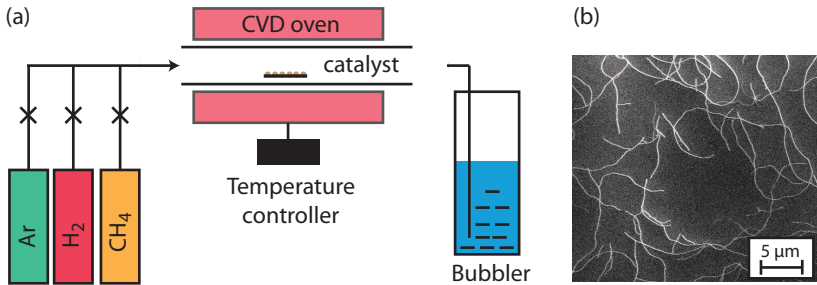


Figure 3.3. Carbon nanotube growth: (a) Typical chemical vapor deposition setup for carbon nanotube growth. (b) Scanning electron microscope image of carbon nanotubes after growth. Figure adapted from Refs. [103, 203, 204].

In this thesis, we implement a recipe developed by Jürg Furer during his PhD that produces reliable, high quality, and a large yield of single-wall CNTs [203, 205]. We use iron/molybdenum (Fe/Mo) catalyst dissolved in IPA [206]. A few mL of this solution is sonicated in a high power sonicator to breakdown the iron clusters and form a homogeneous solution. Directly following the sonication, the catalyst solution is spin-coated onto a substrate and placed into the center of a CVD oven. Subsequently, the CVD oven is heated to a growth temperature of 1100 °C under a constant argon/hydrogen (Ar/H₂)

flow. Once at the growth temperature, the flow of H_2 is stopped and replaced with methane (CH_4) for 10 min to initiate the growth of CNTs. Afterwards, the CVD oven is cooled to $\sim 200^\circ C$ under a constant Ar/H_2 flow.

Electronic properties

Carbon nanotubes are understood as rolled up sheets of graphene. Therefore to understand CNTs, we begin the discussion with the band structure of graphene. Graphene is a two dimensional monolayer of graphite consisting of carbon atoms with 6 electrons each. Two electrons occupy the inner $1s$ shell and are tightly bound to the nucleus, while the other four electrons occupy the $2s$ and $2p$ orbitals. These four electrons are weakly bound to the nucleus and form four bonds; one σ bond with its three neighbors and one π bond in the z -direction [207].

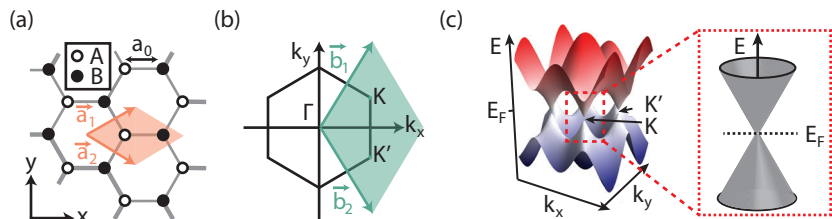


Figure 3.4. Graphene lattice and bandstructure: (a) Honeycomb pattern of graphene in real space with lattice constant $a_0 = 1.42 \text{ \AA}$. The primitive unit cell consists of A and B atoms formed by basis vectors \vec{a}_1 and \vec{a}_2 . (b) First Brillouin zone of the honeycomb lattice with reciprocal lattice vectors, \vec{b}_1 and \vec{b}_2 . (c) Tight binding calculation of the electronic band structure of graphene [207]. (inset) Zoom-in of the charge neutrality point. Figure adapted from Refs. [207–209].

As shown in Fig. 3.4(a), the six carbon atoms are arranged in the well-known 2D hexagonal honeycomb lattice with lattice constant, $a_0 = 1.42 \text{ \AA}$. The primitive unit cell containing two atoms, A and B, is formed by two basis vectors, \vec{a}_1 and \vec{a}_2 , which span one unit cell consisting of two carbon atoms. The corresponding first Brillouin zone of the honeycomb lattice with reciprocal lattice vectors, \vec{b}_1 and \vec{b}_2 , is shown in Fig. 3.4(b). The reciprocal lattice vectors given by the condition: $\vec{a}_i \cdot \vec{b}_j = 2\pi\delta_{ij}$. This creates two inequivalent set of valleys, K and K' , at the six corners of the Brillouin zone [207].

Figure 3.4(c) shows a tight binding calculation of the electronic band structure of graphene by taking into account only nearest neighbor hopping [207]. At the valleys, K and K' , the conduction and valence band meet and are com-

monly referred to as Dirac points or charge neutrality points since the Fermi energy, E_F at this intersection is zero. The linear dispersion relation near the Dirac points is given by:

$$E(q) = \pm \hbar v_F(q), \quad (3.1)$$

where $q = k - K$ or $q = k - K'$ for $|q| \ll |K|$ and $v_F \approx 8 \times 10^5$ m/s is the Fermi velocity [199, 207]. Therefore, graphene is known as a zero bandgap semiconductor, or semi-metal, with zero density of states (DOS) at the Dirac points. Dirac cones, as shown in the inset of Fig. 3.4(c), are the low energy approximation around K and K' . This gives rise to a new degree of freedom called valley-spin or isospin [199, 207].

Figure 3.5(a) illustrates the rolling up process to form CNTs from a single sheet of graphene. The resulting CNT has a cylindrical structure with a diameter, d , of 1 nm to 5 nms [210]. However, if the CNT is made up of several sheets of graphene, it forms a so-called multi-wall carbon nanotube (MWCNT) and can have diameters up to 20 nm [210]. The structure of the CNT is characterized by the chiral vector, \vec{c} , given by: $\vec{c} = n\vec{a}_1 + m\vec{a}_2$, where n and m are integers and $n \leq m$. There are three different sets of CNTs that are defined by n and m : zig-zag, armchair, and chiral CNTs. When $m = 0$, the edge forms a so-called zig-zag pattern. An armchair CNT forms when $n = m$ and the edge forms a so-called armchair. Other variations of n and m form chiral CNTs.

The electronic band structure of a single-wall CNT can be calculated by applying a zone-folding approximation [199]. In this approximation, the axial component of the momentum along the CNT axis, k_{\parallel} , remains unaffected and continuous. However, the perpendicular component of the momentum along the circumference of the CNT, k_{\perp} , becomes quantized with step size given by the condition: $\Delta k_{\perp} \pi d = 2\pi$. Thus, the one-dimensional dispersion relation for CNTs is a cut of the Dirac cone along k_{\perp} , leading to one-dimensional subbands with a dispersion relation given by:

$$E^l(k_{\parallel}) = \pm v_F \sqrt{(k_{\parallel})^2 + (k_{\perp}^l)^2}, \quad (3.2)$$

where l denotes the subband with a quantized momentum component, $k_{\perp}^l = k_{\perp}^0 + k\Delta k_{\perp}$. As shown in Fig. 3.5(b) and (c), we observe that the CNT can either be metallic or semiconducting depending on k_{\perp}^0 . If $k_{\perp}^0 = 0$, the lowest subband cuts through the Dirac point and the linear dispersion relation with zero bandgap and constant DOS is preserved. Therefore, the CNT has a metallic structure. However, if $k_{\perp}^0 \neq 0$, the Dirac point is missed and a bandgap of $E_g = 2\hbar v_F k_{\perp}^0$ is opened. In this case, the CNT has semiconductor properties with a one-dimensional DOS.

The origin of the metallic and semiconducting CNTs is the formulation of periodic boundary conditions and is governed by the chiral indices, n and m . The periodic boundary conditions of the electrons' wavefunctions are given by:

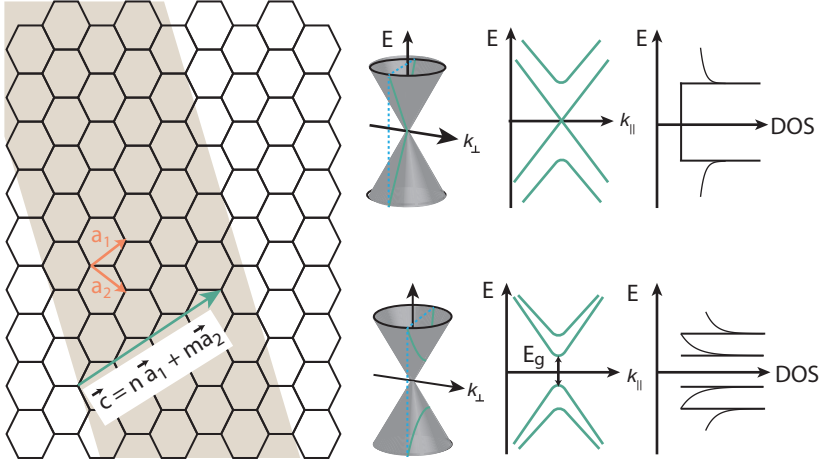


Figure 3.5. CNT lattice and bandstructure: (a) Honeycomb pattern of graphene where the brown area is rolled up into a carbon nanotube with chirality vector \vec{c} . (b)-(c) Quantization of k_\perp along the circumference of the carbon nanotube leads to 1D subbands. (b) If $k_\perp = 0$, then the lowest subband cuts through the Dirac point leading to a metallic band structure and a finite density of states. (c) If $k_\perp \neq 0$, then the lowest subband does not cut through the Dirac point and a band gap E_g is opened where the DOS is zero. Figure adapted from Ref. [103, 107, 211, 212].

$$\phi(r + c) = e^{ic(k+K)}\phi(r) = \phi(r) \quad (3.3)$$

Here, $c \cdot K = 0$ holds if $(n - m) = 3l$ and the CNT is metallic. However, if $(n - m) \neq 3l$, thus $c \cdot K \neq 0$, the lowest subband misses the Dirac point by $\Delta k_\perp^0 = \frac{2}{3d}$. This causes a bandgap to form with size inversely proportional to the CNT diameter, i.e. $E_g = 2\hbar v_F k_\perp^0 = \frac{4\hbar v_F}{3d} \approx 0.7 \text{ eV/d[nm]}$. A CNT with these chiral indices is therefore semiconducting. Following this approach, two-thirds of all CNTs should be semiconducting while only one-third are metallic.

3.3. Summary

In this chapter, the fundamental structural and electronic properties of InAs nanowires and carbon nanotubes were presented. Both materials offer unique advantages to study one- and zero-dimensional electron transport. Carbon nanotubes are often thought of as a true one-dimensional system due to the

possibility of transport via a single electronic mode due to their very small diameters and unusually long mean free paths, that is crucial in understanding, for example, Andreev bound states that form in the system, whereas InAs NWs have a larger diameter and multiple modes contribute to transport. Another major difference is where current propagates: in CNTs it is along the circumference and in InAs NWs it propagates along the surface of the NW due to Fermi level pinning. Selectively grown individual single-wall carbon nanotubes has yet been realized, however InAs NWs can be readily grown on prepatterned templates in a well-controlled manner. In addition, several types of InAs NWs can be in-situ grown, such as core-shell and heterostructure NWs, allowing for in-situ band modification. Carbon nanotubes have an extra orbital degeneracy, valley and spin, that allows for richer physics. In addition, CNTs often have a narrow band gap, leading to the possibility to study electron and hole transport, whereas in InAs NWs this regime is energetically inaccessible. InAs nanowires offer strong spin-orbit interaction with a large g-factor that are crucial ingredients of topological based quantum computation and is not present in CNTs. Because to this, they have been in the forefront of topological quantum computation due to being promising host materials for Majorana bound states.

4 Device fabrication and measurement setup

This chapter first focuses on the fabrication process of the carbon nanotube (CNT) and nanowire (NW) devices presented in this thesis. Afterwards, the experimental measurement setup used in this thesis is discussed. In the following sections, the most important fabrication steps are presented. However to completely fabricate one device, several techniques are used that are not discussed in this thesis: electron beam lithography (EBL), reactive ion etching, optical mask aligner, metalization with electron-gun and thermal sources, as well as standard wet etch methods. More information about the standard EBL process can be found in several PhD theses within our group [103, 106, 108, 208, 211]. For the exact fabrication recipes discussed in this chapter, please refer to the Appendix A.

4.1. Electrostatic gate-defined tunnel barrier devices

In this section, we discuss the fabrication of carbon nanotube (CNT) and indium-arsenide (InAs) NW devices with electrostatic gate-defined tunnel barriers that are presented in Chapter 5.

Bottom gate base structures

For electrostatic gate-defined tunnel barrier CNT and NW devices, we incorporated a grid of bottom gate structures, as shown in Fig. 4.1(a)-(c). To reduce the risk of gate leaks due to the substrate oxide breaking down, we used an undoped silicon wafer with 170 nm SiO₂ capping layer. The wafer is then diced into 2.5 x 2.5 cm pieces using a quartz-tipped scribe and the smaller pieces undergo a cleaning consisting of 15 min sonication in acetone, 15 min sonication in isopropanol (IPA), then 5 min UV ozone treatment to remove the organic surface residues using oxygen radicals.

Afterwards, a very thin 80 nm resist was spin-coated onto the undoped substrate and subsequently placed on a hot plate for 3 min at 180 °C to harden. The thin resist helps to reduce the amount of undercut during EBL, however it also limits how much metal can be evaporated and still have a proper liftoff.

The main challenge of thin and short bottom gate structures is combating the proximity effect during the EBL, where the electrons scatter a small

distance at the surface of the resist. This results in the unexposed resist between each individual gates to also become cross-linked. After development and metalization, this section will also be covered in metal and all of the gates will be shorted. To combat this, a very precise and reproducible fabrication method must be implemented. A series of dose tests with different acceleration voltages were performed to obtain the most optimal line dose with minimal proximity effect.

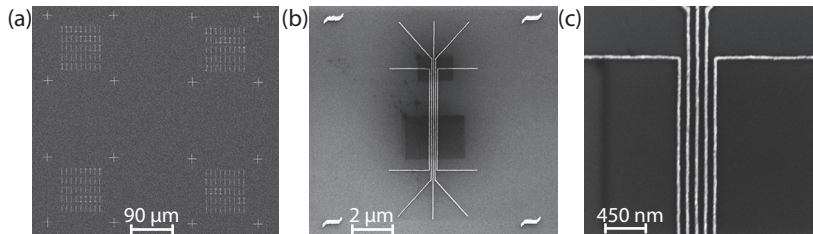


Figure 4.1. Bottom gate base structures: (a) Layout of the bottom gate chip with large alignment markers and an 8x8 grid of bottom gate structures within them. (b)-(c) One of the bottom gate structures within the 8x8 grid. The bottom gate has five 30 nm metallic strips with a pitch of 100 nm.

The bottom gates were fabricated using standard EBL with an acceleration voltage of 20 keV, high current mode, and a line dose of 1460 $\mu\text{C}/\text{cm}$. The chip was then developed in methyl isobutyl ketone (MIBK) at -15°C . The low temperature was achieved by placing the beaker with the developer inside of a bath consisting of dry ice and IPA. Afterwards, the chip was exposed to a O_2 plasma to remove any resist residues and subsequently metallized with a bilayer of titanium/gold.

Figure 4.1(a) shows an outer 2x2 grid structure of alignment markers. Inside this this grid, there is another 8x8 grid of bottom gate structures. One example of a bottom gate structure can be seen in Fig. 4.1(b). The bottom gate structure is made of up five 30 nm wide strips of Ti/Au with a center-center(pitch) distance of 100 nm, as shown in Fig. 4.1(c). The total width of the bottom gate structure where the gates are parallel is 450 nm.

In order to prevent the CNTs to directly contact the bottom gate structure, an insulating layer must be placed on top of the gate structures to electrically isolate them. In this thesis, we implemented a high quality 50 nm thick Si_3N_4 layer as our insulating material. The Si_3N_4 layer was deposited using plasma-enhanced chemical vapor deposition (PE-CVD) externally at the Paul Scherrer Institute (PSI) by Christoph Wild. The process is performed at 300°C , thus making it difficult to use any kind of resist mask. Therefore, the

Si_3N_4 layer was evaporated on the entire substrate.

We use these electrostatic gates to modify the potential along either a CNT or NW. However, the CNT or NW must be placed on top of the gate structure and subsequently metallized. In the following, we discuss the further fabrication steps that are unique to each system.

4.1.1. Carbon nanotube devices

First, we focus electrostatic gate-defined tunnel barrier CNT devices which differ in their growth, placement, and metallization steps.

Carbon nanotube stamps

Now that we established the base structure, we introduce the method which we use to transfer the CNTs to the base structure. We implement stamping technique that was developed and optimized by Thomas Hasler [211, 212]. Carbon nanotube stamps are $50\ \mu\text{m} \times 50\ \mu\text{m}$ large and $4\ \mu\text{m}$ tall pillar-like structures on which CNTs are grown. Then one presses the stamp chip with CNTs and the bottom gate chip together. This mechanically transfers the CNTs from the stamp to the bottom gate chip. The position of the CNTs are random, however due to the amount of CNTs that are transferred and the number of bottom gate structures are on device chip, it is likely that one lies on top of the predefined bottom gates.

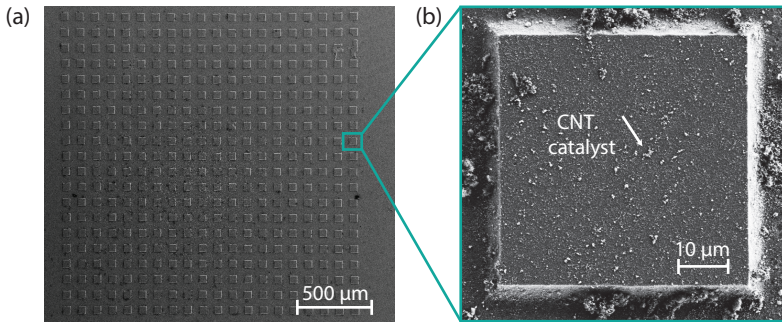


Figure 4.2. Carbon nanotube stamps: (a) Large mesa structure of silicon pillar-like structures. (b) Zoom-in of one pillar where the catalyst from the CNT growth can be seen.

The stamps are fabricated on an undoped silicon wafer with a 170 nm SiO_2 capping layer. In order to achieve the pillar-like structure, as shown in Fig. 4.2(a-b), we utilize a bilayer resist of poly(methyl methacrylate) (PMMA)

and hydrogen silsesquioxane (HSQ). We first spin-coat a $\sim 1\ \mu\text{m}$ thick PMMA layer and let it bake for 3 min at $180\ ^\circ\text{C}$. Then we spin-coat a thin layer of HSQ. After standard EBL to create the mesa structure, the chip is developed for 25 s in tetramethylammonium hydroxide (TMAH). Since HSQ is a positive resist, the HSQ development in TMAH only removes the unexposed HSQ and the PMMA remains everywhere.

Afterwards, a three step etching is performed to create the pillar-like structure. First, the PMMA that is not covered by the HSQ is removed with an O_2 plasma. Then the SiO_2 layer, and all remaining HSQ, is removed by a hydrogen fluoride (HF) wet etch. Subsequently, we etch deep into the silicon using a sulfur hexafluoride (SF_6) plasma and remove the rest of the PMMA on the pillars with acetone. Following this, the desired mesa structure of a square grid of SiO_2 pillar-like structures with a size of $50\ \mu\text{m}$ and height of $4\ \mu\text{m}$ is obtained.

Stamping technique

Afterwards, we grow CNTs directly on top of the CNT stamps using the method presented in Sect. 3.2. After the growth is complete, the CNTs on the stamp need to be transferred to the device chip. This is done by using an optical mask aligner. The CNT stamp is glued to a transparent glass slide using PMMA and mounted in the mask aligner. By using the optical microscope for alignment, the device chip is placed directly underneath the CNT stamp and the stamp is lowered until they press against each other. This causes the CNTs from the stamp to be mechanically transferred to the device chip. Figure 4.3 shows a device chip after being stamped with CNTs. The outline of the meso structure of the stamp can be clearly seen from the catalyst particles and CNTs being transferred. This technique usually results in a 3 – 4 straight CNTs to lie across the bottom gates structure. Afterwards, the device chip is imaged in an SEM and the CNTs are precisely localized.

Continuously stamping the device chip with the CNT stamp results in a rapidly decreasing yield. However, the stamps can be reused by wet etching them in HF. This removes $\sim 10\ \text{nm}$ of the SiO_2 pillars and all of the CNTs and dirt particles. Afterwards, new CNT catalyst can be applied to them again and the growth procedure can be performed again.

Metallization

All that there to do now is to electrically contact the gates and the CNT by a process called metallization. In order to contact individual gates, a window in the Si_3N_4 must be etched to make the gates accessible. The windows were created by standard EBL and the Si_3N_4 within the window was etched using a CHF_3/O_2 plasma. Afterwards, the device undergoes another EBL step to

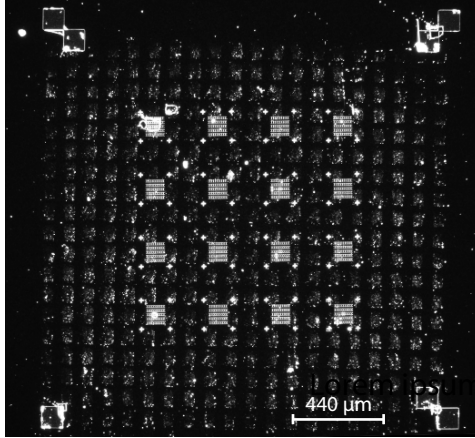


Figure 4.3. Bottom gate base structures after CNT stamping: Optical microscope image of the device chip after stamping. The imprint of the meso structure of the stamp chip with CNTs on the device chip with a grid bottom gate structures can be seen.

open windows in the resist where the individual gates as well as the CNT/NW will be metallized. In this thesis, we use a Ti/Au bilayer.

4.1.2. InAs nanowire devices

Now we swap to electrostatic gate-defined tunnel barrier InAs NW devices that use the same base structure and discuss the two main differences: the placement of NWs and their metallization.

Placement of nanowires

For electrostatic gate-defined InAs NW devices, the NW is placed directly on top of a bottom gate structure using a micromanipulator. The micromanipulator consists of two glass needles with tapered ends that are controlled by a hydraulic system, allowing for precise pickup and placement of NWs onto the bottom gate structure that could otherwise not be achieved by other techniques. The NW is first selectively picked up from the growth chip using a fine tipped glass needle. Due to the van der Waals force between the tip and the NW, the NW will become stuck to the glass tip. Once taken, the NW can easily be transferred to a bottom gate structure on one of the base structures.

Sulfur passivation and metallization

Now that the NW is on top of the bottom gate structure, the gates and NW need to be electrically contacted. The gates are electrically contact similarly to CNTs: by first etching away the SiN_3 to expose the gold gates. However, electrically contacting a NW not the same as a CNT. In order to make ohmic contact to the NW, the NW must first be striped of its 2 nm to 3 nm native oxide. This is done by first using standard EBL to open windows in the resist where the NWs native oxide will be etched and subsequently metallized. Sulfur passivation is a wet etch method where the device chip is submerged into a diluted ammonium polysulfide:water solution, $(\text{NH}_4)_2\text{S}_x:\text{H}_2\text{O}$, which in addition to etching the nanowires native oxide, also creates a monolayer of sulfur atoms that locally dopes the NW [213]. The InAs NWs presented in this thesis have a wurzite crystal phase which has shown to have an intrinsically low carrier concentration [214, 215], therefore the local doping is beneficial to achieve ohmic contact to the NW. Since sulfur passivation is a wet etch method, it must be performed in a cleanroom and cannot be done directly in the evaporation chamber. This means that the NW will be exposed to air during the time between the wet etch and evaporation chamber. If this time is long enough (~ 5 min), it is possible that the passivation layer will disintegrate and the NW will reoxidize. In practice, this means running from the cleanroom to the evaporator as quickly as possible. After sulfur passivation. the NW is then metallized with either a Ti/Au.

Conclusion

Figure 4.4 shows a false colored SEM image of a typical electrostatic gate-defined CNT device that is the end result of the fabrication steps presented in this section. A CNT (red) is stamped on top of five (G1-G5) electrical bottom gates (light blue) that are covered by Si_3N_4 (black).

To make electrical contact to the bottom gates, a region of Si_3N_4 above the bottom gates was etched (dark contour). Consequently, the CNT and each bottom gate was contacted by a Ti/Au (gold) metallization process. These types of devices were designed to form single and double quantum dots by electrostatic gating. Each of the five bottom gates (G1-G5) serves a unique purpose. The two outer gates, G1 and G5, are used to form tunnel barriers at each end of the CNT. G2 and G4, are used to tune the electron population on each quantum dot individually. The middle gate, G3, is to form another tunnel barrier in the center, therefore modifying the coupling between the two quantum dots.

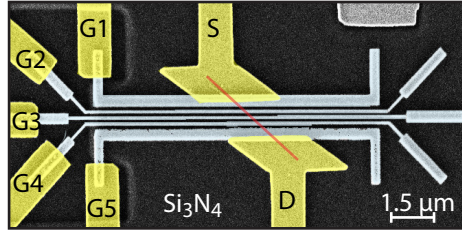


Figure 4.4. Typical CNT device: Scanning electron microscope image of a typical carbon nanotube (CNT) device. The CNT (red) is deposited using the stamping method onto a grid of 5 bottom gates (light blue) that are covered by Si_3N_4 (black). The dark contour is an etched region where the Si_3N_4 was removed to make electrical contact to the bottom gates (G1-G5). The CNT and the bottom gates are contacted using Ti/Au (yellow).

4.2. Integrated tunnel barrier devices

Next, we discuss the fabrication of indium-arsenide/indium-phosphide (InAs/InP) heterostructure nanowire devices that are presented in Chapter 6.

Substrate preparation

The InAs/InP heterostructure NW devices presented in this thesis were fabricated on a highly p-doped (boron) silicon wafer. The silicon wafer is capped with a 400 nm thick layer of thermally grown silicon oxide (SiO_2). The insulating SiO_2 capping layer also serves as a gate oxide for a global backgate. Further wafer preparation is the same as in Sec. 4.1.

Base structure fabrication

First, standard EBL was used to create a marker grid such that the nanowires can be easily and precisely localized. As shown in Fig. 4.5, the base structure consists of two sections: the outer structure (a) and the inner structure (b-c). The outer structure consists of the the bond pads and the leads connecting the inner structure to the bond pads. The inner structure is an area of $500\ \mu\text{m} \times 500\ \mu\text{m}$ consisting of a grid of unique small alignment markers with a spacing of $20\ \mu\text{m}$, as shown in (c). After EBL exposure, the structure is developed and metallized with a Ti/Au bilayer.

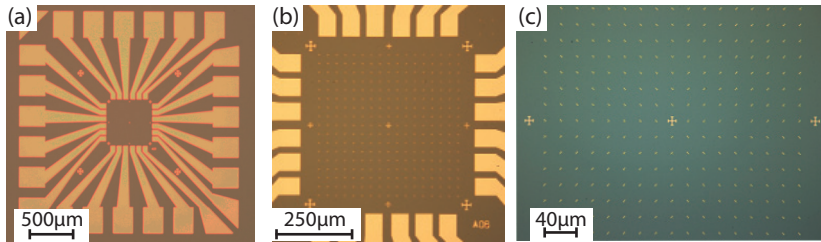


Figure 4.5. Integrated tunnel barrier device base structure: Optical microscope images of the outer (a) and inner (b)-(c) sections of the base structure. (a) The outer contacts and bond pads of the base structure can be seen. (b)-(c) The inner structure of the base structure where the grid of unique small markers is shown.

Nanowire placement and readout

The InAs/InP heterostructure NWs were grown on a separate substrate, as discussed in Sect. 6.1. To transfer the NWs from the growth chip to our prepatterned base structure, we used the tip of a cleanroom tissue. First, we cut the tissue into a small triangle that has a sharp tip, then carefully touch the growth chip that is full of densely packed NWs with the sharp tipped triangular cleanroom tissue. NWs break off from the growth chip and attach to the tip of the cleanroom tissue. By gently touching the base structure with the tip of the cleanroom tissue that is covered in NWs, the NWs will be transferred from the tissue to the base structure. Afterwards, the chip is once again cleaned using a sequence of Acetone/IPA/UV ozone treatment to remove particles from the cleanroom tissue and clumps of densely packed nanowires.

In order to precisely locate individual NWs, we image the base structure with an scanning electron microscope (SEM). Figure 4.6 shows an example of a localized SEM image of a nanowire. From the unique small markers that the NW is positioned within, the exact location of the NW on the base structure is known. It is important to note that not only the position of the NW is important, but also on which end of the NW the gold catalyst is positioned. This is due to the position of the InP segments being defined by the distance from the gold catalyst. We find the distance from the gold catalysis to the first InP segment is ~ 440 nm. In addition, we find that the InP segments are each ~ 6 nm long separated by ~ 20 nm of InAs. These values are consistent with the transmission electron microscopy (TEM) study performed by Valentina Zannier on several NWs from this growth batch.

Using a python program developed by Olivier Faist, we can readout the unique markers and the NW position from the SEM images and export the

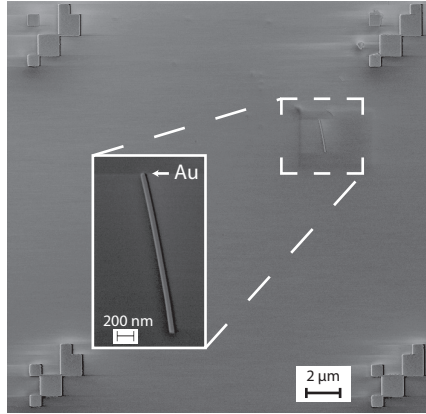


Figure 4.6. Nanowire readout: Scanning electron microscopy (SEM) image of an individual nanowire within four unique markers used for nanowire readout. (inset) High resolution SEM image of the nanowire and the gold catalyst indicated by the white arrow.

NW position into our design program (Elphy). From there, the electrical contacts and gates can be designed for the specific device.

Nanowire metallization

As with InAs NWs, InAs/InP heterostructure NWs have a 2 nm to 3 nm native oxide that must be removed prior to metallization. We implement a wet etch sulfur passivation step, as discussed in detail in Sect. 4.1.2. After sulfur passivation, the NW is then metallized with either a Ti/Au bilayer for normal metal contacts or a titanium/aluminum (Ti/Al) bilayer for superconducting contacts.

Conclusion

Figure 4.7 shows a false colored scanning electron microscope (SEM) image of a typical InAs/InP NW device that is the end result of the fabrication steps presented in this section. The InAs NW, with two short InP segments indicated by white arrows, is electrically contacted with two Ti/Au (gold) contacts. In addition, the doped substrate (black) acts as a global back gate which electrostatically tunes the conduction band edge in the NW.

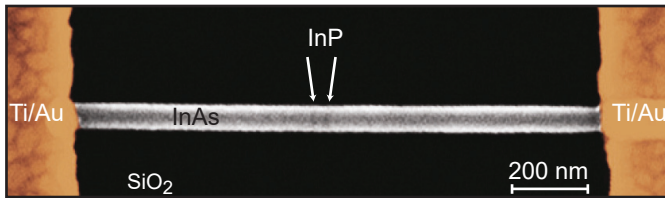


Figure 4.7. Typical integrated tunnel barrier device: False color scanning electron microscope image of a typical InAs/InP heterostructure device. The InAs/InP heterostructure nanowire is contacted with two metal contacts (gold). The two InP segments are indicated by the white arrows. The SiO₂ substrate (black) acts as a global back gate.

4.3. Cryogenic measurement setup

Low temperatures are crucial in the observation of quantum mechanical effects, such as the formation of quantum dots and superconductivity. In order to observe quantum dots, the thermal energy of the electrons has to be significantly lower than the charging energy, E_C , and single particle level spacing, δE , of the quantum dot. In addition, if the quantum dot is coupled to a superconductor, the thermal energy of the electrons must be lower than the superconducting gap, Δ , of the material. These energies are mostly above 400 μeV range. The lowest electronic temperatures in our lab are ~ 50 mK. This corresponds to ~ 4 μeV which is two orders of magnitude lower than the superconducting gap of aluminum.

By placing the sample into liquid ^4He , one can cool the sample down to 4.2 K. By pumping on the surface of the liquid ^4He , the latent heat is removed due to evaporation and the temperature of the liquid ^4He lowers to ~ 1.4 K. However, to reach even lower temperatures, such as in the mK range, more advanced techniques need to be implemented using dilution refrigerators.

Dilution refrigerators function based on a mixture of ^3He and ^4He . At ~ 870 mK, the ^3He and ^4He mixture spontaneously separates into a ^3He -rich and ^3He -poor phase [216]. Cooling power is generated from the heat needed for the ^3H to cross the phase boundary from the rich to the diluted phases. This phase transition can be continuously driven and base temperatures of ~ 20 mK can be obtained.

On the measurement side, we implemented low frequency lock-in-techniques to measure the differential conductance and resistance. Figure 4.8 shows an illustration of an typical measurement setup. We apply a voltage bias to one end of the nanowire using a standard lock-in (Stanford SR830) and measure the current using low-noise a I/V converter on the other end of the nanowire.

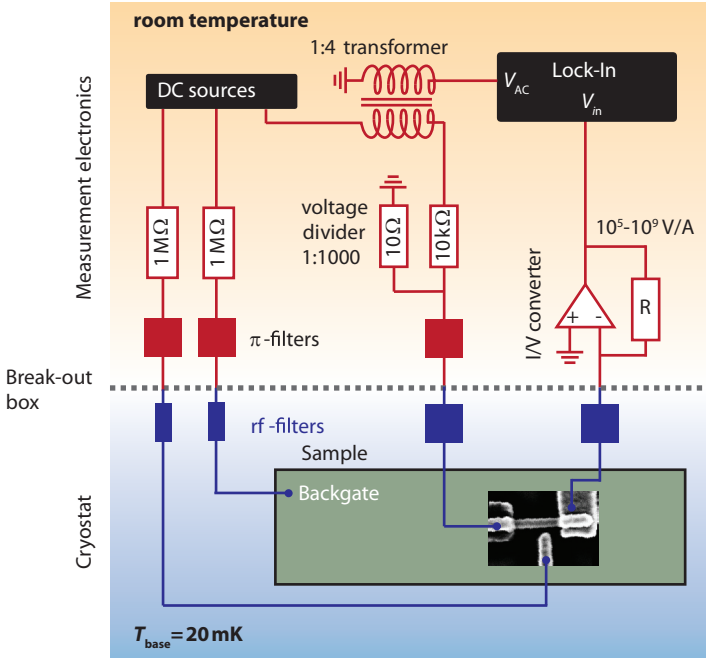


Figure 4.8. Schematic of a typical low frequency voltage bias differential conductance measurement at a base temperature of ~ 20 mK. Adapted from Refs.[103, 104, 107, 211].

We apply a small AC voltage that is stepped down using a 1:4 transformer, transpose the signal with a DC voltage source (Yokogawa YK7651), then the combined signal is further reduced using a 1:1000 voltage divider directly on the breakout box. In addition, DC voltages were applied to electrostatic gates using a 8 channel high resolution digital-to-analog converter (DAC) that was built in-house by the electronics workshop. If voltages higher than 10 V were required, the DAC was connected to a voltage amplifier that was also built in-house.

The measurements were performed using QCodes, a python based program that was developed in Delft, and QCTools which was developed by Dr. Joost Ridderbos. Dr. Gergő Fülöp and Dr. Joost Ridderbos were heavily involved in the setup, problem solving, and maintenance of these programs within our group.

5 **Electrostatic gate-defined tunnel barriers in carbon nanotubes and InAs nanowires**

The first approach to form deterministic tunnel barriers is by electrostatic gating of a carbon nanotube (CNT) and an InAs nanowire (NW). Tunnel barriers formed via electrostatic gating have been shown to be a powerful tool to enable the confinement and manipulation of individual charge carriers, as well as spin, to form fully tunable single and double quantum dots where crucial QD parameters can be freely tuned *in situ* by electric and magnetic fields [217, 218]. Furthermore, due to their straight forward top-down fabrication method, electrostatic gate-defined QDs can be formed in a wide variety of material systems like two-dimensional electron gases [73, 219], CNTs [14, 16, 18–20, 27, 30, 96, 97, 186, 187, 194], NWs [6, 44, 48, 50, 61, 80, 82, 83, 88, 89, 220], and two-dimensional van der Waals materials [98, 221, 222].

In this chapter, we begin with an introduction to electrostatic gate-defined tunnel barriers in a quantum wire. Then we present a realization of two electrostatic gate-defined tunnel barrier devices incorporating either a CNT or InAs NW. Afterwards, we present single and double QDs formed by electrostatic gating and extract their electrostatic properties. To conclude, a short discussion of tunnel barriers formed via electrostatic gating is presented.

5.1. Electrostatic gate-defined tunnel barriers

We first begin with a brief introduction to how tunnel barriers are formed in a one-dimensional wire by electrostatic gating. The working principle behind electrostatic gate-defined tunnel barriers is a shifting of the band edge relative to the Fermi level, E_F , to higher or lower energies in specific regions along the one-dimensional wire using gate electrodes in close proximity to the wire. If the shift of the band edge is large enough, a potential barrier in the quantum wire is formed that the electrons or holes must overcome by quantum tunneling to contribute to transport (see: Chapter 2.1.3).

A schematic of a typical electrostatic gate-defined tunnel barrier device is illustrated in Fig. 5.1 for two (a) and three (b) tunnel barriers. A series of five metallic gates (red) are lying on top of the substrate (grey). The wire (green) lies on top of five metallic gates (G1-G5) separated by a thin insulating layer (turquoise) and is electrically contacted to metallic reservoirs (yellow).

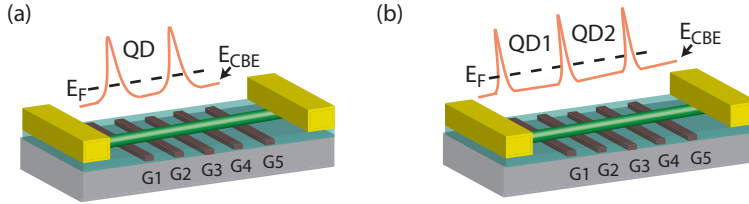


Figure 5.1. Electrostatic gate-defined tunnel barriers formed in a quasi one-dimensional wire: Five gates (G1-G5) are prepatterned onto a substrate (grey). The wire (green) is lying on top of five metallic gates (G1-G5) separated by a thin insulating layer (turquoise). By applying negative or positive voltages to one of the gates, the conduction band edge, E_{CBE} in close proximity to the gate shifts to higher or lower values relative to the Fermi energy, E_F . In (a) a negative voltage values are applied to G2 and G4, shifting E_{CBE} to higher values and confining the region between G2 and G4 and forming a quantum dot (QD). A similar situation is presented in (b), but now an additional tunnel barrier is formed with G3. Now two regions along the wire become confined which forms two QDs in series: QD1 and QD2.

Now, we first consider the case of Fig. 5.1(a). If a negative voltage is applied to gates G2 and G4, an electric field is formed perpendicular to the gates. The electric field couples to the semiconductor bands of the wire in close proximity to the gates via the field effect [65] and shifts the conduction band edge energies, E_{CBE} , to higher or lower values relative to E_F . If the shift of E_{CBE} is sufficiently large, tunnel barriers are formed by G2 and G4 and the region along the wire between G2 and G4 becomes confined, resulting in the formation of a QD. A similar situation is presented in Fig. 5.1(b), where now three tunnel barriers are formed by applying negative values to gates G1, G3, and G5. Consequently, the regions between G1 and G3, as well as between G3 and G5 become confined, resulting in two axial QDs in series: QD1 and QD2. Now for charge carriers to contribute to transport, an extra tunneling event must take place between one quantum state to another quantum state.

Since the tunnel barriers are controlled by voltages applied to the gates, their heights are easily controlled. Their widths are approximated by the width of the gate electrodes. However, the potential profile for electrostatic gate-defined tunnel barriers is often not well understood and highly depends on the coupling between the gate and the wire.

5.2. Electrostatic gate-defined tunnel barrier devices

Now, we present two realizations of electrostatic gate-defined tunnel barrier devices. We incorporate the bottom gate structure discussed in Sec. 4.1 with two different material systems: an InAs NW and a CNT. Figure 5.2 shows a false colored scanning electron microscope (SEM) image of a typical electrostatic gate-defined tunnel barrier device. The bottom gate structures consists of a grid of five 30 nm wide metallic titanium/gold (Ti/Au) gates with a center-center(pitch) distance of 100 nm. A 50 nm thick silicon nitride (Si_3N_4) layer (black) covers the bottom gate structures that acts as an insulating layer. Afterwards, the Si_3N_4 layer near the edge of the bottom gate structure is etched away, revealing the bare metallic gates (G1-G5). Subsequently, the NW or CNT and all of the individual metallic gates are contacted by a 65 nm layer of titanium/gold (yellow). The distance between source (S) and drain (D) contacts is ~ 700 nm. The electrochemical potential in the NW or CNT is tuned by the gate voltages $V_{G1} - V_{G5}$, which shifts E_{CBE} , relative to E_{F} , to higher or lower values in the region of the NW or CNT close to the gate.

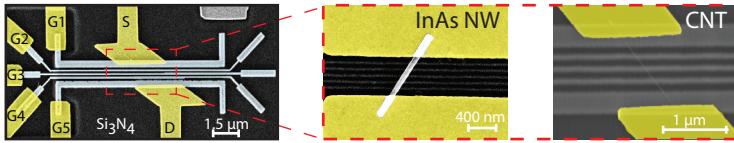


Figure 5.2. Electrostatic gate-defined tunnel barrier devices: False colored scanning electron microscope (SEM) image of a typical electrostatic gate-defined quantum dot device. (inset) InAs nanowire (NW) and carbon nanotube (CNT) lying on top of the bottom gate structure (G1-G5).

Two different devices are presented: one InAs NW (NW1) and one CNT (CNT1) device. The inset of Fig. 5.2 shows a false colored SEM image of device NW1 and CNT1. All measurements were performed in at a base temperature of 270 mK. The differential conductance, $dI/dV = I_{\text{AC}}/V_{\text{AC}}$, was measured using standard low frequency lock-in techniques described in Sect. 4.3.

5.3. Formation of tunnel barriers

We first show that the bottom gates can induce tunnel barriers into the device via electrostatic gating. For this, we demonstrate that the device can be depleted with each gate. The measurements presented in this section are from device NW1.

Figure 5.3 shows dI/dV as a function of V_{G} for G1-G5 with a constant source-drain voltage bias, $V_{\text{SD}} = 2$ mV. The gates not being swept are kept

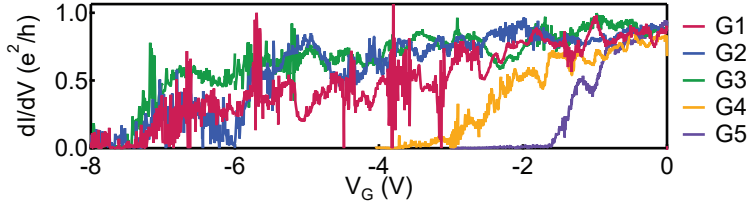


Figure 5.3. Formation of tunnel barriers in device NW1: (a) Differential conductance, dI/dV , as a function of gate voltages, $V_{G1} - V_{G5}$, for $V_{SD} = 2$ mV. For each gate sweep, the other four gates are kept at 0 V.

at a constant voltage of 0 V. We observe that for $V_G = 0$, $dI/dV \approx 0.8e^2/h$ is roughly constant. As V_G is decreased, dI/dV decreases until $dI/dV \approx 0$ for $V_{G1}, V_{G2}, V_{G3} \approx -8$ V, $V_{G4} \approx -4$ V, and $V_{G5} \approx -1.8$ V. This gate voltage value is commonly referred to as the pinch-off voltage and can be understood as an increase in E_{CBE} in the region of the NW in close proximity to the gate is shifted to higher energies relative to the rest of the NW. This results in the formation of a tunnel barrier and consequently lowers dI/dV until the tunnel barrier is sufficiently large such that $dI/dV \approx 0$. We speculate that the difference in depletion voltages for the gates is attributed to different couplings between the electric field produced by the gates and the NW, screening effects from the metallic contacts, and gating effects by the source contact.

These measurements show that the electrostatic gates can induce tunnel barriers along specific regions of the NW and that we can form large enough tunnel barrier that the electrons cannot overcome and transport is blocked.

5.4. Single quantum dots

Now we focus on creating a single QD in the NW by forming tunnel barriers with two gates. A schematic of the gating configuration is illustrated in Fig. 5.4(a). Two tunnel barriers (red) are formed by applying negative gate voltages to gates G1 and G5, thus increasing E_{CBE} . Here, $V_{G1} = -2.5$ V and $V_{G5} = -1.3$ V, respectively. Consequently, a QD (green) is formed in $L_{G1-G5} = 300$ nm long NW segment between G1 and G5. The electrochemical potential of the QD is tuned with applying a voltage, V_{G234} , to gates G2, G3, and G4 simultaneously (blue).

Figure 5.4(b) shows dI/dV as a function of V_{SD} and V_{G234} for this gating configuration. We observe a regular set of Coulomb blockade (CB) diamonds over a gate range of 80 mV, corresponding to the addition of 12 electrons on the QD. As discussed in Sect. 2.2.1, we can extract the addition, E_{add} and charging, E_C , energies, as well as the single particle level spacing, δE , from the dimen-

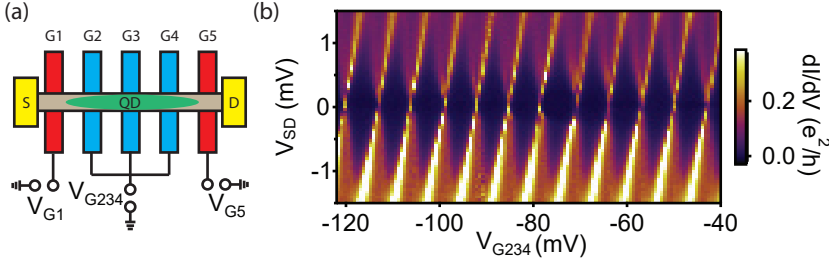


Figure 5.4. Single quantum dots in device NW1: (a) Schematic of the gating configuration to define a single quantum dot (QD). Gates G1 and G5 are used to define tunnel barriers (red) between which a QD (green) is formed in the $L_{G1-G5} = 300$ nm long NW region. Gates G2, G3, and G4 are used to tune the electrochemical potential of the QD by applying a voltage, V_{G234} , to each of the gates simultaneously. (b) Differential conductance, dI/dV , as a function of source drain bias, V_{SD} and gate voltage, V_{G234} , with $V_{G1} = -2.5$ V and $V_{G5} = -1.3$ V. Regular Coulomb blockade (CB) diamonds are observed.

sions of the CB diamonds. From the height of the CB diamonds, we extract $E_{\text{add}} = (1.2 \pm 0.1)$ meV. No two-fold symmetry of the CB diamonds was observed and E_{add} is constant as a function of the QD population. In addition, no visible excite state resonances were observed. From the slopes of the CB diamond edges, we extract the QD lever arm, $\alpha = 0.128 \pm 0.005$. In addition, using Eq. 2.11, we extract the total capacitance of the QD, $C = (133 \pm 10)$ aF and QD gate capacitance $C_{G234} = (17 \pm 2)$ aF. We also observe that each CB diamond exhibits an increase of dI/dV along one edge of the CB diamond. This diamond edge corresponds to the transport process when the chemical potential of the source, μ_S , aligns with the chemical potential of the QD, μ_{QD} . Therefore, an increase in dI/dV is expected when the coupling between the QD and the source contact is stronger than the QD and drain contact.

5.5. Double quantum dots

Now, we show that the by decoupling G3 from G2 and G4, and applying negative values of V_{G3} , we can split the single QD into a double quantum dot (DQD). One QD will be confined between G1 and G3, while the second QD is confined between G3 and G5. By lowering V_{G3} , we form a tunnel barrier in the middle of the single QD. If the tunnel barrier is sufficiently opaque, the single QD will evolve into a DQD depending on the V_{G3} . Figures 5.5(a)-(b) show the stability diagrams for $V_{G3} = -2$ V and $V_{G3} = -4$ V with $V_{SD} = 1$ mV, respectively.

For $V_{G3} = -2$ V, we observe a stability diagram that is typical for a single QD. From the spacing between the diagonal CB resonances, ΔV_{G2} and ΔV_{G4} , we can extract the gate capacitances using Eq. 2.12. From Fig. 5.5(a), we extract $\Delta V_{G2} = \Delta V_{G4} = (22 \pm 1)$ mV for G2 and G4. This corresponds to an equal gate capacitance for both gates, $C_{G2} = C_{G4} = (7.3 \pm 0.3)$ aF. This is in agreement from the single QD measurement, $C_{G2} + C_{G4} \approx C_{G234}$, further indicating that the single QD spans the total distance between G1 and G5 as expected.

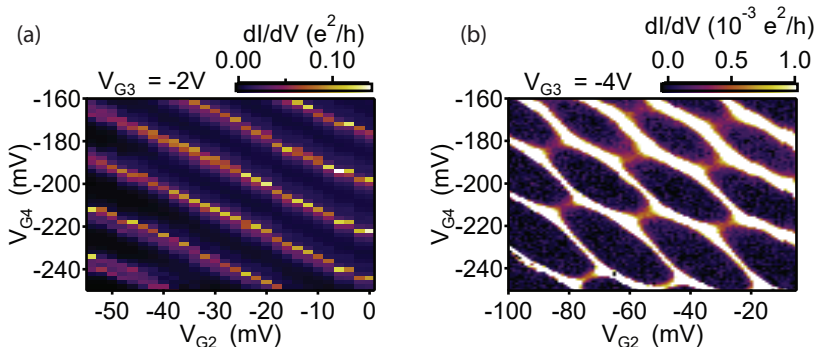


Figure 5.5. Transition from a single QD to a DQD in device NW1: (a)-(b) Differential conductance dI/dV as a function of V_{G2} and V_{G4} for $V_{G1} = -2.5$ V, $V_{G5} = -1.3$ V, and V_{SD} . (a) For $V_{G3} = -2$ V and the resulting charge stability diagram takes the form of a single quantum dot. (b) For $V_{G3} = -4$ V, the charge stability diagram evolves into one for a strongly coupled double quantum dot.

By further lowering of the voltage applied to G3 to $V_{G3} = -4$ V, thus increasing the interdot tunnel barrier, we observe that the stability diagram evolves from diagonal CB resonances to a honeycomb pattern. From Fig. 5.5(e), we extract $\Delta V_{G2} = (27 \pm 1)$ mV and $\Delta V_{G4} = (22 \pm 1)$ mV, resulting in $C_{G2} = (5.9 \pm 0.2)$ aF and $C_{G4} = (7.2 \pm 0.3)$ aF. From the splitting of the triple points and using Eq. 2.13, we extract a mutual capacitance of $C_M = (2.2 \pm 0.2)$ aF. The mutual capacitances of both of the QDs are roughly equal and on the order of C_{G2} and C_{G4} which indicates that the two QDs are strongly coupled. Similarly for the cross capacitance, we extract $C_{G2,C} = (1.0 \pm 0.2)$ aF and $C_{G4,C} = (0.7 \pm 0.4)$ aF. This indicates that V_{G2} slightly tunes the chemical potential of the right QD and similarly for V_{G4} and the left QD.

Further decreasing V_{G3} should result in a larger tunnel barrier between the two QDs. Thereby decreasing their mutual capacitances further and the system would transition into the weakly coupled DQD regime. In this region,

the triple points evolve into bias triangles from which the total capacitances of QD1 and QD2 can be extracted. However, in this device, decreasing V_{G3} further caused instability of the gates due to charge noise and no transition into the weakly coupled DQD regime could be observed. Therefore, for this device it was not possible to extract the total capacitances. Another method would be to analyze the CB diamonds of QD1 and QD2 and extract the total capacitance from the heights of the CB diamonds, but this measurement was not performed.

Nonlinear transport regime

To investigate the nonlinear transport regime, we turn to device CNT1, as shown in Fig. 5.2. In this device only one gate was used to induce a tunnel barrier into the CNT, G3, while the other two tunnel barriers were formed at the metal-CNT interface. The electrochemical potential of QD1 was tuned by a voltage, V_{G12} , applied to G1 and G2 simultaneously. Similarly, the electrochemical potential of QD2 was tuned by a voltage, V_{G45} , applied to G4 and G5 simultaneously. The coupling between QD1 and QD2 is tuned by V_{G3} .

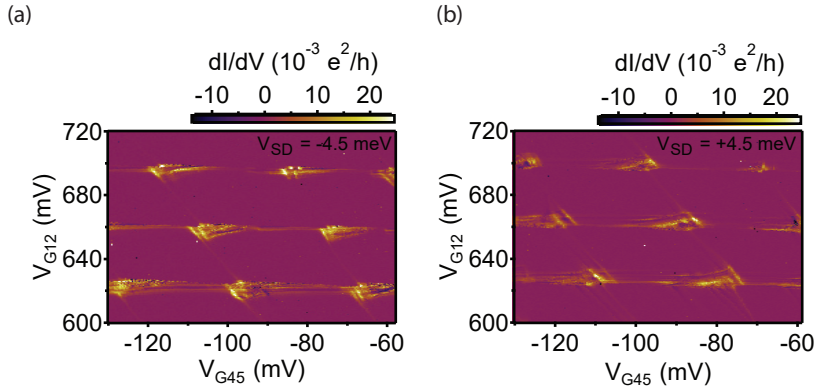


Figure 5.6. Charge stability diagram in device CNT1: dI/dV as a function of gate voltages, V_{G12} and V_{G45} , for (a) negative and (b) positive source-drain bias voltage, $V_{SD} = \pm 4.5$ meV. The resulting charge stability diagram takes the form of two weakly coupled quantum dots. A regular pattern of bias triangles were observed.

In Fig. 5.6, we show dI/dV as a function of V_{G12} and V_{G45} with $V_{G3} = -100$ mV for negative (a) and positive (b) $V_{SD} = \pm 4.5$ meV. We observe a stability diagram that features several bias triangles in a regular honeycomb pattern that is characteristic for weakly coupled DQDs.

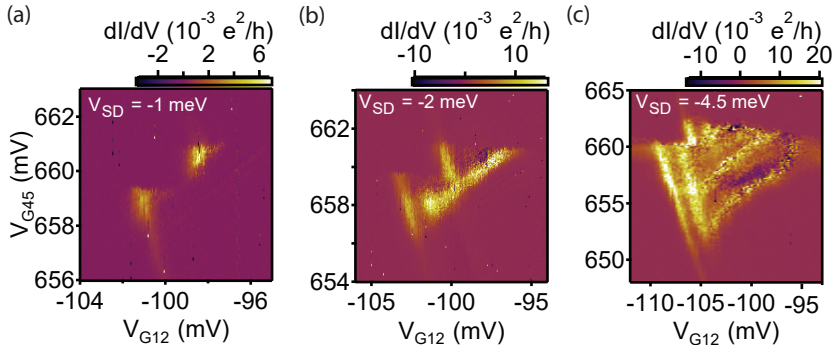


Figure 5.7. Bias triangles in device CNT1: (a)- (c) Bias triangles for three different source drain bias voltage values: (a) $V_{SD} = -1$ mV, $V_{SD} = -2$ mV, and $V_{SD} = -4.5$ mV. For increasing V_{SD} , the fully separated bias triangles in (a) begin to overlap (b) until they fully overlap (c).

Now, we investigate the dependence of V_{SD} on the dimensions of the bias triangles. As discussed in Sect. 2.3, the splitting of the triple points, thus the bias triangles, is dependent on V_{SD} . Figure 5.7 shows the bias triangles for: (a) $V_{SD} = -1$ mV, (b) $V_{SD} = -2$ mV, and (c) $V_{SD} = -4.5$ mV. We observe that for $V_{SD} = -1$ mV the two bias triangles are fully separated, similar to triple points when $V_{SD} \approx 0$. For $V_{SD} = -2$ mV, two bias triangles increase in size and begin to overlap. Increasing the bias further to $V_{SD} = -4.5$ mV, causes the bias triangles nearly overlap fully.

From the measurements in Figures 5.6 and 5.7, all of the capacitances of the DQD can be extracted. From the dimensions of the honeycomb pattern in Fig. 5.6(a) and Eq. 2.12, we extract $C_{G12} = 5$ aF and $C_{G45} = 6$ aF. Similarly, the total capacitances of QD1, C_1 , and QD2, C_2 , were extracted from the dimensions of the bias triangles in Fig. 5.7(b) using Eq. 2.14. This yields $C_1 = 10$ aF and $C_2 = 18$ aF. C_M was determined using Eq. 2.13 by the dimensions of the honeycomb pattern in Fig. 5.6(a) and the dimensions of the bias triangles in Fig. 5.7(a). This yields, $C_M \approx 1.2$ aF. Therefore, all of the capacitances are accounted for in this device.

5.6. Discussion

All of the devices in this chapter utilized electrostatic gating by metallic gates below the CNT or NW to form tunnel barriers in the system. The tunnel barriers confined the electrons along the CNT or NW such that single and double QDs could be studied and their associated capacitances were extracted.

Electrostatic gate-defined tunnel barriers offer a the large experimental tunability that is not easily achieved in other gating configurations. For example, in our devices a single or double QD system can be fully tunable with three or five gates, respectively. In the case of DQDs, this includes the tunnel barriers that isolate the QD from the contacts (G1 and G5), the tunnel barrier that tunes the interdot coupling (G3), and two gates that tune the electrochemical potential of the two QDs (G2 and G4). This allows for comprehensive studies of single charges and spins using QDs where each parameter is gate tunable.

This thesis tries to achieve deterministic tunnel barriers, meaning their physical and energetic properties are well-known. In an ideal electrostatic gating device, only the local band structure of the wire that is in direct proximity of the gate is tuned and the tunnel barrier formed has a well-defined position and width given by the gate width. However, this is not what we observed in our system and the tunnel barriers are far from deterministic, as this thesis tries to realize. The tunnel barriers are defined by the electrostatic gates that have well-defined widths, however it is unclear how this is related to the potential profile of the induced tunnel barriers. Their potential profile is strongly dependent on the electrostatic coupling between the gate and the NW or CNT, as well as where the space charge density [179]. In addition, while the tunnel barrier height can be tuned by applying a voltage to the gate, how this effects the potential profile of the induced tunnel barrier is unknown.

An estimation of the confinement strength can be deduced from Fig. 5.4(b). If there was strong confinement, one would expect highly symmetric QDs with large addition and charging energies, as well as level spacings to observe features of the density of states in the lead segments between the QD and contacts. In our measurements, we observed small addition and charging energies without two-fold symmetry, characteristic of a small and wide tunnel barriers resulting in weak quantum confinement [179]. In addition, no resonances were observed outside of the CB diamonds, indicating that the QD level broadening is too large to resolve them. We use these observations as evidence that the electrostatic-gate defined tunnel barriers are not well-defined nor deterministic, making it difficult to use them as tunnel spectrometers.

6 Integrated tunnel barriers in InAs/InP heterostructure nanowires¹

In this chapter, we take an alternative approach to form deterministic tunnel barriers: integrated tunnel barriers in indium-arsenide/indium-phosphide (InAs/InP) heterostructure nanowires (NWs). In this system, two short InP segments are grown in-situ during the InAs NW growth, forming a heterostructure nanowire. The two InP segments cause a band realignment due to strain at the InAs/InP interface resulting in a conduction band edge offset and consequently form in-situ grown tunnel barriers in the NW [54, 61, 223, 224]. Due to the strong confinement of tunnel barriers, a quantum dot (QD) is formed in the InAs segment between the two InP segments. Similar heterostructures have been used previously to investigate single [61, 80, 84, 90, 91, 95, 225] and double [77, 226] QD physics, as well as thermoelectric transport [78, 92].

We present an in-depth analysis of an InAs/InP heterostructure NWs, demonstrating their exceptional long term stability and broad electrical tunability. We report a detailed and comprehensive characterization of the InP tunnel barriers and the resulting Coulomb blockade (CB) resonance lineshapes, which can be crucial, for example, to distinguish different single electron [227] or superconducting subgap transport processes [93, 193]. We show that the in situ grown InP barriers result in highly predictable, electrically tunable, and symmetric QDs with level broadenings that are small enough for high resolution spectroscopy of subgap states in hybrid systems, demonstrated by distinct spectral features in the lead segments.

6.1. Principles of integrated tunnel barriers

InAs/InP nanowire growth

To understand the integrated tunnel barriers in InAs/InP heterostructure nanowires, we begin with their growth and geometric properties. They are synthesised similarly to the InAs NWs presented in Sect. 3.1, i.e. by vapor-liquid-solid methods via chemical beam epitaxy [55]. The growth process is schematically illustrated in Fig. 6.1(a). First, a thin gold film was evaporated

¹Parts of this chapter have been published in similar form in Ref. [87]

onto an epitaxially grown InAs(111)B substrate, then underwent a thermal annealing step inside of the growth chamber to initiate the formation of randomly distributed gold catalyst nanoparticles with a diameter of 40 nm to 50 nm (Fig. 6.1(a)(i)). Next, trimethylindium(TMIn) and tert-butylarsine(TBAs) are introduced into the system to initiate the growth of InAs by feeding the TMIn and TBAs to the gold catalyst particle until it supersaturates and begins to grow (Fig. 6.1(a)(ii)). After a sufficient amount of InAs has grown, the As gas is shut off and tert-butylphosphine(TBP) is introduced into the chamber and similarly fed to the gold catalyst particle to initiate the growth of InP (Fig. 6.1(a)(iii)). Afterwards, the growth of InAs and InP is repeated to form a short segment of InAs (Fig. 6.1(a)(iv)) and InP (Fig. 6.1(a)(v)). After the growth of the second InP segment, a long segment of InAs is grown (vi). This procedure has been shown to produce pure InAs and InAs/InP heterostructure NWs with straight morphology, constant diameter, defect-free wurtzite crystal structure, and atomically sharp interfaces between the InAs and InP [55].

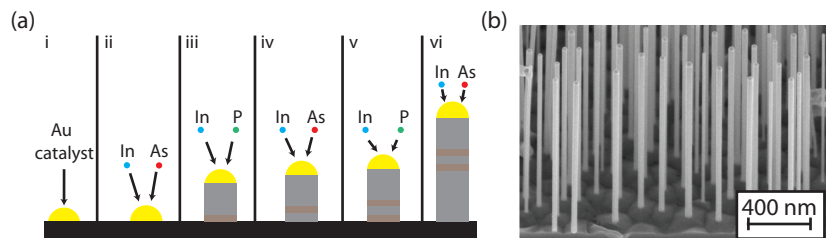


Figure 6.1. InAs/InP heterostructure nanowire growth: (a) Schematic of the vapor-liquid-solid growth process of InAs/InP heterostructure nanowires. (i) Gold catalyst particles are formed on the InAs(111)B substrate. (ii) In and As are fed to the gold catalyst to initiate the growth of InAs. (iii) In and P are fed to the gold catalyst to initiate the growth of InP. (iv)-(v) A similar process to grow another short segment of InAs and InP. (vi) A long segment of InAs is grown. (b) Scanning electron microscope (SEM) image of InAs/InP heterostructure nanowires on the growth chip. The schematic was adapted from Refs. [104, 106, 160] and the SEM image was provided by Lucia Sorba.

A scanning (SEM) and transmission (TEM) electron microscope image of two InAs/InP heterostructure NWs are shown in Fig. 6.2(a) and (b), respectively. The hexagonal NW has a diameter of 50 ± 5 nm, with two InP segments of widths $\ell_1, \ell_2 \approx 5.5$ nm located 440 nm from the gold catalyst. Bounded by the two InP segments, a QD is formed on an InAs segment of length $s \approx 19$ nm. The dimensions of the InP barriers were determined in a TEM analysis of NWs of the same growth. Additional data for shorter InP segments (2 nm to 3 nm)

can be found in Appendix B.

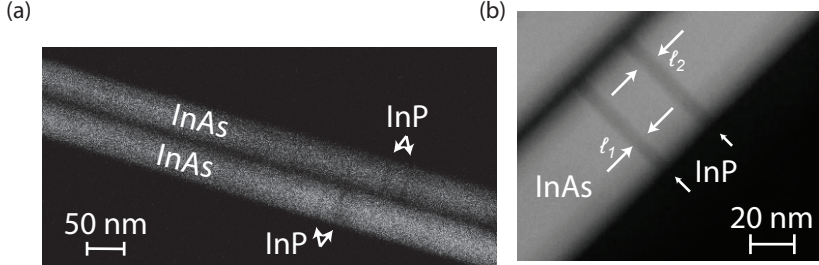


Figure 6.2. Identification of the InP segments: Scanning (a) and transmission (b) electron microscope image of two InAs/InP heterostructure nanowires. The two InP segments, indicated by the white arrows, are clearly seen by the change in contrast. From the SEM image, we find that the two InP segments are located ~ 440 nm from the gold catalyst particle, the two InP segments are $\ell_{1,2} \approx 5.5$ nm wide separated by ~ 20 nm of InAs. TEM image provided by Valentina Zannier.

The two InP segments can be clearly seen using only standard SEM techniques with an in-lens detector. This enables us to know the exact location of the tunnel barriers in our devices. Therefore, in this system, we can state with high precision where the quantum dot is positioned relative to any electrical contacts or gates. This is a valuable tool for spectroscopy measurements where the geometric properties and length scales of the device plays a crucial role. This is a great advantage over other integrated tunnel barriers, such as InAs crystal-phase defined quantum dots, where more advanced techniques are required to know the precise location which is not feasible to perform for each device [48, 50].

Formation of integrated tunnel barriers

Now, that we established how InAs/InP heterostructure nanowires are grown, we discuss the underlying physics behind the formation of integrated tunnel barriers in this system. As stated earlier, integrated tunnel barriers are formed by implementing two short in-situ grown InP segments in an InAs NW. The working principle behind integrated tunnel barriers is a conduction band edge (CBE) offset at the InAs/InP interface. This is well understood in the case of bulk semiconductors where various semiconductor heterostructures have been realized [228–230].

A schematic of an InAs/InP heterostructure NW is illustrated in Fig. 6.3(a).

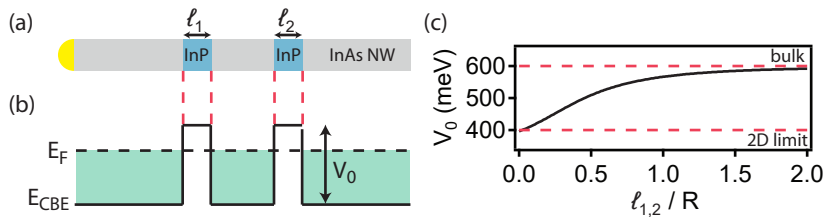


Figure 6.3. Formation of integrated tunnel barriers: (a) Schematic of an InAs/InP heterostructure nanowire (NW) consisting of an InAs NW (grey) with two in situ grown InP segments (blue) and gold catalyst particle (yellow). (b) Schematic of the energy diagram for a nanowire with two in-situ grown tunnel barriers. Strain from the lattice mismatch between two materials with different band gaps results in a conduction band edge (CBE) offset, V_0 , relative to the CBE, E_{CBE} . The Fermi energy, E_F , is indicated by the dashed line. (c) V_0 as a function of the ratio between the InP thickness, $\ell_{1,2}$, to the NW radius, R . For, $\ell_{1,2}/R > 1$, V_0 takes the bulk value of 600 meV, while for $\ell_{1,2}/R < 1$, V_0 is decreased continuously to 400 meV due to the NW geometry. Figures adapted from Refs. [104, 160, 224].

The system consists of an InAs NW (grey) with two in-situ grown InP segments of widths $\ell_{1,2}$ (blue) and a gold catalyst particle (yellow). The systems respective energy diagram is schematically illustrated in Fig. 6.3(b).

The first striking difference is the CBE becomes energetically offset at the InAs/InP interface. To explain this CBE offset, we consider what happens when the two materials are brought into contact with one another. The Fermi levels of InAs and InP are forced to align, causing the CBEs of InAs and InP to align with a bulk CBE offset, V_0^{bulk} , at the interface of the two materials. For an atomically sharp interface, the potential profile takes the form of a hard-wall potential barrier for electrons with height $V_0^{\text{bulk}} = 600$ meV in the bulk case [224]. However, in a nanowire system one has to consider the effects of strain, ϵ , and the InP widths, $\ell_{1,2}$. The InP segments are put under biaxial strain from the InAs which lowers the conduction band (CB) energy. This shift in energy, δE_{CB} , can be described by: $\delta E_{CB} = a_c(2\epsilon_{\parallel} + \epsilon_{\perp})$, where $a_c = -5.2$ eV is the conduction band deformation of InP, while $\epsilon_{\parallel} = 3.23\%$ and $\epsilon_{\perp} = -2.04\%$ are the amount of strain in the axial and radial direction, respectively [224]. The resulting CBE offset, or tunnel barrier height, in the 2D limit is given by [224]: $V_0 = V_0^{\text{bulk}} + a_c(2\epsilon_{\parallel} + \epsilon_{\perp})$. This results in a conduction band edge offset of 370 meV, significantly lower than the bulk value of 600 meV. As stated earlier, V_0 is also highly dependent on the thickness of the InP segments. The dependence of $V_0(\ell_{1,2}/R)$ is given by [224]:

$$V_0(\ell_{1,2}/R) = V_0^{\text{bulk}} \cdot \left(1 - \frac{0.34}{1 + 0.92(\ell_{1,2}/R) + 4.15(\ell_{1,2}/R)^{2.41}} \right) \quad (6.1)$$

where $\ell_{1,2}/R$ is the ratio of the InP widths to the NW radius, R . This is plotted in Fig. 6.3(b) for various NW geometries. For long InP segments, $\ell_{1,2}/R > 1$, V_0 takes the bulk value of 600 meV. However, for shorter InP segments, $\ell_{1,2}/R < 1$, V_0 is continuously lowered to the 2D limit of 400 meV due to strain. For our NW geometry, $\ell_{1,2}/R = 0.22$ and the barrier height is predicted to be $V_0 \approx 400$ meV [224], providing a strong confinement to the electrons in the axial direction.

6.2. Integrated tunnel barrier device

To investigate the properties of the integrated tunnel barriers, we implement an InAs/InP heterostructure device. A false color scanning electron microscopy (SEM) image of a typical device is shown in Figure 6.4. The electrical contacts (yellow) to the NW are made of titanium/gold films with a thickness of 5 nm/65 nm. Before evaporating the contact material, the native oxide of the NWs is etched with an $(\text{NH}_4)_2\text{S}_x \cdot \text{H}_2\text{O}$ solution [213]. Further details about the device fabrication can be found in Sect. 4.2. Due to the simplicity of this system, it can easily be related back to the notation used in Chapter 2.1. The InAs/InP heterostructure NW acts as a quasi one-dimensional quantum wire, where the Ti/Au metallic contacts are the electronic reservoirs, the long InAs segments are the leads, and the InP segments are scatter centers.

We explicitly refer to the regions of bare InAs between the QD and the source or drain contact as the lead segments (LSs) [50]. The lead segment LS_1 between the QD and the source contact is $L_1 \approx 350$ nm long, while the lead segment LS_2 between the QD and the drain contact is $L_2 \approx 600$ nm long. The QD and the LSs are tuned simultaneously by the back gate voltage V_{BG} , which shifts the conduction band edge, $E_{\text{CBE}}(V_{\text{BG}})$, relative to the Fermi energy, E_{F} , to higher or lower values. For later, we define $\phi(V_{\text{BG}}) = E_{\text{F}} - E_{\text{CBE}}(V_{\text{BG}})$.

The inset of Figure 6.4 shows a TEM image of the epitaxially defined QD region in a similar NW. The two InP segments, indicated by black arrows, act as tunnel barriers with a rectangular potential profile for electrons due to the atomically sharp transitions in the material composition.

All measurements were performed in a dilution refrigerator with a base temperature of ~ 30 mK. We apply a DC voltage to the source electrode to correct for small offsets ($V_{\text{DC}} \approx 50$ μV) from the I/V converter and superimpose an AC voltage of typically 1 μV_{rms} for lock-in detection, while the drain electrode is grounded and used for the current (I) measurement. The differential conductance $dI/dV_{\text{SD}} = I_{\text{AC}}/V_{\text{AC}}$ was measured using standard lock-in techniques.

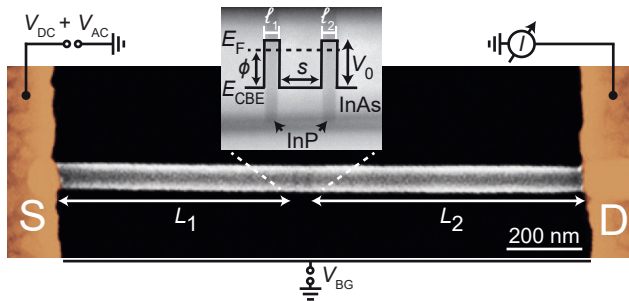


Figure 6.4. InAs/InP device: False colored scanning electron micrograph of a typical device consisting of an InAs nanowire with two in situ grown InP tunnel barriers of length $l_1, l_2 \approx 5.5$ nm. The nanowire segments between the contacts (S/D) and the quantum dot (QD) are referred to as the lead segments $LS_{1/2}$ of lengths $L_{1/2}$. A QD of length $s \approx 19$ nm forms between the two tunnel barriers due to the conduction band offset, V_0 , between InAs and InP. V_{BG} is the global backgate voltage that simultaneously tunes the QD and the LSs. The inset shows a transmission electron microscopy image of two InP segments pointed out by two black arrows and an energy diagram of the gate tunable conduction band edge, E_{CBE} . The Fermi energy, E_F , is indicated by a dashed line and the difference between E_F and E_{CBE} is defined as ϕ .

6.3. Characterization of the quantum dot

Figure 6.5(a) shows dI/dV_{SD} as a function of V_{SD} and V_{BG} . We observe regular, stable, and reproducible Coulomb diamonds (CDs) over the large backgate range of 30 V, corresponding to the addition of ~ 124 electrons. At $V_{BG} \approx 1$ V, the number of electrons on the QD is close to zero, i.e. $N \approx 0$. By increasing V_{BG} , electrons are added to the QD sequentially, which brings the QD into the many electron regime. For the measurement sequence shown in Fig. 6.5(a), the maximum number of electrons on the QD is $N \approx 124$. When increasing V_{BG} beyond 40 V, thermal activation of carriers across the tunnel barriers begins to considerably contribute to the transport. Similar behavior was observed in another device and additional data can be found in Appendix C.

According to the constant interaction model [102], assuming two-fold spin degenerate orbitals, the energy required to add an electron to a QD with an even electron configuration is given by the addition energy $E_{add} = E_C + \delta E$, with $E_C = e^2/C_\Sigma$ the charging energy, the total capacitance C_Σ of the QD, and δE the single particle energy spacing. To add a second electron to the same QD orbital requires $E_{add} = E_C$. This gives rise to an alternating even-odd pattern of large and small CDs, characteristic for spin-degenerate QD states,

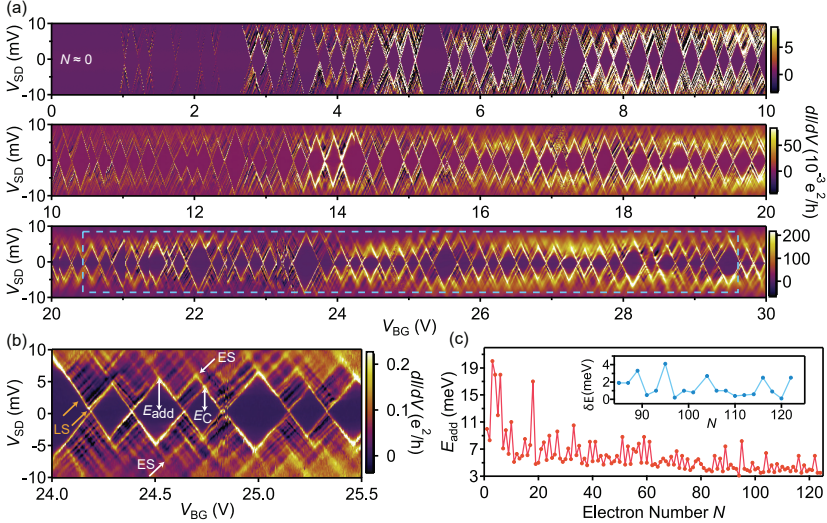


Figure 6.5. Coulomb blockade diamonds: Differential conductance, dI/dV_{SD} , as a function of the bias, V_{SD} , and the back gate voltage, V_{BG} . (a) Regular and stable Coulomb diamonds over a gate range of 30 V, ranging from near depletion with an electron population of approximately zero ($N \approx 0$) to $N = 124$. (b) High resolution Coulomb diamonds, where excited state (ES) resonances of the QD and the resonances due to a modulation in the density of states in the semiconducting lead segments (LSs) are pointed out by white and orange arrows, respectively. (c) The addition energy, E_{add} , as a function of the number of electrons on the quantum dot, N . The inset shows the difference of single particle energy spacing, δE , as a function of N in the many electron regime extracted from the region indicated by the blue box in (a).

and allows one to extract the corresponding energy scales. A region of the CDs shown in Fig. 6.5(b) exhibits a clear even-odd pattern with $E_{\text{add}} = 5.5$ meV and $E_C = 4.2$ meV, as indicated by the white arrows. From the difference between E_{add} and E_C , we find $\delta E = 1.3$ meV, consistent with $\delta E \approx 1.6$ meV from the corresponding excited state (ES) resonances outside the CDs, pointed out by white arrows.

In Fig. 6.5(c) we plot E_{add} as a function of N for the full V_{BG} range of Fig. 6.5(a). We find an overall decrease in $E_{\text{add}}(N)$ for increasing N due to changes in the QD capacitance by electron-electron interactions [231]. From the very regular even-odd pattern in the gate range indicated by the blue box in Fig. 6.5(a), we extract $\delta E(N)$, as shown in the inset of Fig. 6.5(c). We find that δE strongly scatters and assumes values in between 0.2 meV and 4 meV, suggesting that only single levels contribute to the transport.

In addition to the QD excited state resonances, we find several other features outside of the CDs that cannot be attributed to the energy spectrum of the QD. For example, the resonances indicated by orange arrows in Fig. 6.5(b) are due to a non-constant DOS in the LSs, forming as standing waves in the LSs. Since these waves are strongly reflected at the InP barrier, the widths of these states are determined mostly by the coupling to the source and drain contacts, respectively. In addition, we find negative differential conductance (NDC) throughout the entire gate range, which we attribute to the simultaneous tuning of the QD and the LSs with different lever arms. We note that the NDC is more prominent in the few electron regime where the carrier concentration is low. The NDC supports our notion that the DOS in the LSs is not constant, which is typical for NW QD devices with semiconductor leads [61]. Further analysis of these resonances and nonconstant DOS in the LSs is presented in Chapter 7.

6.4. Resonance line shapes

By analyzing the Coulomb blockade (CB) resonance line shape, we can extract the total tunnel coupling of the QD, Γ , and the electron temperature in the LSs, T . The total tunnel coupling, $\Gamma = \Gamma_1 + \Gamma_2$, is given by the individual couplings to the source and drain leads, Γ_1 and Γ_2 . In the case of an ideal measurement setup, the line shape only depends on Γ , T [232], and the asymmetry $A = \Gamma_1/\Gamma_2 \geq 1$ [233, 234]. However, there are also extrinsic broadening mechanisms, such as noise in the source and drain contacts, and on the gate, as well as the applied AC voltage.

For our analysis, we assume that only a single QD level contributes to the transport, i.e. $eV_{\text{AC}}, \Gamma, 4k_{\text{B}}T \ll \delta E$,² and account for the three main broadening contributions: V_{AC} , Γ , and T . V_{AC} limits the smallest width of the

² $4k_{\text{B}}T$ is the 10%-90% width of the Fermi-Dirac distribution

line shape that can be reliably extracted, therefore eV_{AC} should be chosen such that $eV_{\text{AC}} < 4k_{\text{B}}T, \Gamma$. By tuning E_{CBE} with V_{BG} , we can access three different regimes: thermally broadened ($\Gamma, eV_{\text{AC}} \ll 4k_{\text{B}}T$), lifetime broadened ($4k_{\text{B}}T, eV_{\text{AC}} \ll \Gamma$), or a combination of both ($eV_{\text{AC}} \ll \Gamma \approx 4k_{\text{B}}T$). These three regimes are summarized in Fig. 6.6(a), (c), and (e), where the lifetime broadening is indicated by the width of the blue QD levels and the thermal broadening by the width of the orange Fermi-Dirac distribution in the LSs.

We model the line shape of the CB resonances with the assumption that the DOS in the LSs is constant and discuss effects due to a non-constant DOS later. For a single energy level, the line shape of a conductance resonance is described by a resonant tunneling model [65, 232, 235]:

$$I = g \frac{e}{h} \int T_{\text{QD}}(E) [f_{\text{S}}(E) - f_{\text{D}}(E)] dE, \quad (6.2)$$

where $g = 1$ is the number of independent parallel transport channels, $T_{\text{QD}}(E) = (\Gamma_1 \Gamma_2) / (\Delta E^2 + \Gamma^2/4)$ the Breit-Wigner (BW) transmission function [65] with $\Delta E = E - E_0$ the detuning from the CB resonance centered at E_0 , and $f_{\text{S/D}}(E) = 1 / (1 + \exp((E + eV_{\text{S/D}}) / k_{\text{B}}T))$ are the Fermi-Dirac distributions in the LSs. dI/dV is calculated numerically. The contribution of V_{AC} is accounted for by evaluating Equation 6.2 for a sinusoidal V_{S} that also electrically gates the QD. If not chosen properly, V_{AC} can mask the "true" resonance and the measured resonance width is then given by V_{AC} .

In the regime where the broadening is mainly due to temperature, $\Gamma \ll 4k_{\text{B}}T \ll \delta E$, Equation 6.2 reduces to $G/G_{\text{max}} = \cosh^{-2}(\Delta E / 2k_{\text{B}}T)$, where $G_{\text{max}} = e^2/h \cdot \pi / (2k_{\text{B}}T) \cdot (\Gamma_1 \Gamma_2 / \Gamma)$ [232]. In this limit, T can be extracted from the full-width at half maximum (FWHM) of the resonance by $\text{FWHM} \approx 3.5k_{\text{B}}T$.

In the limit, where the broadening is mainly due to the electron lifetime on the QD, $4k_{\text{B}}T \ll \Gamma \ll \delta E$, Equation 6.2 reduces to the BW formula [65] $G/G_{\text{max}} = (\Gamma/2)^2 / (\Delta E^2 + (\Gamma/2)^2)$ with $G_{\text{max}} = e^2/h \cdot 4\Gamma_1 \Gamma_2 / \Gamma^2$. In this limit, $\text{FWHM} = \Gamma$ and A determines the maximum conductance $G_{\text{max}} = e^2/h \cdot 4A / (1 + A)^2$. Note that A is defined such that $A \geq 1$.

Evolution of the resonance line shapes

We now investigate how the line shapes of the resonances evolves with V_{BG} and the bath temperature, T_{bath} . Figures 6.6(b),(d), and (f) show high resolution CB resonance measurements in the three broadening regimes. To show the evolution of Γ , each of the three CB resonances was fit with the expressions for a thermal, BW, and the convolution line shape, described by Equation 6.2.

From the convolution fit, we extract Γ_1 , Γ_2 , T , and their corresponding standard error of the individual fits, shown as error bars in Fig. 6.6(g) and 6.7.³

Figure 6.6(b) shows a CB resonance near depletion ($N \approx 10$) at $V_{\text{BG}} = 6.6$ V, measured with $V_{\text{AC}} = 0.1$ μV . The convolution line shape agrees very well with the experiment, as does the pure thermal broadening line shape, but not the BW line shape. In this regime, the conduction band edge of the Ls is near the Fermi level ($\phi \ll V_0$) and the electrons are strongly confined by the large tunnel barriers, such that the width of the Coulomb resonance is mostly determined by the electron temperature and not by the QD lifetime. Only in this regime, we can accurately determine the electron temperature of the Ls. From the convolution fit, the extracted total tunnel coupling, asymmetry, and electron temperature are $\Gamma = 2.51 \pm 0.07$ μeV , $A = 1.05 \pm 0.04$, and $T = 50.5 \pm 0.2$ mK, respectively. We see that T is somewhat higher than the bath temperature ($T_{\text{bath}} = 30$ mK), probably due to noise and radiation due to insufficient filtering. Since T is not expected to change with V_{BG} , we set $T = 50.5$ mK for the following analysis of data at the same T_{bath} .

For the resonance at $V_{\text{BG}} = 13.5$ V ($N \approx 50$) a transition from the thermally to the lifetime broadened regime begins. As shown in Fig. 6.6(c) and (d), only the convolution line shape fits the data well. From the convolution fit, with $T = 50.5$ mK and $V_{\text{AC}} = 0.25$ μV fixed, $\Gamma = 18.1 \pm 0.4$ μeV and $A = 6.2 \pm 0.2$ were extracted from the fit. Therefore, this resonance is in the regime where the lifetime and thermal broadening contributes equally significantly with $\Gamma \approx 4k_{\text{B}}T$.

By increasing the gate voltage further, the CB resonances transition into the lifetime broadened regime with $\Gamma \gg 4k_{\text{B}}T$. This can be seen for the resonance in Fig. 6.6(f) at $V_{\text{BG}} = 24.99$ V ($N \approx 100$), where the data agrees very well with the convolution fit, as well as with the BW fit, with $T = 50.5$ mK and $V_{\text{AC}} = 1$ μV fixed. From the convolution fit, we extract $\Gamma = 52.5 \pm 0.1$ μeV and $A = 7.2 \pm 0.1$, which shows that the resonance is mostly lifetime broadened ($\Gamma \gg 4k_{\text{B}}T$).

For each of the three resonances, the temperature dependence of the CB resonances was investigated, as shown in Fig. 6.6(g). We used the convolution fit with Γ_1 and Γ_2 fixed at the values determined at $T_{\text{bath}} = 30$ mK, to extract T for a series of different T_{bath} . For low T_{bath} , the CB resonances are either thermally broadened for $\Gamma \ll 4k_{\text{B}}T$, lifetime broadened for $4k_{\text{B}}T \ll \Gamma$, or a combination of the two for $\Gamma \approx 4k_{\text{B}}T$, as discussed in the previous section. For bath temperatures between 30 mK and 60 mK, the extracted T remains constant. As we increase T_{bath} beyond 60 mK, T for two resonances (cyan and orange) increases with a slope of 1.00 ± 0.05 , in agreement with the thermally broadened regime. This is indicated by the dashed black line with a slope of

³This error bar does not account for potential experimental errors in consecutive experiments.

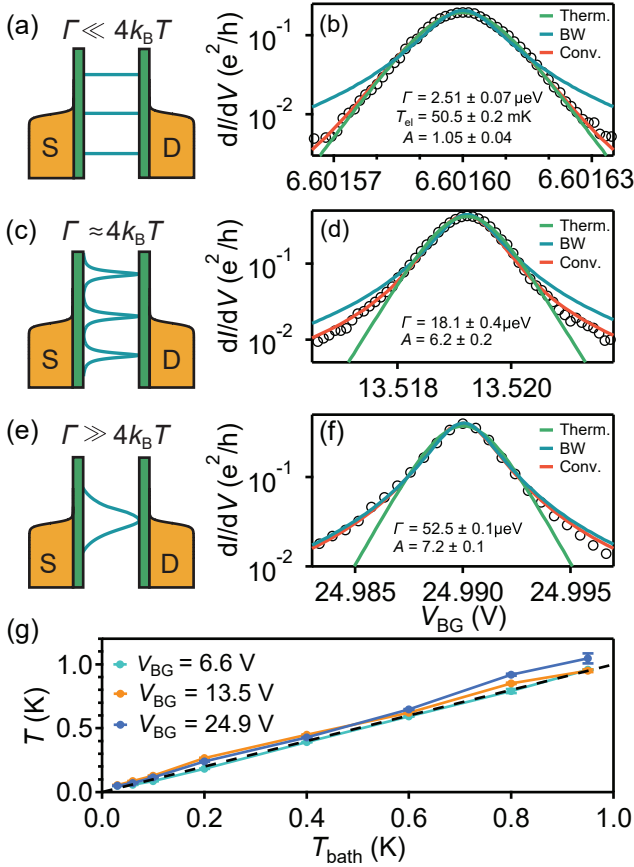


Figure 6.6. Evolution of the resonance line shapes: Differential conductance dI/dV as a function of V_{BG} for three resonances (b,d,f) in different regimes: (a) $\Gamma \ll 4k_B T$, (c) $\Gamma \approx 4k_B T$, and (e) $\Gamma \gg 4k_B T$. From (b), the electron temperature, $T = 50.5 \pm 0.2$ mK, was extracted and was fixed in the fits of (d) and (f). (g) T as a function of the bath temperature, T_{bath} , of the three resonances in (b), (d) and (f), respectively. T remains constant for $T_{bath} < 60$ mK, then increases with a slope of 1.00 ± 0.05 , as expected for the thermally broadened regime.

1. However, for the blue resonance, which is mostly lifetime broadened, the slope is 1.2 ± 0.1 , likely due to the resonance not fully transitioning into the temperature broadened regime. These experiments show that the electron and phonon system equilibrate at ~ 100 mK and that InAs/InP heterostructure QDs can be used as in-situ thermometers. In contrast to typical Coulomb blockade thermometers [236, 237], integrated QDs form an integral part of the device, which does not require thermal coupling to a separate device. We note that a series of thermal cycling takes roughly one week during which we did not observe any charge rearrangements, demonstrating a unique stability of this type of QD. Only tuning V_{BG} on the scale of several tens of volts results in a shift of the CB spectrum, which is reproducible and likely due to significant charging of substrate states.

6.5. Properties of the tunnel barriers

By investigating the functional dependence of the total tunnel coupling Γ and the asymmetry A on V_{BG} , we estimate the height and symmetry of the tunnel barriers formed by the InP segments. By fitting the CB resonances with Equation 6.2 and using the previously determined $T = 50.5$ mK, we extract Γ and A as a function of V_{BG} , as shown in Fig. 6.7(a) and (b), respectively. The red data points correspond to the CB resonances from Fig. 6.6(b),(d), and (f) measured with a high resolution in V_{BG} , while the black data points stem from resonances selected from a large gate sweep ($\Delta N \approx 150$) over 50 V measured with a lower resolution.

$\Gamma(V_{BG})$ is plotted in Fig. 6.7(a) and shows a systematic increase of Γ with increasing V_{BG} . Close to full depletion, we find a tunnel coupling of $\Gamma \approx 1$ μeV , which increases up to ~ 600 μeV for $V_{BG} = 42$ V. Comparing the dependence of $\Gamma(V_{BG})$ to a resonant tunneling model allows us to estimate V_0 . For this, we assume that an electron bounces back and fourth in the InAs segment between the two InP barriers at an attempt frequency ν and escapes through either of the barriers with a transmission probabilities, $T_{1,2}$, given by the rectangular tunnel barriers (see Eq. 2.3). Consequently, the total tunnel coupling Γ as a function of V_{BG} can be described by [238]:

$$\Gamma(V_{BG}) = \hbar\nu(T_1 + T_2) = 2\hbar\nu \left(1 + \frac{V_0^2 \sinh^2(\kappa(\phi)l)}{4\phi(V_0 - \phi)} \right)^{-1}, \quad (6.3)$$

with $T_1 = T_2$ for symmetric tunnel barriers, $\kappa(\phi) = \sqrt{2m_{\text{InP}}(V_0 - \phi(V_{BG}))/\hbar^2}$, $m_{\text{InP}} = 0.08m_e$ the effective electron mass in the InP segments [141], $\phi(V_{BG}) = e\alpha_{\text{LS}}(V_{BG} - V_P)$, α_{LS} the lever arm of the LSs, V_P the pinch-off gate voltage, $\nu = v_F/2s$ the attempt frequency with Fermi velocity $v_F = \sqrt{\frac{2\phi}{m_{\text{InAs}}}}$, and $m_{\text{InAs}} = 0.04m_e$ the effective electron mass in wurzite InAs [239]. The values

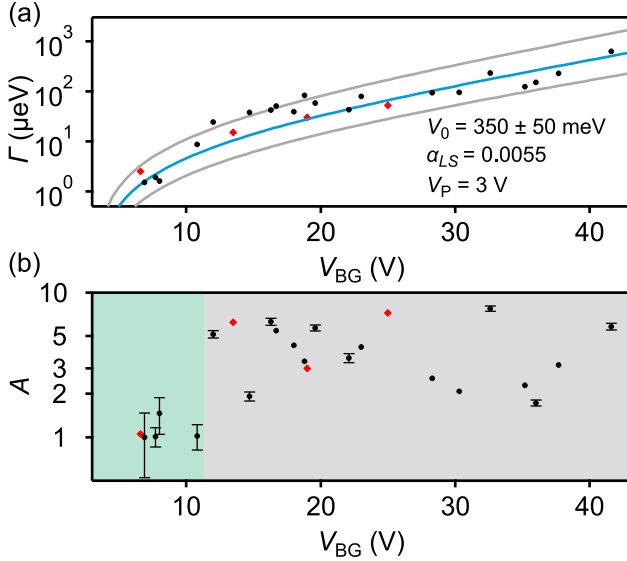


Figure 6.7. Evolution of the total tunnel coupling and asymmetry:

(a) Total tunnel coupling Γ as a function of the back gate voltage, V_{BG} . Γ systematically increases with V_{BG} in agreement with a double barrier model described in the main text. We estimate a conduction band edge offset, V_0 , between InAs and InP of 350 ± 50 meV (solid blue line), while the upper and lower solid gray lines are for $V_0 = 400$ meV and $V_0 = 300$ meV, respectively. (b) Asymmetry, $A = \Gamma_1/\Gamma_2$, as a function of V_{BG} . For low V_{BG} , $A \approx 1$, while for larger V_{BG} A scatters between 1 and 8 due to the modulation of the density of states in the lead segments. The red data points were extracted from the CB resonances in Fig. 6.6(b), (d), and (f) measured with a higher V_{BG} resolution than the black data points. Error bars smaller than the symbol size are not shown.

for the length of the InP segments and the QD were taken from the TEM analysis, with $\ell = \ell_{1/2} = 5.5$ nm and $s = 19.0$ nm, respectively.

From the best fit of Equation 6.3 to $\Gamma(V_{\text{BG}})$ (solid blue), we obtain the free parameters $V_0 = 350 \pm 50$ meV, $V_P = 3$ V, and $\alpha_{\text{LS}} = 0.0053$. V_0 is in good agreement with the calculated literature value of $V_0 = 400$ meV for strained InP in InAs NWs with our geometry [224]. The upper and lower solid gray lines are obtained using the same parameters and $V_0 = 300$ meV and $V_0 = 400$ meV, respectively. V_P agrees very well with the first CB resonances and α_{LS} is 4.5 times smaller than the lever arm to the QD, in qualitative agreement with the LSs being longer than the QD. Further discussion about α_{LS} is presented in Chapter 7.

Next, we investigate the asymmetry A as a function of V_{BG} in Fig. 6.7(b). The values of A scatter seemingly random between 1 and 8 for $V_{\text{BG}} > 10.5$ V. However, for $V_{\text{BG}} < 10.5$ V, $A \approx 1$ is constant, indicating highly symmetrical tunnel barriers. These characteristics of A can be understood qualitatively by the following argument. The modulation of the DOS in the confined LSs is determined by the single particle level spacing in the LSs, δE_{LS} , and the broadening of the energy levels in the LSs, Γ_{LS} . At E_F , $\delta E_{\text{LS}} = \pi \hbar v_F / L_{1/2}$ for a parabolic dispersion relation and thus $\delta E_{\text{LS}} \sim \delta E / 10$. In addition, the strong coupling between the LSs and the source or the drain contact gives rise to a larger Γ_{LS} than for the QD. With increasing V_{BG} , v_F also increases and we suspect that for $V_{\text{BG}} > 10.5$ V, $\delta E_{\text{LS}} > \Gamma_{\text{LS}}$, leading to a weaker overlap between the energy levels and thus to a stronger modulation of the DOS in the LSs. In contrast, for $V_{\text{BG}} < 10.5$ V, δE_{LS} decreases and the energy levels in the LSs overlap stronger, resulting in a weaker modulation of the DOS. Consequently, in the low gate regime, A reflects the asymmetry of the tunnel barriers $A \approx 1$, which are essentially equal in length and height.

6.6. Conclusion

In summary, we present an in-depth characterization of a QD formed by InP tunnel barriers and connected to metallic contacts via NW lead segments. For this system we demonstrate a nearly depletable QD with Coulomb diamonds that are exceptionally robust against charge rearrangements over a large gate range of 30 V, corresponding to ~ 124 electron states, and several months measurement time. By analyzing the line shapes of the CB resonances, we find a continuous transition from the lifetime to the thermally broadened regime and extract the electron temperature in the LSs. The QD shows a systematic and tunable increase in the tunnel coupling, based on which we estimate the conduction band edge offset between the InAs and the InP segments as $V_0 = 350 \pm 50$ meV. The InP segments act like ideal tunnel barriers with an asymmetry of $A = \Gamma_1 / \Gamma_2 \approx 1$, as targeted in the crystal growth. This is found

for low V_{BG} , where the modulation of the DOS in the LSs is negligible, while at larger V_{BG} the transport is modulated by the NW lead states. In conclusion, we demonstrate that integrated InAs/InP quantum dots are a promising platform for quantitative in situ electron tunneling spectroscopy and thermometry for future superconducting hybrid devices and other electronic and thermoelectrical applications.

7 Spectroscopy of the local density of states in nanowire leads

In the previous chapter, we investigated the fundamental properties of integrated quantum dots (QDs) in InAs/InP heterostructure nanowires (NWs). Now, we use the electrically and spatially well-defined integrated QD as a tunnel spectrometer to probe the local density of states (DOS) in the finite InAs nanowire segments between the QD and metallic reservoirs. We explicitly refer to these NW segments as lead segments. Evidence of a non-constant local DOS in the lead segments becomes clear in bias spectroscopy measurements such as Coulomb blockade (CB) diamond measurements where there exists resonances outside of the CB diamond that cannot be attributed to QD features such as excited states (ESs). These resonances are called lead states (LSs) and originate in the nanowire lead segments. LSs have been observed in InAs/InP heterostructure NWs [61], InAs crystal phase NWs [51], silicon single electron transistors [240–244] and graphene transistors [245]. However, a systematic study of them has yet been performed in a nanowire device with an integrated QD acting as a tunnel probe.

In this chapter, we present the first steps to a systematic study of the lead resonances. We begin with a brief description on how to distinguish states of the QD and LSs, then introduce the three different InAs/InP heterostructure NW devices that exhibit unique LS features. We focus on how the coupling between the reservoir and the lead segment influences the observed LSs, such as their slopes and broadenings depending on the chemical doping, as well as global and local gating effects. Following this, we introduce a three site model to explain the different slopes of the lead states then incorporate a resonant tunneling model to quantitatively describe the broadenings of the LSs.

Distinguishing between resonances originating from the quantum dot and the nanowire leads

Based on the previous results in Chapter 6, we first discuss what distinguishes resonances originating from the QD and the nanowire leads. Figure 7.1 shows a typical Coulomb blockade diamond measurement for an InAs/InP heterostructure NW. Outside of the CB region, we observe several resonances, but can we attribute all of these to purely the QD?

To answer this question, we first assume that the system can be modeled as a QD directly coupled to two reservoirs with a constant DOS. In this system, one would expect that only resonances in the CB diamond measurement arise from transport mechanisms via the QD, for example, transport via ESs of the QD.

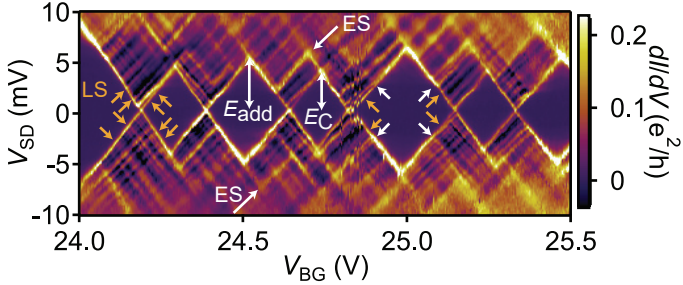


Figure 7.1. Coulomb blockade diamond: Differential conductance, dI/dV , as a function of source drain bias voltage, V_{SD} , and back gate voltage, V_{BG} . We find several resonances outside of the CB diamond pattern corresponding to excited states (ES) of the quantum dot indicated by a white arrow, as well as the lead states (LS) arising from the nanowire lead segments, indicated by an orange arrow.

We first consider where the excited state resonances are expected to appear by considering the quantum dot's addition energy, E_{add} , and charging energy, E_C , to determine its level spacing, δE_{QD} . As previously stated in Chapter 6, the region in Fig. 7.1 exhibits a clear even-odd pattern with $E_{add} = (5.5 \pm 0.1)$ meV and $E_C = (4.2 \pm 0.1)$ meV. From the difference between E_{add} and E_C , we find $\delta E_{QD} = (1.3 \pm 0.2)$ meV. This value is consistent with $\delta E_{QD} = (1.5 \pm 0.2)$ meV from the corresponding resonance indicated by ES (white) in Fig. 7.1. The ES resonances have a slope similar to the QD ground state (GS) resonances (i.e. the CB diamond edge), large δE_{QD} and amplitudes, and can often be determined from cotunneling lines present in the Coulomb blockade region. The ES resonances are indicated in Fig. 7.1 by ES (white arrows). However we find this analysis only captures a small portion of the features observed in Fig. 7.1 and there exists several resonances with smaller level spacings and smaller slopes outside of the CB diamond that can be clearly resolved. A few of these resonances are indicated in Fig. 7.1 by LS (orange arrows).

	Excited State	Lead State
Origin	Quantum dot	Nanowire leads
Slope	Similar to QD GS slope	Smaller than QD GS slope
Level spacing	Large	Small
Amplitudes	Large	Small

Table 7.1. Summary of features attributed to excited and lead states.

To explain the origin of the additional resonances, we now take into account the finite InAs nanowire lead segments between the reservoirs and the QD. We define $LS1$ ($LS2$) as the nanowire lead segment between the source (drain) and the QD. In principle, these lead segments are quasi one-dimensional due to confinement in the transverse directions, however further confinement in the axial direction, e.g. due to tunnel barrier formation at the metal-NW interface, can result in the formation of quasi zero-dimensional Fabry-Pérot like bound states in the lead segments.

In general, the two lead DOSs are made up of several overlapping states in each of the two NW lead segments with widths mainly determined by the coupling to the reservoirs. If the states strongly overlap, the DOS of the lead segments will be approximately constant resulting in a constant background conductance outside of the CB diamond. However, if they weakly overlap there is a strong modulation of the lead DOSs resulting in additional resonances and strong negative differential conductance outside of the CB region. Lead states outside of the CB blockade region are observed when the a peak in the lead DOS enters the bias window and its electrochemical potential is aligned with the electrochemical potential of the QD. From Fig. 7.1, we find two sets of lead states with positive and negative slopes ($\Delta V_{SD}/\Delta V_{BG}$). We will later demonstrate in Sec. 7.2 that lead states with positive (negative) slopes originate from $LS1$ ($LS2$).

To explain the small level spacings, $\delta E_{LS1/2}$, observed in the measurement, we consider the length of the lead segments. Since the lead segments are typically an order of magnitude longer than the QD, $\delta E_{LS1/2}$, are typically much smaller, i.e. $\delta E_{LS1/2} \ll \delta E_{QD}$. In addition, unlike excited state resonances, we find that their slopes are smaller compared to resonances originating from the QD (CB diamond edges and QD excited states).

In summary, we observe two sets of resonances: ES resonances originating from the QD and LSs resonances originating from the NW leads. Table 7.1 summarizes the main differences between them and can be used as a basis for identifying whether a resonance originates from the leads or the QD.

7.1. Devices and characterization

In this chapter, we present measurements from three different InAs/InP heterostructure NW devices: Device A, B, and C. All devices were fabricated in a similar fashion, as discussed in Chapter 4. However, each device is not identical and exhibit unique features allowing for a deeper understanding of the LSs.

For the analysis later, we need to extract the QD and LS slopes for each device. The positive and negative QD slopes, β_+ and β_- , are defined in Fig. 2.7. The slope of lead states ($\Delta V_{SD}/\Delta V_{BG}$) with positive (negative) slopes are defined as s_{LS1} (s_{LS2}). The choice of this notation will become clear in Sec. 7.2.

Device A

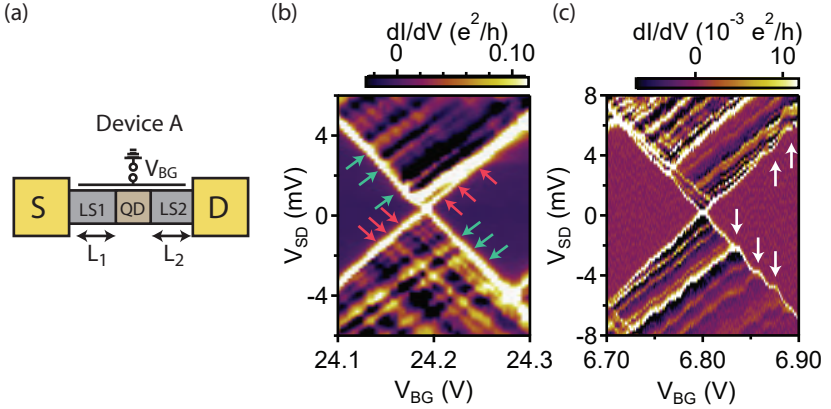


Figure 7.2. Schematic and Coulomb blockade diamonds for device A: (a) Schematic of an InAs/InP heterostructure nanowire with an integrated quantum dot (QD) (brown) coupled to two InAs nanowire (grey) leads, $LS1$ and $LS2$, of lengths, $L_1 \approx 350$ nm and $L_2 \approx 600$ nm, respectively. $LS1$ and $LS2$ are electrically contacted to either a source (S) or drain (D) reservoir made of Ti/Au. The electrochemical potential in the entire NW (leads+NW) is tuned by applying a back gate voltage, V_{BG} . (b)-(c) Differential conductance, dI/dV , as a function of back gate voltage, V_{BG} , and source drain bias, V_{SD} . In (b), we find two sets of lead states, indicated by the green and red arrows, with slopes not equal to the QD diamond edge and have smaller amplitudes. In (c), we find effects due to discrete charge transport through one of the lead segments, indicated by the white arrows.

A schematic illustrating Device A is depicted in Fig. 7.2(a). The integrated QD (brown) is coupled to two InAs lead segments (grey), $LS1$ and $LS2$, with lengths $L_1 \approx 350$ nm and $L_2 \approx 600$ nm. $LS1$ and $LS2$ are further coupled to either a source (S) or drain (D) reservoir made of Ti/Au (yellow). The electrochemical potential of $LS1$, $LS2$, and the QD are tuned by a global back gate (BG) with voltage, V_{BG} . This is the same device presented in Chapter 6.

Figure 7.2(b) and (c) show high resolution Coulomb blockade (CB) diamond measurements in this device exhibiting several LSs outside of the CB diamond. First, we focus on the properties of the QD. The QD is characterized by its single particle level spacing, slopes, and broadening. The single particle level spacing for this CB diamond in (b) is $\delta E_{QD} \approx 7$ meV and in (c) $\delta E_{QD} \approx 2.6$ meV. We estimate the broadening to be $\Gamma_{QD} \approx 200$ μ eV from Fig. 6.7(a).

The positive and negative slopes of the CB diamond edge are equal in both CB diamonds and are given by $\beta_+ = 0.038 \pm 0.001$ and $\beta_- = -0.050 \pm 0.001$. In addition, we observe two sets of lead resonances in (b), corresponding to $LS1$ (green arrows) and $LS2$ (red arrows) with lead level spacings, $\delta E_{LS1/2} \ll \delta E_{QD}$. We find that the resonances corresponding to $LS1$ and $LS2$ have slopes of $s_{LS1} = 0.033 \pm 0.001$ and $s_{LS2} = -0.033 \pm 0.001$, respectively. The slopes of the lead resonances are nearly parallel to the diamond edge, suggesting the lead segments are well, but not perfectly, coupled to the reservoirs. In addition, we find regions of negative differential conductance (NDC), a feature of weakly overlapping lead states. Furthermore, the conductance amplitude of the LSs is a factor of 3 – 10 smaller than that of the QD diamond edge.

In (c), we find that the lead resonances and the QD diamond edge exhibit "jumps", indicated by the white arrows. We speculate this is due effects of discrete electron charge transfer between the reservoir and $LS2$. At low V_{BG} values the nanowire lead segment is likely nearly depleted, meaning when one electron tunnels onto the lead segment from the reservoir the capacitance of the lead segment changes. This then induces a voltage in the QD, leading to a change in its electrochemical potential. Therefore, the QD acts as a charge sensor for the leads [246, 247].

Device B

In Device B, the effect of increasing the charge carrier concentration in the NW is investigated. Figure 7.3(a) illustrates a schematic of an selenium doped InAs/InP heterostructure NW. In this device, the source (S) reservoir (blue) made of titanium/aluminum (Ti/Al) and the the drain (D) is Ti/Au (yellow). The NW region beneath the source reservoir consists of InAs with selenium (Se) dopants (white). The Se dopants increase the carrier concentration, thereby reducing the Schottky barrier at the interface, resulting in better electrical contact [248]. We note that between the Se-doped region and the InP tunnel barrier, there exists 100 nm of undoped InAs. The corresponding lead

segment lengths for Device B are: $L_1 = 100$ nm and $L_2 = 300$ nm.

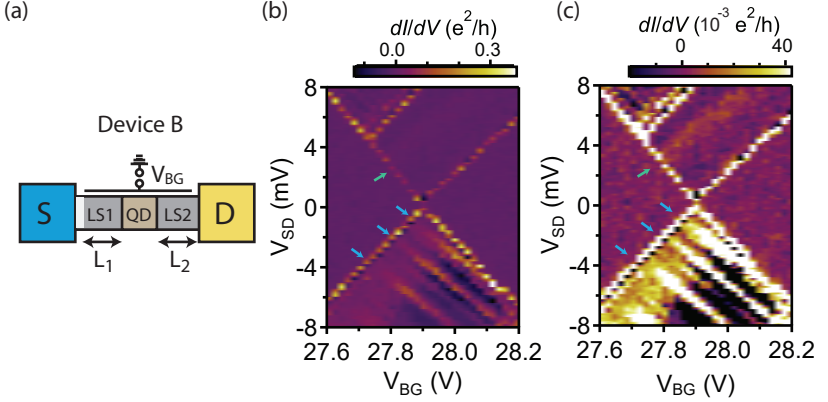


Figure 7.3. Schematic and Coulomb blockade diamonds for device B: (a) Schematic of a selenium doped InAs/InP heterostructure nanowire (NW) device. In this device, $LS1$ consists of InAs with Se dopants to increase the carrier concentration of the NW lead. There exists 100 nm of undoped InAs between the quantum dot (QD) and where the doped region begins. The corresponding lead segment lengths are: $L_1 = 100$ nm and $L_2 = 300$ nm. (b) Two sets of lead states corresponding to $LS1$ (green arrow) and $LS2$ (blue arrows) outside of the Coulomb blockade diamond. (c) Same as (b), but with higher contrast to see the LS indicated by the green arrow.

A Coulomb blockade diamond is shown in Fig. 7.3(b). Here, we find $\delta E_{QD} \approx 4.7$ meV and $\beta_+ = 0.017$ and $\beta_- = -0.024$ for the QD. Now, only one set of lead resonances, those corresponding to $LS2$, can be clearly resolved. The lead resonances in $LS1$ are still present (green arrow), however they are broader than those corresponding to $LS2$. We speculate that this is due to the increased carrier concentration in $LS1$ from the Se-dopants resulting in better coupling to the reservoir. To better illustrate this, Fig. 7.3(c) shows the same as (b), but with a larger contrast. By increasing the carrier concentration, the lead states couple stronger to the source reservoir and appear to be broadened. The slopes of the LSs in the device are: $s_{LS1} = 0.016$ and $s_{LS2} = -0.014$. Now, we find that $s_{LS1} \approx \beta_+$, suggesting that $LS1$ is strongly coupled to the source reservoir.

Device C

Device C was used to investigate the gate dependence of the lead states in one lead. Figure 7.4(a) illustrates a schematic of the device. In this device, the source reservoir (S) consists of Ti/Al, while the drain (D) reservoir is Ti/Au. In addition, there is a local metallic (Ti/Au) side gate (SG) that tunes the electrochemical potential in $LS2$, as well as the QD. $LS1$ and $LS2$ have lengths $L_1 \approx 50$ nm and $L_2 \approx 350$ nm. While the device has a superconducting reservoir (Ti/Al) and a proximity induced superconducting gap is observed (see Chapter 8), we restrict our discussion to features outside of the superconducting gap ($\Delta^* \approx 125$ μ eV).

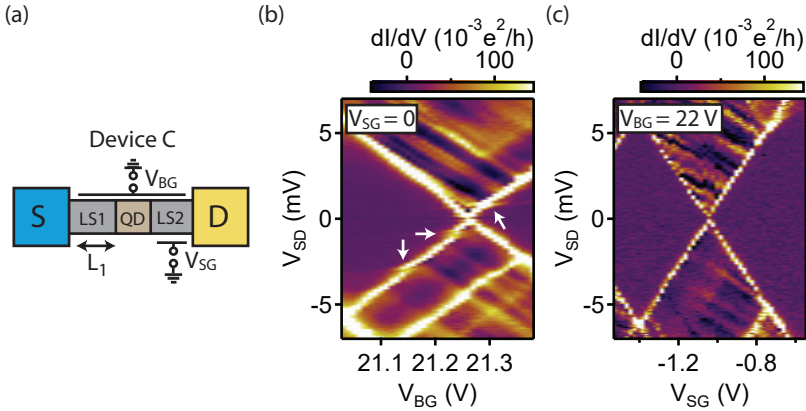


Figure 7.4. Schematic and Coulomb blockade diamonds for device C: (a) Schematic of an InAs/InP heterostructure NW is coupled to one superconducting contact (blue) and one normal metal contact (yellow). The lengths of the lead segments, $LS1$ and $LS2$, are $L_1 \approx 50$ nm and $L_2 \approx 350$ nm, respectively. In this device, a side gate (SG) is positioned perpendicular to $LS2$ that tunes the electrochemical potential in $LS2$ and the QD. (b)-(c) Coulomb blockade diamond measurements as a function of (b) back gate voltage, V_{BG} , and (c) side gate voltage, V_{SG} . We find a clear difference between the slopes of the lead states. The white arrow indicates a possible hybridization between the lead state and quantum dot state.

Figure 7.4(b) shows the differential conductance, dI/dV , as a function of V_{SD} and V_{BG} for $V_{SG} = 0$. We observe several lead resonances with negative slopes outside of the CB diamond that we attribute to bound states in $LS2$. Figure 7.4(c) shows dI/dV as a function of V_{SD} and V_{SG} for $V_{BG} = 22$ V. Once again, we find lead resonances corresponding to bound states in $LS2$, however

	Device A	Device B	Device C
NW Type	InAs/InP NW	Se-doped InAs/InP NW	InAs/InP NW
L_1 (nm)	350	100	50
L_2 (nm)	600	300	350
Reservoirs	Ti/Au	Ti/Al + Ti/Au	Ti/Al + Ti/Au
Features	Two sets of LSs, different LS slopes, small level spacing, charge sensing	Large broadening of lead states	Gating effects in LS2 by a side gate, LS+QD hybridization

Table 7.2. Summary of devices A, B, and C.

now with different slopes than in (a). We attribute this to gating effects by V_{SG} that change the coupling between $LS2$ and the drain reservoir or the coupling between the QD and $LS2$. In addition, we find three anticrossings in (b) that suggest the lead states and QD states become hybridized despite the large integrated tunnel barriers in the system. These anticrossings are not found in (c). We perform a similar analysis as in device A and B to extract the slopes of the QD and the lead states for later. From the slopes of the QD diamond edge and lead resonances formed in $LS2$, we find in (b) $\beta_+ = 0.022$, $\beta_- = -0.021$, $s_{LS2} = -0.019$. Similarly for (c), we find $\beta_+ = 0.017$, $\beta_- = -0.017$, $s_{LS2} = -0.0042$. Therefore, we deduce that V_{SG} leads to a large change in s_{LS2} .

Table 7.2 summarizes devices A, B, and C presented in this chapter and the unique features they exhibit. In the following, we discuss LSs and describe how these conductance features arise from the resulting modulation of the local DOS in the lead segments.

7.2. Lead states

We now turn our focus to the different slopes observed in the experiment. We first introduce our general InAs/InP heterostructure nanowire system and its corresponding electrostatic model then discuss what features our model can capture.

As previously discussed, lead states originate from quantum confinement in the lead regions, giving rise to a discrete energy spectrum in the lead segments that we characterized by a non-constant DOS. We consider an InAs/InP heterostructure nanowire where the QD is not directly coupled to the reservoirs, but rather to NW lead segments, as illustrated in Fig. 7.5(a). Here, an InAs NW (grey) with a QD formed by two in situ grown InP tunnel barriers (black) separates two lead segments, $LS1$ and $LS2$, that are electrically contacted to either a source (S) or drain (D) reservoir (yellow).

We assume two tunnel barriers (brown) are formed at the lead-reservoir interface, for example, by the presence of a Schottky barrier. If the tunnel barrier at the $LS1/LS2$ -reservoir interface is sufficiently large, the transmission between the wire and the reservoir will be reduced and in-bound electrons are not perfectly transmitted into the reservoir, but are reflected at the lead-reservoir

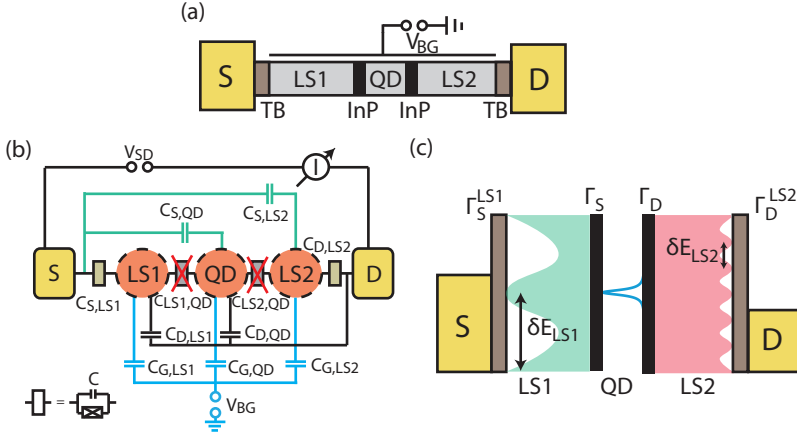


Figure 7.5. Model of the nanowire system: (a) Illustration of an integrated quantum dot (QD) coupled to two InAs nanowire (grey) lead segments, $LS1$ and $LS2$, of lengths, L_1 and L_2 , respectively. $LS1$ and $LS2$ are further electrically contacted to source (S) and drain (D) reservoirs (yellow). Four tunnel barriers (TB) are present in the system: two InP tunnel barriers (black) and two tunnel barriers formed at the $LS1/LS2$ -reservoir interface (brown). (b) Electrochemical potential diagram of the system. The two InP tunnel barriers confine the region between them forming a QD. Confinement from the tunnel barriers at the lead-reservoir interface results in QD-like characteristics in $LS1$ and $LS2$. The local density of states (DOS) is illustrated as strongly modulated (green) or weakly modulated (red).

interface. This leads to the electron wave functions becoming confined in $LS1$ and $LS2$ and to the formation Fabry-Pérot- like bound states in these regions. These bound states exhibit QD-like characteristics such as: discrete energies, E_{LS1} and E_{LS2} , single particle level spacings, δE_{LS1} and δE_{LS2} , and tunnel couplings, Γ_{LS1} and Γ_{LS2} , respectively. Furthermore, since the electrons are strongly reflected at the QD tunnel barrier, the widths of these states are determined mostly by the coupling to the source and drain contacts, $\Gamma_{LS1} \approx \Gamma_{LS1}^S$ and $\Gamma_{LS2} \approx \Gamma_{LS2}^D$ respectively.

To describe the electrostatics of the system, we assume a three site model to qualitatively and to some extent quantitatively understand the presented experimental findings, as illustrated in Fig. 7.5(b). The source (S), back gate (BG), and drain (D) all couple capacitively to $LS1$, the QD, and $LS2$. The capacitances are denoted as $C_{S/G/D,LS1/QD/LS2}$ where, for example, $C_{S,LS1}$

means the capacitive coupling between the source and $LS1$. We apply a bias to the source, V_S , while keeping the drain grounded, $V_D = 0$. We omit any interdot coupling between $LS1$ and $LS2$ (red cross). However we observe charging effects in Fig. 7.2(c) as well as hybridization between the LS and QD in Fig. 7.4(c).

The electrochemical potential diagram for this system is illustrated in Fig. 7.5(b). Here, the discrete energy states of the quantum dot, as well as the energy states in the lead regions characterized by a non-constant density of states, is shown. Two possible scenarios of the DOS in $LS1$ (green) and $LS2$ (red) are illustrated. In $LS1$, $\delta E_{LS1} \gg \Gamma_{LS1}$, thus the electron states in this region are weakly overlapping, leading to a strong modulation of the DOS. However, in $LS2$, $\delta E_{LS2} \ll \Gamma_{LS2}$, resulting in strong overlap between the electron states and thus a weakly modulated DOS forming a near constant energy spectrum.

7.3. Lead state slopes

The slopes of the lead resonances give valuable information about the capacitive coupling between the reservoir and the lead segment. To further describe the transport properties via lead states, we consider an electrochemical potential diagram of a QD. Here, we simplify the local DOS in $LS1$ and $LS2$ to a single peak that is otherwise constant in energy and restrict ourselves to only positive V_{SD} values. We also assume that the DOS of one lead segment is constant.

Five electrochemical potentials play a role in the transport processes here: the electrochemical potential of $LS1$ (μ_{LS1}), of the source reservoir (μ_S), of the QD (μ_{QD}), of $LS2$ (μ_{LS2}), and the drain reservoir (μ_D). In addition, four lever arms are considered: the lever arm between the source and $LS1$ ($\alpha_{S,LS1} = \frac{C_{S,LS1}}{C_{LS1}}$), the lever arm between the drain reservoir and $LS2$ ($\alpha_{D,LS2} = \frac{C_{D,LS2}}{C_{LS2}}$), the lever arm between the gate and $LS1$ ($\alpha_{G,LS1} = \frac{C_{G,LS1}}{C_{LS1}}$), and the lever arm between the gate and $LS2$ ($\alpha_{G,LS2} = \frac{C_{G,LS2}}{C_{LS2}}$).

Strong coupling to reservoirs

We first consider the case where $LS1$ is capacitively strongly coupled to the source reservoir ($\alpha_{S,LS1} = 1$) or $LS2$ is strongly coupled to the drain reservoir ($\alpha_{D,LS2} = 1$). Figure 7.6 shows an illustration of a CB diamond for positive V_{SD} whose diamond edges are indicated by black lines and two lead states originating from $LS1$ ($LS2$) are indicated by a dashed green (red) line. The inset shows a sketch of the electrochemical potential at four positions along the dashed green and red lines.

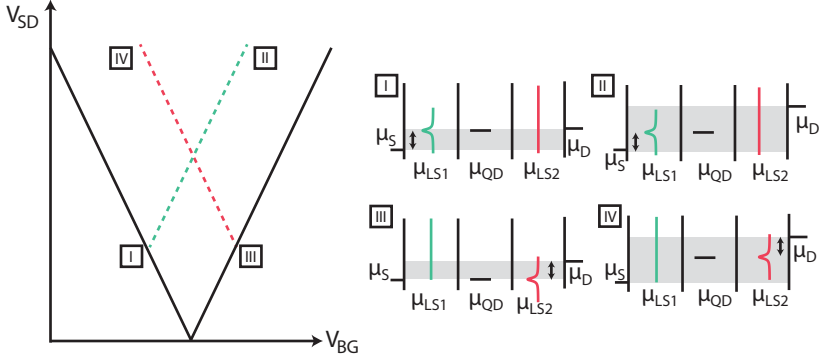


Figure 7.6. Lead states when strongly coupled to the reservoirs: Illustration of the lead states outside of the Coulomb blockade diamond for a quantum dot (QD) coupled to two lead segments, $LS1$ and $LS2$, exhibiting a single peak in its local density of states (DOS). (I)-(IV) Electrochemical potential diagram of the lead resonances. The dashed green line corresponds to a peak in the local DOS of $LS1$ entering the bias window ($eV_{SD} = \mu_D - \mu_S$). Similarly, the dashed red line corresponds to a peak in the local DOS of $LS2$ entering the bias window.

We begin with discussing transport along the dashed green line. Since $\alpha_{S,LS1} = 1$, the green resonance is always at the same energy distance to μ_S , indicated by the black arrow in (I). At point (I), a finite bias is applied such that $\mu_S < \mu_D$ and the peak in μ_{LS1} is aligned with μ_{QD} , while the DOS in $LS2$ is constant. The QD is now acting as an energy filter and we only get transmission if μ_{QD} and μ_{LS1} align. Therefore, there is a net electron flow from the drain to the source contact, resulting in a peak in differential conductance. As we move along the dashed green line to point (II), the bias window is increased, the latter requires that the μ_{QD} moves with μ_{LS1} and thus with μ_S , therefore the resonance has the same positive slope as QD diamonds. Since $\sum_i \alpha_{i,LS} < 1$, the states cannot move faster in energy than the bias.

A similar situation happens for transport along the dashed red line. Here, $\alpha_{D,LS2} = 1$, and the red resonance is always at the same energy distance to μ_D , indicated by the black arrow in (III) and (IV). Starting from point (III), now the DOS in $LS1$ is constant and a peak in μ_{LS2} is aligned with μ_{QD} . Transmission only occurs when μ_{QD} and μ_{LS2} align and the QD acts once again as an energy filter. Continuing along to point (IV), the bias window is increased, therefore μ_{QD} moves with μ_{LS2} and thus μ_D . This results in the lead resonance having the same slope as the negative slope of the QD diamond.

Weaker coupling to reservoirs

Previously, we assumed that the the lead segments and their corresponding reservoirs were strongly coupled, meaning that $\mu_{LS1/2}$ moves perfectly with $\mu_{S/D}$. This results in the slopes of the lead resonances running parallel with QD diamond edge. However, in device A (Fig. 7.2(b)) we observe that the slopes of the lead resonance are not parallel to the QD diamond. To explain this finding, we now assume that the capacitive coupling between the lead segments and reservoirs is weaker, i.e. $\alpha_{S,LS1} < 1$ and $\alpha_{D,LS2} < 1$.

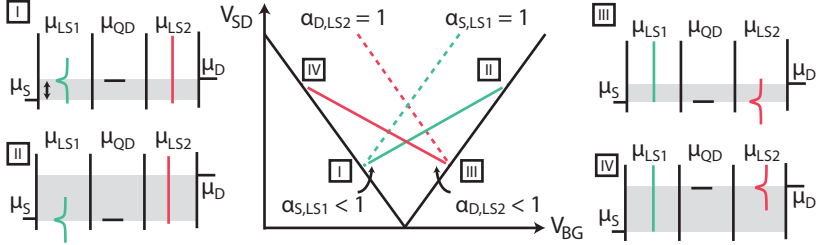


Figure 7.7. Lead states when weakly coupled to the reservoirs: Schematic to qualitatively explain gate dependence of lead state resonances with respect to quantum dot Coulomb blockade diamond with finite bias voltage, V_{SD} , and back gate voltage, V_{BG} . The green(red) lines represent resonances when a peak in the local density of states of $LS1(LS2)$ is aligned with the electrochemical potential of the quantum dot. The slopes of the resonances depends on the coupling between the $LS1(LS2)$ and the source(drain) reservoir, characterized here by $\alpha_{S,LS1}(\alpha_{D,LS2})$. For weak coupling, $\alpha_{D,LS2} < 1$ or $\alpha_{S,LS1} < 1$, the slopes become shallower.

Figure 7.7 illustrates a schematic of the slopes of the lead resonances in $LS1$ (green) and $LS2$ (red) for strong coupling (dashed line) and weaker coupling (solid line). First, we consider lead resonances in $LS1$ (dashed green line). Since $\alpha_{S,LS1} < 1$, μ_{LS1} does not perfectly follow μ_S , but "lags" behind it. Therefore, when the bias window is increased between (I) and (II), the distance between the peak in the DOS in $LS1$ and μ_S becomes larger. This distance is indicated by the black arrows in (I) and (II). In addition, less V_{BG} is required to shift μ_{QD} such that it remains aligned to μ_{LS1} . This results in the slope of the LS becoming shallower and not parallel to the QD diamond. Similarly, for LSs in $LS2$ (dashed red line), the peak in the DOS does not perfectly follow μ_D for increasing bias since $\alpha_{D,LS2} < 1$. Therefore, the distance between μ_D and the peak in the DOS becomes larger. Also, μ_{QD} is shifted less by V_{BG} due to the smaller shift in μ_{LS2} .

Using this model, we can derive an expression for the slope of the lead states, neglecting interdot couplings, by considering transport through the QD and one lead segment. Here, we note again that a finite V_{SD} is applied to the source contact while the drain remains grounded. Therefore, current is allowed when the electrochemical potential of the QD and lead segment are aligned:

$$\begin{aligned} \mu_{LS1/2} &= \mu_{QD} \\ \Rightarrow -e\alpha_{BG,LS1/2}V_{BG} - e\alpha_{S,LS1/2}V_{SD} &= -e\alpha_{BG,QD}V_{BG} - e\alpha_{S,QD}V_{SD} \end{aligned} \quad (7.1)$$

By rearranging the equation and solving for $s_{LS1/2} := \frac{V_{SD}}{V_{BG}}$, we find:

$$s_{LS1/2} = -\frac{\alpha_{BG,LS1/2} - \alpha_{BG,QD}}{\alpha_{S,LS1/2} - \alpha_{S,QD}}. \quad (7.2)$$

Using this equation, we would like to extract all of the lever arms of the system. This equation has in principle five unknowns, however $s_{LS1/2}$, $\alpha_{BG,QD}$, and $\alpha_{S,QD}$ can be determined by analyzing the slopes CB diamond measurement. Since this leaves two more unknowns and only one equation, we make the assumption that $\alpha_{BG,LS} = 0.005$. We support this assumption by noting similar values were reported in Chapter 6 and in Ref. [104] using the same methodology.

Device A

From device A, we found the resonances in $LS1$ have a slope of $s_{LS1} = |s_{LS2}| = 0.033 \pm 0.001$. From the slopes of the QD, $\beta_+ = 0.038 \pm 0.001$ and $\beta_- = -0.050 \pm 0.001$, we find $\alpha_{G,QD} = 0.02$ and $\alpha_{S,QD} = \alpha_{D,QD} = 0.49$. Therefore, from Eq. 7.2, we find $\alpha_{S,LS1} = 0.97$ and $\alpha_{D,LS1} = 0.025$. Similarly, for the resonances in $LS2$, we find $\alpha_{D,LS2} = 0.97$ and $\alpha_{S,LS2} = 0.025$. Therefore, both lead segments do not perfectly couple to their respective reservoir, leading to slopes that do not perfectly follow the QD diamond edge. The slopes and lever arms for device A are summarized in Table 7.3.

	QD	LS1	LS2
Positive slope	$\beta_+ = 0.038$	$s_{LS1} = 0.033$	-
Negative slope	$\beta_- = -0.050$	-	$s_{LS2} = -0.033$
Lever Arms	$\alpha_{G,QD} = 0.02$	$\alpha_{G,LS1} = 0.005$	$\alpha_{G,LS2} = 0.005$
	$\alpha_{S,QD} = 0.49$	$\alpha_{S,LS1} = 0.97$	$\alpha_{S,LS2} = 0.025$
	$\alpha_{D,QD} = 0.49$	$\alpha_{D,LS1} = 0.025$	$\alpha_{D,LS2} = 0.97$

Table 7.3. Summary of the slopes and lever arms found in device A.

Device B

We apply the same method for device B. Previously, we found the resonances in $LS1$ have a slope of $s_{LS1} = 0.016 \pm 0.001$, while the QD has slope $\beta_+ = 0.017 \pm 0.001$. We expect that $\alpha_{S,LS1} \approx 1$, since $s_{LS1} \approx \beta_+$. The lever arms of the QD were determined by the slopes of the diamond edges and are: $\alpha_{G,QD} = 0.01$, $\alpha_{S,QD} = 0.43$, and $\alpha_{D,QD} = 0.56$. Using Eq. 7.2, we find $\alpha_{S,LS1} = 1$ and $\alpha_{D,LS1} = 0$. We note that it is physically impossible that $\alpha_{G,LS1} = \alpha_{D,LS1} = 0$, however even a slight increase of $\alpha_{G,LS1} = 0.005$ results in a change $s_{LS1} = 0.016$ to $s_{LS1} = 0.007$. Therefore, we can only state that the $\alpha_{G,LS1} \ll 0.005$. Similarly, for $LS2$, $s_{LS2} = -0.014$, we find $\alpha_{D,LS2} = 0.87$ and $\alpha_{S,LS2} = 0.125$ with $\alpha_{G,LS2} = 0.005$. Now, we find a difference in couplings between the lead segment with Se dopants ($LS1$) and the one without ($LS2$). We attribute the strong coupling between the source reservoir and $LS1$ to the larger carrier concentration in the Se-doped InAs. The slopes and lever arms for device B are summarized in Table 7.4.

	QD	LS1	LS2
Positive slope	$\beta_+ = 0.017$	$s_{LS1} = 0.016$	-
Negative slope	$\beta_- = -0.024$	-	$s_{LS2} = -0.014$
Lever Arms	$\alpha_{G,QD} = 0.01$	$\alpha_{G,LS1} < 0.005$	$\alpha_{G,LS2} = 0.005$
	$\alpha_{S,QD} = 0.43$	$\alpha_{S,LS1} \approx 1$	$\alpha_{S,LS2} = 0.125$
	$\alpha_{D,QD} = 0.56$	$\alpha_{D,LS1} \approx 0$	$\alpha_{D,LS2} = 0.87$

Table 7.4. Summary of the slopes and lever arms found in device B.

Device C

In device C, a similar analysis was performed to determine the coupling between $LS2$ and the drain reservoir. For Fig. 7.4(b) with $V_{SG} = 0$ V, we find $\alpha_{D,LS2} = 0.75$ with $\alpha_{G,QD} = 0.01$, $\alpha_{G,LS2} = 0.005$, and $s_{LS2} = -0.019$, suggesting that $LS2$ couples weakly to the drain reservoir.

Further analysis of how the coupling changes in Fig. 7.4(c) is challenging due to $\alpha_{D,LS2}$ and $\alpha_{G,LS2}$ changing simultaneously from the voltage applied to the side gate. Therefore, we neglect to comment further on this, but speculate that $\alpha_{G,LS2}$ will increase and $\alpha_{D,LS2}$ will decrease, leading to the shallower slopes of the lead states in $LS2$ observed in the measurement. However, V_{SG} could also tune the interdot coupling between $LS2$ and the QD, which we do not take into account in this simple model.

7.4. Broadening of lead states

We now investigate the broadening of the lead resonance by numerically evaluating the simplified model presented in Fig. 7.5(a), neglecting interdot coupling between $LS1/2$ and the QD. We restrict our model for transport through a single quantum dot energy level with a large E_C . A dc bias voltage, V_S , is applied to the source reservoir and the drain reservoir is kept grounded, $V_D = 0$. The current through the system, I , is given by the total transmission, $T(E)$, through the system [65, 232, 235]:

$$I = \frac{e}{h} \int T(E) \cdot (f_S(E) - f_D(E)) dE, \quad (7.3)$$

where $T(E) = T_{LS1}(E) \cdot T_{QD}(E) \cdot T_{LS2}(E)$ is the product of transmission probabilities for LS1, the QD, and LS2 in the weak tunnel coupling regime. $f_{S/D}(E) = 1/(1 + \exp((E + eV_{S/D})/k_B T_e))$ are the Fermi-Dirac distributions of the source (S) and drain (D) reservoirs at temperature T_e .

The QD is characterized by its transmission probability, $T_{QD}(E)$, described by the Breit-Wigner (BW) transmission function [65, 232, 235]:

$$T_{QD}(E) = (\Gamma_1 \Gamma_2) / ((E - \mu_{QD})^2 + \Gamma^2 / 4), \quad (7.4)$$

with QD level broadening $\Gamma = \Gamma_1 + \Gamma_2$ and electrochemical potential $\mu_{QD} = -|e|\alpha_{S,QD}V_S - |e|\alpha_{G,QD}V_G - |e|\alpha_{D,QD}V_D$ [65]. To implement the modulated DOS in LS1 and LS2, we model the transmission probability of the LSs, $T_{LS1/2}(E)$, by the sum of N number of BW transmission functions:

$$T_{LS1/2}(E) = \sum_{n=1}^N \frac{(\Gamma_{LS1/2}^n)^2}{\left(E - \mu_{LS1/2} - n \cdot \delta E_{LS1/2}^n\right)^2 + \frac{1}{4} \left(\Gamma_{LS1/2}^n\right)^2}, \quad (7.5)$$

where $\Gamma_{LS1/2}^n = \Gamma_{LS1/2}^{n,1} + \Gamma_{LS1/2}^{n,2}$ is the broadening of the n th LS in LS1 or LS2, $\delta E_{LS1/2}^n$ is the level spacing of the n th state of LS1 or LS2, and $\mu_{LS1/2} = -|e|\alpha_{S,LS1/2}V_S - |e|\alpha_{G,LS1/2}V_G - |e|\alpha_{D,LS1/2}V_D$ are the electrochemical potentials in LS1 and LS2. dI/dV is calculated numerically.

In this model, the capacitive coupling between the leads and the QD is not taken into account. In addition, we assume that the leads are strongly capacitively coupled to the reservoirs and only weakly capacitively coupled to the gate, expressed here by the lever arms.

As stated previously, our goal is to extract the broadening of the resonances, however this is not trivial, because we convolute three transmission functions and two Fermi-Dirac functions, so that the amplitudes are not directly the energies and transmission maximum of the individual sites. We expect that

the model captures the position, since we use capacitances to model the electrostatics, except for hybridization of wave functions observed in Fig. 7.4(b), which we do not take into account.

Device A

Figure 7.8 shows the (a) measured and (b) modeled Coulomb blockade diamond. For the model, we used the QD and LS lever arms that can be found in Table 7.3. In addition, each LS was added corresponding to their spacings extracted from the experiment. Their individual energies, $E_{LS1/2}$, slopes, $s_{LS1/2}$, and level spacings, $\delta E_{LS1/2}$, and broadenings, $\Gamma_{LS1/2}$, can be found in Table D.1. We find that our simplified model can qualitatively describe the experimental measurement and capture the broadenings.

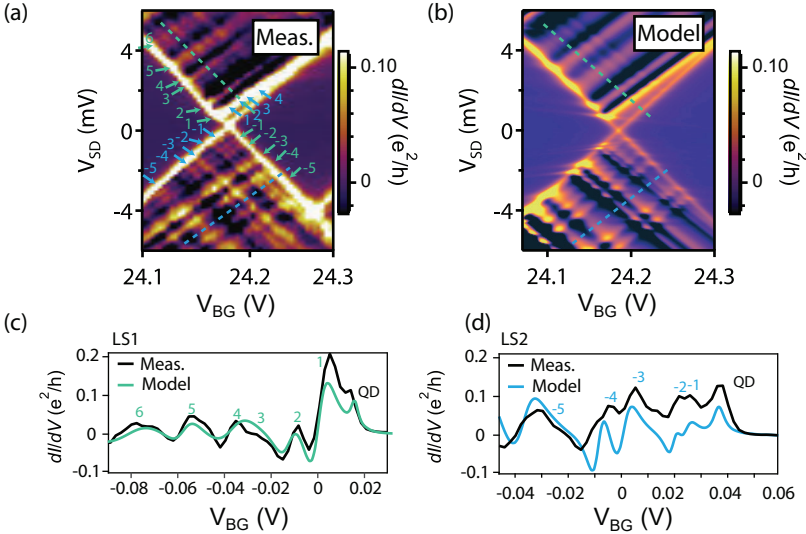


Figure 7.8. Device A Model: (a) Coulomb blockade diamond measurement and (b) results of model calculations with adjustable parameters given Appendix D. The numbers denote the resonance number, n , for $LS1$ (green) and $LS2$ (blue). (c) Line cut along the green dashed line in (a) for the measurement (black) and (b) for the model (green). (d) Line cut along the dashed blue line in (a) for the measurement (black) and in (b) for the model (blue). We find that we are able to reproduce the positions and widths, but not the amplitudes, of the resonances.

To find each resonances appropriate broadening, Γ_{LS1}^n and Γ_{LS2}^n , we take

a line cut along the green(blue) dashed line. Figure 7.8 shows dI/dV as a function of V_{BG} along the dashed (c) green and (d) blue line in (a) and (b). This represents the local DOS of (c) $LS1$ or (d) $LS2$ where the peaks in dI/dV correspond to peaks in the local DOS. By adjusting $\Gamma_{LS1/2}^n$ and their amplitudes for each resonance, we fit the peaks in the model to the data. In (c), we find that Γ_{LS1} in the model takes values between 0.15 meV to 1.3 meV to accurately capture the broadening of the peaks, as well as the NDC found in the measurement. Similar for (d), we find Γ_{LS2} varies between 0.2 meV to 0.4 meV.

Figure 7.9(a) shows the dependence of δE_{LS1} and δE_{LS2} on n . We find that δE_{LS1} and δE_{LS2} have similar values that vary between 0.2 meV and 1.3 meV over the 20 LSs. Similarly, Fig. 7.9(b) shows the dependence of Γ_{LS1} and Γ_{LS2} on n . We find Γ_{LS1} and Γ_{LS2} are roughly constant with $\Gamma_{LS1} \approx \Gamma_{LS2} \approx 0.3$ meV for the LSs probed by this QD resonance. In both cases, we do not observe a systematic trend or dependence on n . We speculate that this is due to the QD probing only a local DOS of $LS1$ and $LS2$, where large changes in $\delta E_{LS1/2}$ and $\Gamma_{LS1/2}$ are not expected. Further analysis as a function of V_{BG} would be interesting to see how the values change over a large change in the electrochemical potential of the leads.

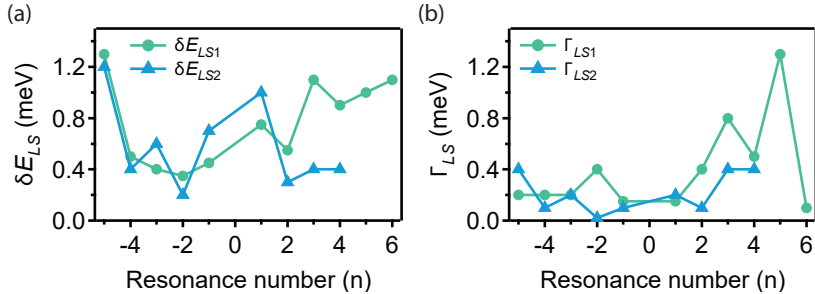


Figure 7.9. Single particle level spacing and broadening in device **A:** (a) Lead state level spacing, δE_{LS} , as a function of resonance number, n for lead states (LSs) in $LS1$ (green) and $LS2$ (blue). We find that δE_{LS1} and δE_{LS2} remains roughly constant for increasing n . (b) Lead state level broadening, Γ_{LS} , as a function of resonance number, n for LSs in $LS1$ (green) and $LS2$ (blue). Similar to (a), Γ_{LS2} remains roughly constant for increasing n . All of the values for δE_{LS2} and Γ_{LS2} were extracted from Fig. 7.8(b).

Device B

Fig. 7.10 shows the (a) measured and (b) modeled Coulomb blockade diamond for the lever arms given in Table 7.4. We find that the model Coulomb blockade diamond is in good agreement with the measured diamond. From (a), we find that $\delta E_{LS1}^1 = 3.1 \text{ meV}$ and $\delta E_{LS2} = 0.6 \text{ meV}$ to 1 meV . However, the broadening of the resonances could not be extracted in a similar fashion as in device A due to the low resolution of the measurement.

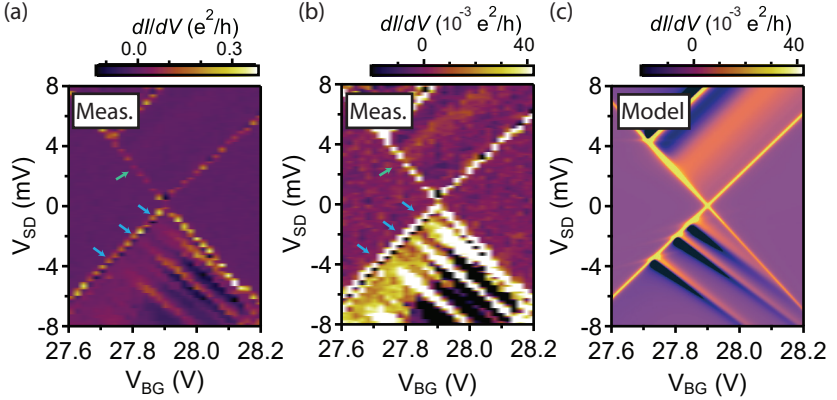


Figure 7.10. Device B Model: (a) Measured and (c) modeled Coulomb blockade diamond measurement showing one lead resonance corresponding to $LS1$ (green) and four lead resonances corresponding to $LS2$ (blue). (b) The same measurement as (a), but with adjusted contrast. We find that the lead resonance corresponding to $LS1$ is very broad and its slope is parallel to the diamond edge, suggesting that the Se dopants increase the carrier concentration enough to strongly couple the lead states to the source reservoir.

Nevertheless, we estimate $\Gamma_{LS1} \approx 3 \pm 0.5 \text{ meV}$ from the plot. This results in $\Gamma_{LS1} \approx \delta E_{LS1}$, consistent with stronger coupling due to the doping. However, for $LS2$, we estimate $\Gamma_{LS2} = 0.2 \text{ meV}$ to 0.4 meV . Therefore, $\Gamma_{LS2} < \delta E_{LS2}$ and the local DOS of $LS2$ is strongly modulated, similar to device A. Thus, we speculate that this discrepancy between the two lead segments is likely due from the Se dopants present in the lead segment of $LS1$ that broaden the lead states compared to the undoped lead segment of $LS2$.

7.5. Conclusion

In this chapter, we demonstrated that the in situ grown QD in InAs/InP heterostructure NWs can be used as a tunnel spectrometer to probe the local density of states in the NW lead segments. The non-constant local density of states appear as resonances in Coulomb blockade diamond measurements that cannot be attributed to effects of the QD itself. These features could be modeled using a capacitance model neglecting interdot couplings. Using this simplified model, we could extract the lever arms between the lead segments and the reservoirs, as well as the broadening of the bound states in the leads. We find that the local DOS is heavily modulated, as expected from Chapter 6.

We find that in device A, both of the lead segments are equally weakly coupled to their reservoirs, resulting in their resonances having slopes that are shallower than the QD diamond edge and narrow broadenings. The weak coupling likely arises from the low carrier concentration in wurtzite InAs. In device B, we investigated how the capacitive coupling differs between a reservoir contacted to Se-doped InAs and undoped InAs. We find that chemical doping results in strong coupling between the lead segment and the reservoir, leading to lead resonances that are parallel to the QD diamond edge, as well as a large broadening of the LSs. In contrast, the coupling between the undoped InAs lead segment and its reservoir had weaker coupling, similar to device A, that results in lead resonances with a shallower slope than the QD diamond edge. In device C, we find that the slopes of the lead states can be described by weak coupling between $LS2$ and the drain reservoir. However, the influence of V_{SG} on their slopes could not be deduced. In addition, we find hybridization effects between LSs and QD states.

Further investigation of the LS could be performed in the next generation of experiments with these InAs/InP heterostructure NWs. Nevertheless, this information is valuable for further spectroscopy studies of how the quasi zero dimensionality of the lead segments affects transport studies in hybrid nanowire systems [42, 50, 249].

8 Spectroscopy of the superconducting proximity effect

In this chapter, we use an InAs/InP heterostructure NW with one superconducting contact. This gives rise to new types of lead states due to the coupling to the proximity induced superconducting NW lead segment (LS) adjacent to the superconducting contact. Following a similar methodology to experiments done on crystal-phase InAs NWs [50], we demonstrate that the integrated QD can be used as a spectrometer to probe the quasiparticle density of states (DOS) and sub-gap states in the LS. We show the results of two transport regimes of the QD used to extract the proximity induced superconducting gap size, Δ^* : the cotunneling regime and the sequential tunneling regime. Figure 8.1 illustrates the transport processes in each regime. In (a) the sequential tunneling regime, the QD acts as an energy filter coupling to LSs only at the energies of QD resonances, while in (b) the cotunneling regime, the QD can be thought of as a tunable tunnel barrier.

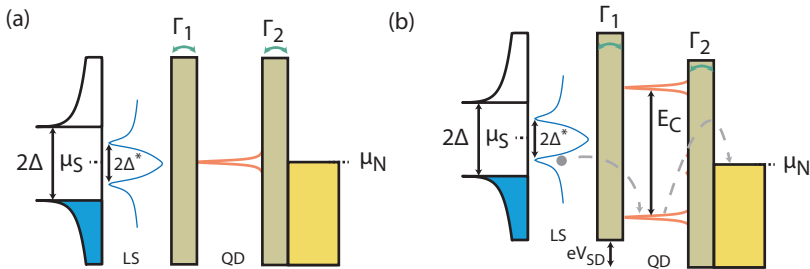


Figure 8.1. Sequential and cotunneling regime: Schematic of the electrochemical potentials for a proximitized nanowire lead segment (LS). The quantum dot (QD) acts as a tunnel probe for the quasiparticle density of states of the lead segments. Transport via the (a) sequential tunneling regime and (b) the cotunneling regime is shown. Adapted from [50].

We assume most of the voltage across the NW drops over the QD, therefore the differential conductance is proportional to the DOS and we can describe the system with a resonant tunneling model. If electrons would tunnel directly

from the superconducting contact onto the QD, we would expect to see a BCS-like gap with a sharp ideal BCS DOS and a gap size similar to the bulk value (here: aluminum $\Delta \approx 210 \mu\text{eV}$) [250]. In this chapter, we investigate whether the DOS of the LS becomes more BCS-like for large tunnel barrier height in InAs/InP heterostructure NWs compared to crystal-phase InAs NWs [50].

8.1. Device and characterization

In Fig. 8.2 (a) a schematic of the device along with (b) a false colored scanning electron microscope image of an InAs/InP NW superconducting hybrid device is shown. The NW is contacted by one superconducting (SC) Ti/Al contact (blue) and one normal (N) Ti/Au contact (yellow). The deterministic properties of the integrated QD, defined by the in situ grown InP segments (red), allows us to separate the NW into two lead segments: $LS1$ and $LS2$. $LS1$ and $LS2$ have lengths of $L_1 = 50 \text{ nm}$ and $L_2 = 350 \text{ nm}$, respectively. A side gate (SG) of width 100 nm is positioned 50 nm away from the NW between the normal metal contact and the QD. Further fabrication details can be found in Chapter 4.

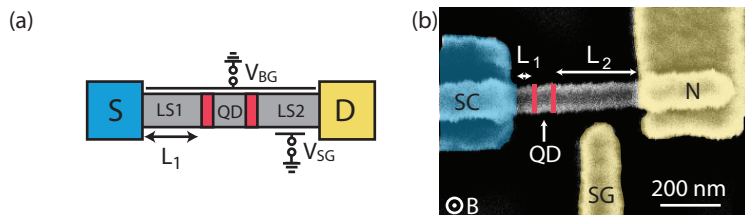


Figure 8.2. Device and setup: (a) Schematic and (b) false color scanning electron microscopy image of an InAs/InP heterostructure nanowire device. The NW is electrically contacted to a superconductor (SC) consisting of titanium/aluminum (blue) electrode and to a normal (N) metal electrode consisting of titanium/gold (yellow). A quantum dot (QD) is formed within the bare InAs segment between two in-situ grown InP segments (red). The distance between the superconducting contact and the QD is $L_1 = 50 \text{ nm}$ and $L_2 = 350 \text{ nm}$ is the distance between the QD and normal metal contact. The chemical potential of the entire NW is tuned with a global back gate V_{BG} , while the electrochemical potential of the QD and in the lead region near the normal contact is tuned by side gate voltage, V_{SG} .

The chemical potential in both the lead segments and the NW is tuned by a back gate voltage, V_{BG} , while the electrochemical potential of the QD and in the lead region near the normal contact is tuned by side gate voltage, V_{SG} . A

perpendicular magnetic field, B , was used to suppress the superconductivity of aluminum. The device was measured in a dilution refrigerator with a base temperature of 20 mK. An AC and DC voltage was applied to the SC contact, V_{SD} , while the N contact was kept grounded and used for the current (I) measurement. The differential conductance, $dI/dV_{SD} = I_{AC}/V_{AC}$, was measured using standard lock-in techniques.

We first show that the integrated QD and LSs in the normal state in this device exhibits similar properties to the one discussed in Chapter 6. Figure 8.3 shows dI/dV as a function of source-drain voltage, V_{SD} , and (a) V_{BG} or (b) V_{SG} , in the superconducting state ($B = 0$). In (a), $V_{SG} = 0$ and for (b), $V_{BG} = 22$ V. In both measurements, we observe very regular and reproducible Coulomb blockade (CB) diamonds over several volts. In the gate range shown in Fig. 8.3(a) and (b), we estimate the electron population on the QD to be ~ 50 .

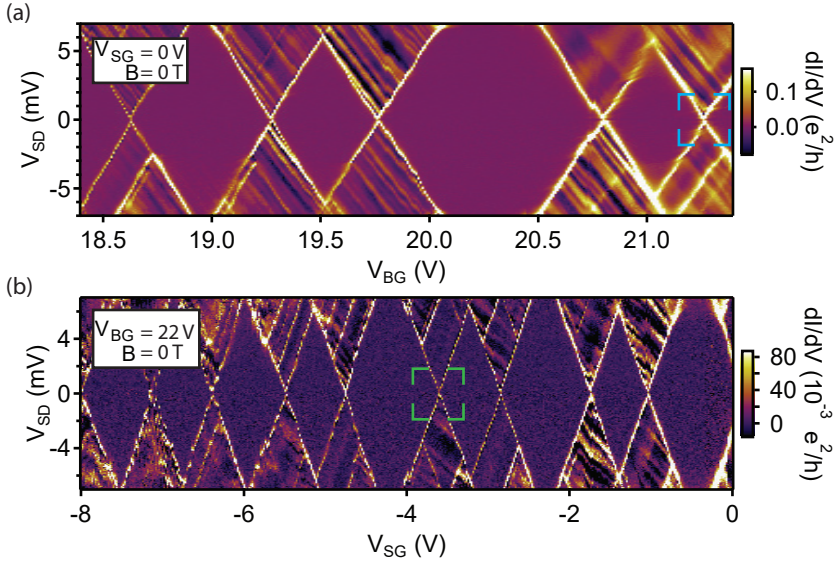


Figure 8.3. Coulomb blockade diamonds: Differential conductance, dI/dV , as a function of source-drain voltage, V_{SD} and either back gate voltage (a), V_{BG} or side gate voltage (b), V_{SG} . In (a), $V_{SG} = 0$, while for (b) $V_{BG} = 22$ V. Regular Coulomb blockade diamonds are observed over a large gate range. Further analysis were performed on the resonances indicated by the dashed blue and green regions.

The QD is characterized by the addition energy, E_{add} , charging energy, E_C , and single particle level spacing, δE , total tunnel coupling, Γ , and asymmetry $A = \Gamma_1/\Gamma_2$, where Γ_1 and Γ_2 are the individual tunnel couplings. A region of the CB diamonds exhibits a clear even-odd pattern from which we can determine the characteristic QD energy scales [102]. From the even/odd pattern of the first two diamonds in Fig. 8.3(a), we extract $E_{\text{add}} = 8$ meV and $E_C = 6$ meV. This results in $\delta E = 2$ meV which is consistent with the corresponding excited state resonances outside the CB diamonds. For the resonances indicated by the blue and green dashed box, Γ and A were determined by fitting the line shape of the CB resonance in the normal state ($B = 100$ mT) with Eq. 6.2 with the electron temperature fixed to $T = 50$ mK.¹ For the resonance indicated by the blue dashed box in (a), we find $\Gamma \approx 140$ μeV with asymmetry $A \approx 23$. Similarly, for the resonance indicated by the green dashed box in (b), we find $\Gamma = 48$ μeV and $A = 23$. In addition, we observe several lead resonances that arise from the modulated DOS of the InAs lead segments, similar to the measurements in Chapter 6. We refer back to Chapter 7 for further discussion on lead resonances. Now, we will look into the probing the superconducting proximity gap in the lead region.

8.2. Sequential tunneling regime

The first transport regime we investigate is the sequential tunneling regime, as shown in Fig. 8.1(a). To describe the system, we assume that the QD is weakly coupled to the superconductor and strongly coupled to the normal metal, i.e. $\Gamma_S \ll \Gamma_N \ll \Delta \ll \delta E \ll E_C$. The normal lead is assumed to have a constant DOS, while the superconducting contact has a BCS DOS. The electron wavefunctions within the superconductor is extended into the NW lead segment via Andreev reflection. This causes the lead segment to become proximitized and exhibit superconducting properties [251, 252]. However, the DOS of the superconducting lead segment is unknown, but we characterize it by the proximity induced superconducting gap, Δ^* and suppression factor, $S = G_S/G_N$. Here, G_S and G_N is the differential conductance in the gap and outside of the gap, respectively.

Figure 8.4(a) shows the expected effects on the single electron transport for an N-QD-S device in the sequential tunneling regime. Here, we plot dI/dV as a function of V_{SD} and gate voltage V_G . We observe two clear effects, each marking the onset of quasiparticle transport: a shift in bias and gate voltage of the Coulomb blockade diamond "tips" by $\Delta V_{\text{SD}} = 2\Delta^*/e$ and $\Delta V_G = \frac{2\Delta^*}{e|\beta_-|}$, respectively. Here, we assume the bias is applied to the superconductor, therefore β_- is the negative slope of the CB diamond. The purple panel indicates the effect of a finite DOS within the superconducting gap ($eV_{\text{SD}} < |\Delta^*|$). Since

¹See Chapter 6 for more information on Coulomb blockade resonance line shape analysis.

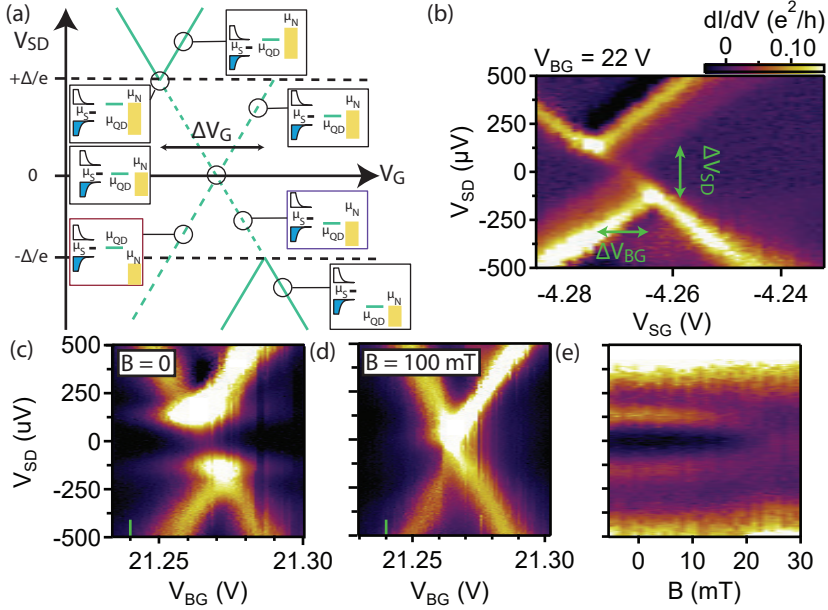


Figure 8.4. Proximity gap in the sequential tunneling regime: illustration of the expected (a) and measured (b) Coulomb blockade diamonds in a S-QD-N device. (a) A diagram of the alignment of all the involved electrochemical potentials in relation to the CB diamond are shown where the normal metal (gold) and a superconductor (blue) coupled to a QD. (b) Differential conductance as a function of source-drain voltage bias V_{SD} and gate voltage V_{SG} for back gate voltage $V_{BG} = 22$ V. Transport is blocked within the superconducting gap $\pm\Delta$, indicated by the dashed line, and the Coulomb diamond tips are shifted in gate voltage by $\Delta V_G = \frac{2\Delta}{e\beta_-}$. (c-e) Another CB diamond in the (c) superconducting state ($B = 0$) and (d) normal state $B = 100$ mT. (e) Magnetic field dependence of the superconducting gap. Schematic adopted from Ref. [103].

the DOS is nonzero, transport can still be mediated by quasiparticles within the gap.

We now focus on the two CB diamonds in Fig 8.3(a) and (b) indicated by a blue and green box, starting with the resonance indicated by the green marked region. In Fig. 8.4(b), we plot dI/dV as a function of V_{SD} and V_{SG} for $V_{BG} = 22$ V and $B = 0$. As expected from (a), we find that the CB diamond tips are shifted in V_{SD} and V_{SG} . From the shift in V_{SD} , we extract $\Delta^* \approx$

125 μeV . The CB diamond tips are shifted in gate voltage by $\Delta V_{SG} = 0.01$ V. Using $|\beta_-| = 0.02$ from the negative slope of the diamond edge, we extract $\Delta^* \approx 115$ μeV , in agreement with the shift in V_{SD} . $S \approx 0.4$ was determined by dI/dV inside and outside of the gap along the CB diamond edge. As stated earlier, $\Gamma = 48$ μeV for this resonance, therefore, the proximity induced gap larger than the broadening of the energy level, i.e. $\Gamma < \Delta^*$.

Now, we look into the magnetic field dependence of Δ^* and focus on the resonance indicated by the blue marked region in Fig. 8.3(a). Figure 8.4 shows dI/dV as a function of V_{SD} and V_{BG} for $V_{SG} = 0$ in (c) the superconducting state ($B = 0$) and (d) normal state ($B = 100$ mT). In the superconducting state, we find $\Delta^* \approx 125$ μeV and $S \approx 0.5$. Now, we observe a gap size similar to the broadening of the energy level, i.e. $\Delta^* \approx \Gamma$. In the normal state, the superconducting properties are suppressed and the system acts a typical QD coupled to two normal metals. In Fig. 8.4(e), we show the evolution of Δ^* as a function of B at $V_{BG} = 21.24$ V (green line in Fig. 8.4(a) and (b)). We find that the gap closes at 25 mT.

To extract the characteristic values of this system, we implement a resonant tunneling model for an S-QD-N system. We use a simple resonant tunneling model to approximate the current as [193, 253]:

$$I = \frac{e}{h} \int D_N(E) D_S(E + eV_{SD}) \cdot T_{\text{QD}}(E, V_{BG}, V_{SD}) \cdot [f_N(E) - f_S(E + V_{SD})] dE, \quad (8.1)$$

where $D_N(E)$ is the constant DOS of the normal lead. The DOS of the superconducting lead is given by Eq. 2.15. The transmission through the QD, $T_{\text{QD}}(E, V_{BG}, V_{SD})$, takes the form of a Breit-Wigner function and accounts for resonant tunneling through the QD which we assume to be independent of the lead DOS. The Fermi distribution of the contacts are taken into account in $f_{S/N}$. To reproduce the suppression observed experimentally, Eq. 2.15 can be modified by introducing the phenomenological Dynes parameter δ [254]. The DOS of the lead segment is then given by $D_S(E) = \left| \Re \left(E - i\delta / \sqrt{(E - i\delta)^2 - (\Delta^*)^2} \right) \right|$.

By fixing the the QD parameters and Δ^* to the values determined previously, we get conductance maps as shown in Fig. 8.5(a)-(b) (model). To quantitatively compare the measurement to the model, we take a line cut along the QD diamond edge indicated by the arrows. In (a), we set $\Delta^* = 125$ μeV , $\Gamma_1 = 46$ μeV , and $\Gamma_2 = 2$ μeV . We find that we can reproduce the characteristics of the CB diamond and $S \approx 0.4$ with $\delta = 0.15$. Similarly for (b), we set $\Delta^* = 125$ μeV , $\Gamma_1 = 133$ μeV , and $\Gamma_2 = 19$ μeV , and find $\delta = 0.15$ results in $S \approx 0.5$, similar to that observed in the experiment. We note that Γ_2 extracted from the Coulomb resonance in the normal state is $\Gamma_2 = 7$ μeV , leading to a change in A from 23 to 7. We found no value of δ with $A = 23$ that could

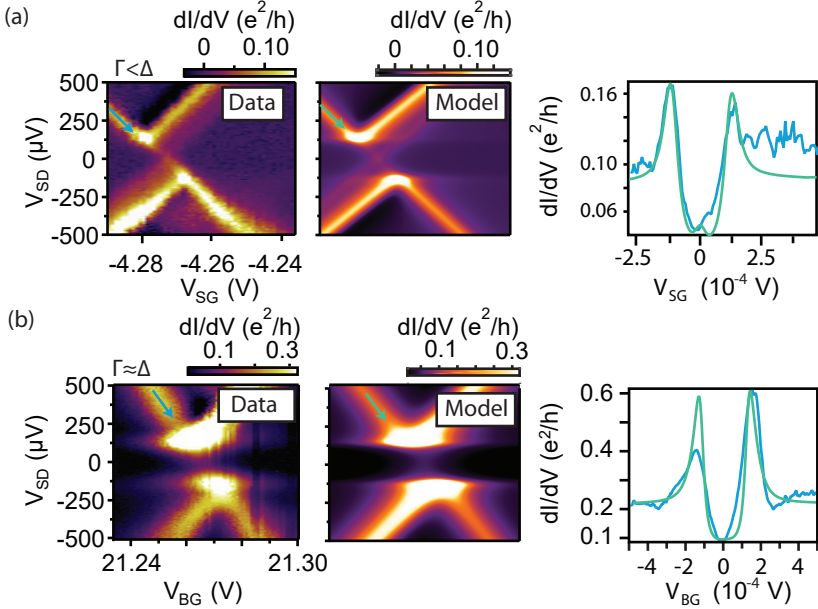


Figure 8.5. Modeling of the proximity gap in the sequential tunneling regime: (a)-(b) Comparison of the measurement to the resonant tunneling model. To qualitatively compare the model to the measurement, we compare dI/dV as a function of gate voltage along the Coulomb blockade diamond edge. From the Coulomb blockade diamond measurement, we extract $\Delta^* = 125 \mu\text{eV}$, $\Gamma_1 = 46 \mu\text{eV}$, and $\Gamma_2 = 2 \mu\text{eV}$. Using a Dyne's parameter, $\delta = 0.15$, reproduces the features of the CB diamond measurement and the suppression, $S \approx 0.4$, observed in the experiment. Similarly in (b), we extract $\Delta^* = 125 \mu\text{eV}$, $\Gamma_1 = 133 \mu\text{eV}$, and $\Gamma_2 = 19 \mu\text{eV}$ and find $\delta = 0.15$ results in $S \approx 0.4$ observed in the experiment.

reproduce the suppression observed in the measurement. We speculate that this is a result of lead states being present in the region between the QD and the normal metal that is not taken into account in the model.

In both cases, we observe a proximity induced gap in the NW lead segment smaller than Δ . This can be understood by considering Andreev bound states (ABSs) forming in the lead with energy, E_{ABS} , in either the long or short junction limit. In the long junction limit, the length of the proximitized lead segment, L , is longer than the characteristic coherence length of the superconductor in the ballistic limit, i.e. $L > L_C = \hbar v_F / \Delta^*$, where v_F is the Fermi

velocity in the NW lead segment [255]. In this limit, E_{ABS} is determined by the phase picked up in the lead segment which scales with v_{F} and can take smaller values, thus filling the gap with ABSs which mimicks a closing of the gap when observed in transport experiments [50, 255]. As a result, Δ^* is reduced by ABSs moving into the gap. In the short junction limit, $L \ll L_{\text{C}}$, the energies of the ABSs are pushed to the gap edge, $E_{\text{ABS}} \approx \Delta$, resulting in the superconducting proximity gap similar to Δ , i.e. $\Delta^* \approx \Delta$.

In our case, we have a proximitized region of length $L = L_1 = 50 \text{ nm}$. If the system would be in the long junction limit, then $v_{\text{F}} < 1 \times 10^4 \text{ m s}^{-1}$ is required for $L_1 > L_{\text{C}}$. We estimate $v_{\text{F}} = \sqrt{\frac{2\phi}{m^*}}$, where $\phi = e\alpha_{\text{LS}}(V_{\text{BG}} - V_{\text{P}})$ is the difference between E_{F} and E_{CBE} with the gate lever arm of the lead segment, α_{LS} , and the pinchoff voltage, V_{P} , and $m^* = 0.04m_{\text{e}}$ is the effective mass of wurtzite InAs. From Chapter 7, we estimate $\alpha_{\text{LS}} \approx 0.005$. The exact value of V_{P} is not known for this device, however we estimate it to be $V_{\text{P}} \approx 5 \text{ V}$ by the onset of CB resonances at $V_{\text{SD}} = 0$. For $V_{\text{BG}} = 21 \text{ V}$, we find $v_{\text{F}} \approx 5 \times 10^5 \text{ m s}^{-1}$. Therefore, we find that the system is in the short junction with values similar with the work done in crystal-phase defined QDs even though E_{F} is positioned closer to E_{CBE} in our case [50].

8.3. Cotunneling regime

Now, we investigate is the cotunneling regime, as shown in Fig. 8.1(b). In the cotunneling regime, the QD is in Coulomb blockade and transport is mediated via higher order elastic tunneling processes often referred to as elastic cotunneling where an electron can tunnel off of the QD if another electron tunnels onto the QD within a time window $\sim h/E_{\text{C}}$ given by Heisenberg's uncertainty principle. For $E_{\text{CBE}} \approx E_{\text{F}}$, the effective tunnel barrier is large and higher order tunneling processes are suppressed.

Cotunneling lines are expected to form around the gap edge, $V_{\text{SD}} = \pm\Delta^*$, which mark the onset of quasiparticle transport. Figure 8.6 shows the cotunneling regime for large V_{BG} . The dashed lines indicated where the cotunneling lines are expected to form, i.e. at $V_{\text{SD}} = \pm 125 \mu\text{V}$. We observe no clear evidence of cotunneling in our measurements. We attribute this to the large tunnel barrier height, $V_0 = 350 \pm 50 \text{ meV}$, in InAs/InP heterostructure NWs. Compared to crystal-phase QDs, V_0 is ~ 3.5 times larger [48, 50], which makes it difficult to tune E_{CBE} such that $E_{\text{CBE}} \ll E_{\text{F}}$ due the the small gate lever arm, $\alpha = 0.01$, for this device. We observed no evidence of cotunneling up to $V_{\text{BG}} = 40 \text{ V}$.

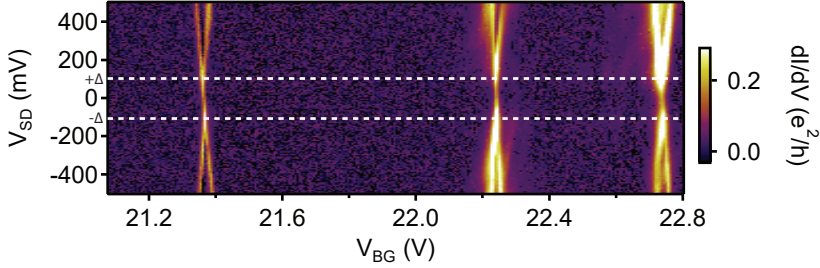


Figure 8.6. Cotunneling regime: Differential conductance, dI/dV , as a function of source-drain bias, V_{SD} , and back gate voltage, V_{BG} . In the cotunneling regime, no proximity induced gap is observed. The dashed white line marks $\pm\Delta^* \approx 125 \mu\text{eV}$ extracted in the sequential tunneling regime.

8.4. Summary and discussion

In this chapter, we presented a systematic study of proximity induced superconductivity in a nanowire lead segment. We implemented an integrated InAs/InP heterostructure QD as a tunnel probe for a proximity induced superconducting nanowire lead segment by investigating the sequential and cotunneling regime. In the sequential tunneling regime, we observed a clear shift of the CB diamond tips as a function of bias and gate voltage, characteristic of one nanowire lead exhibiting proximity induced superconductivity. From the CB diamonds, we extract $\Delta^* \approx 125 \mu\text{eV}$, consistent with an S-N system in the short junction limit. This provides further evidence that proximity induced gap values are heavily modified from their corresponding bulk values, i.e. $\Delta^* < \Delta$, when coupled to a finite nanowire lead segment. The characteristics of the CB diamonds and suppression could be replicated with a resonant tunneling model of a QD coupled to a "soft" superconductor with $\delta = 0.15$. In the cotunneling regime, we observed no evidence of transport via cotunneling processes at the gap edge. This could be understood by the large tunnel barrier height in InAs/InP heterostructure NWs making it difficult to allow higher order tunneling processes energetically favorable. In contrast to crystal-phase InAs NW QDs, we observed no evidence of ABSs forming in the LS [50, 51]. However, this is not a consequence of the larger tunnel barriers, but rather the weaker coupling to the superconductor. In InAs/InP heterostructure NWs, the superconductor is contacted to wurtzite InAs which intrinsically has a lower electron density than zinc-blende InAs in crystal-phase InAs NWs. Therefore stronger coupling to the superconductor in crystal-phase InAs NWs is expected. Efforts have been made to strengthen the coupling to the super-

conductor by increasing the carrier concentration in InAs/InP heterostructure NWs by intrinsically doping one wurtzite InAs lead segment with selenium atoms during growth [248], however no clear evidence of proximity induced superconductivity was observed. The measurements presented in this chapter provide further support that integrated InAs/InP heterostructure QDs can be used as a novel spectroscopic tool to probe topological bound states in superconducting hybrid systems [57, 59, 121, 249, 256, 257].

9 Summary and Outlook

In this thesis, we successfully demonstrated that in situ grown InP segments in InAs nanowires form large deterministic tunnel barriers that can be used for systematic tunnel spectroscopy experiments. We found that the deterministic nature of the tunnel barriers allows us to divide the device into well understood sub-systems and that the integrated quantum dot acts as a high resolution tunnel spectrometer that can be used to probe the fine structure of the density of states (DOS) in the leads.

We began with investigating electrostatic gate-defined tunnel barriers in **Chapter 5**. In this system, we implemented a grid of bottom gates that were used to electrostatically gate specific regions along an InAs nanowire and a carbon nanotube to study the physics of single and double quantum dots. We showed that electrostatic gates can be used to form single and double quantum dots in these quasi one-dimensional semiconductors. However, we observed that the electrostatic gates only weakly confine the quantum dots and therefore are spatially ill-defined with broad line widths and exhibit uncontrolled barrier characteristics. These ill-defined tunnel barrier characteristics likely stem from their unknown geometries, interactions between the gate and the charge carriers in the system, and being susceptible to charge noise from the environment. These observations make it challenging to use electrostatic gates as a building block for tunnel spectroscopy measurements.

An alternative method to form deterministic tunnel barriers was taken in **Chapter 6**. Here, we investigated the properties of in-situ grown InP tunnel barriers in an InAs nanowire. We showed that the in situ grown InP segments strongly confine the region between them, resulting in highly predictable and perfectly symmetric QDs with level broadenings small enough for high resolution spectroscopy measurements. We observed a continuous transition of the Coulomb blockade line shapes from the lifetime to the thermally broadened regime. This showcases that the linewidth of the tunnel probe is not limited by weak confinement, but rather by the electronic temperature of the system. In addition, we observed a systematic increase in the tunnel coupling from which we extracted a conduction band edge offset between InAs and InP of 350 ± 50 meV, in agreement with theoretical calculations. Thus showing the InP tunnel barriers behave as the large deterministic tunnel barriers we aimed to achieve in this thesis.

Furthermore, we demonstrated two experiments where we used the integrated QD to investigate the DOS in the nanowire when coupled to normal metal (**Chapter 7**) and superconducting (**Chapter 8**) reservoirs. In **Chapter 7**, we showed that the QD exhibits high enough resolution to resolve the fine structure of the local DOS in the leads. From Coulomb blockade diamond measurements, we observed several additional features that cannot be attributed to the QD and demonstrated that these additional features originate from a modulated DOS of the NW leads. From the slopes of the lead states, we quantified the coupling between the lead and its respective reservoir. We found that by implementing a three site resonant tunneling model, we could analytically extract the broadening of the lead states. By comparing their broadenings to their level spacings, we could deduce that the local DOS in the leads is strongly modulated, providing further support to the analysis presented in Chapter 6. In addition, we compared the coupling for a typical InAs/InP heterostructure NW and a InAs/InP heterostructure NW with one lead containing selenium dopants to increase the carrier concentration. We found that the increase in carrier concentration results in stronger coupling between the lead and reservoir, which, in turn, broadens the widths of the lead states. Furthermore, we found evidence of hybridization between the QD and the LSs, as well as clear affects due to electrostatic gating of LSs, that requires further investigation. This type of systematic study has yet been shown, however this paves the way to further understanding the entire NW system and not just the QD.

In **Chapter 8**, we used the integrated QD as a tunnel probe for a superconducting proximitized lead region by coupling the QD to one superconducting contact and showed that these types of integrated QDs are excellent tools to probe subgap features. In the resonant tunneling regime, we could clearly resolve a superconducting proximity gap that arises when the bulk superconductor proximitizes the NW lead region. We extracted a proximity gap less its bulk value, providing further evidence that the proximitized gap is heavily modified from its corresponding bulk value, likely due to many overlapping Andreev bound states in short junction regime. The proximity gap was also studied in the cotunneling regime, however we found that the strong confinement from the in situ grown tunnel barriers makes studies in the cotunneling regime difficult.

In summary, we have successfully established a new platform where in-situ grown InP segments in InAs NWs form highly deterministic tunnel barriers. Throughout this thesis, we have shown their remarkable textbook-like properties and a potential platform for next generation nanowire devices for studying tunnel probe experiments, as well as fundamental QD physics. This thesis laid the ground work for future tunnel spectroscopy measurements in one-dimensional wires to probe exotic states of matter such as Majorana bound states, as well as play a crucial role in spin-readout in topological scaleable

qubit architectures.

Future experiments

Several interesting experiments could be immediately realized by combining the two systems studied in this thesis: electrostatic bottom gates and an InAs/InP heterostructure nanowire. In this setup, independent control over the QD, leads, and the doping beneath the reservoirs could be achieved. In this next generation of devices, a more thorough and systematic study of the normal or superconducting state lead DOSs could be performed. For example, by keeping the QD charge state fixed, thus a constant tunnel probe, and investigating the evolution from single to many mode transport by independent electrostatic gating of the lead regions and/or the doping beneath the superconducting reservoir. This experiment would lead to a better understanding of how the modes in the leads contribute to transport processes and would be one step towards unambiguously differentiating trivial Andreev bound states from topological states formed in a proximitized nanowire region.

Bibliography

- [1] A. Stern and N. H. Lindner, *Science* **339**, 1179 (2013).
- [2] C. Nayak, S. H. Simon, A. Stern, M. Freedman, and S. D. Sarma, *Reviews of Modern Physics* **80**, 1083 (2008).
- [3] J. Alicea, *Physical Review B* **81** (2010), 10.1103/physrevb.81.125318.
- [4] Y. Oreg, G. Refael, and F. von Oppen, *Physical Review Letters* **105** (2010), 10.1103/physrevlett.105.177002.
- [5] J. Alicea, Y. Oreg, G. Refael, F. von Oppen, and M. P. A. Fisher, *Nature Physics* **7**, 412 (2011).
- [6] M. T. Deng, S. Vaitiekėnas, E. B. Hansen, J. Danon, M. Leijnse, K. Flensberg, J. Nygård, P. Krogstrup, and C. M. Marcus, *Science* **354**, 1557 (2016).
- [7] V. Mourik, K. Zuo, S. M. Frolov, S. R. Plissard, E. P. A. M. Bakkers, and L. P. Kouwenhoven, *Science* **336**, 1003 (2012).
- [8] S. D. Sarma, M. Freedman, and C. Nayak, *npj Quantum Information* **1** (2015), 10.1038/npjqi.2015.1.
- [9] D. Aasen, M. Hell, R. V. Mishmash, A. Higginbotham, J. Danon, M. Leijnse, T. S. Jespersen, J. A. Folk, C. M. Marcus, K. Flensberg, and J. Alicea, *Physical Review X* **6** (2016), 10.1103/physrevx.6.031016.
- [10] J. Klinovaja and D. Loss, *Physical Review B* **90** (2014), 10.1103/physrevb.90.045118.
- [11] E. Gaidamauskas, J. Paaske, and K. Flensberg, *Physical Review Letters* **112** (2014), 10.1103/physrevlett.112.126402.
- [12] A. Keselman, L. Fu, A. Stern, and E. Berg, *Physical Review Letters* **111** (2013), 10.1103/physrevlett.111.116402.
- [13] L.-A. Wu and D. A. Lidar, *Journal of Mathematical Physics* **43**, 4506 (2002).
- [14] S. J. Tans, M. H. Devoret, H. Dai, A. Thess, R. E. Smalley, L. J. Geerligs, and C. Dekker, *Nature* **386**, 474 (1997).
- [15] S. Reich, C. Thomsen, and P. Ordejón, *Physical Review B* **65** (2002), 10.1103/physrevb.65.155411.
- [16] G. Abulizi, A. Baumgartner, and C. Schönenberger, *physica status solidi (b)* **253**, 2428 (2016).

- [17] J.-D. Pillet, C. H. L. Quay, P. Morfin, C. Bena, A. L. Yeyati, and P. Joyez, *Nature Physics* **6**, 965 (2010).
- [18] M. Jung, J. Schindele, S. Nau, M. Weiss, A. Baumgartner, and C. Schönenberger, *Nano Letters* **13**, 4522 (2013).
- [19] P. Jarillo-Herrero, S. Sapmaz, C. Dekker, L. P. Kouwenhoven, and H. S. J. van der Zant, *Nature* **429**, 389 (2004).
- [20] E. A. Laird, F. Pei, and L. P. Kouwenhoven, *Nature Nanotechnology* **8**, 565 (2013).
- [21] M. R. Gräber, M. Weiss, and C. Schönenberger, *Semiconductor Science and Technology* **21**, S64 (2006).
- [22] J. Nygård, D. H. Cobden, and P. E. Lindelof, *Nature* **408**, 342 (2000).
- [23] M. Mergenthaler, A. Nersisyan, A. Patterson, M. Esposito, A. Baumgartner, C. Schönenberger, G. A. D. Briggs, E. A. Laird, and P. J. Leek, arXiv e-prints, arXiv:1904.10132.
- [24] M. Marganska, L. Milz, W. Izumida, C. Strunk, and M. Grifoni, *Physical Review B* **97** (2018), 10.1103/physrevb.97.075141.
- [25] J. D. Sau and S. Tewari, *Physical Review B* **88** (2013), 10.1103/physrevb.88.054503.
- [26] J. Klinovaja, S. Gangadharaiah, and D. Loss, *Physical Review Letters* **108** (2012), 10.1103/physrevlett.108.196804.
- [27] S. Sapmaz, P. Jarillo-Herrero, L. P. Kouwenhoven, and H. S. J. van der Zant, *Semiconductor Science and Technology* **21**, S52 (2006).
- [28] A. Bachtold, C. Strunk, J.-P. Salvetat, J.-M. Bonard, L. Forró, T. Nussbaumer, and C. Schönenberger, *Nature* **397**, 673 (1999).
- [29] C. Schönenberger, *Semiconductor Science and Technology* **21**, S1 (2006).
- [30] A. Baumgartner, G. Abulizi, K. Watanabe, T. Taniguchi, J. Gramich, and C. Schönenberger, *Applied Physics Letters* **105**, 023111 (2014).
- [31] J. Gramich, A. Baumgartner, M. Muoth, C. Hierold, and C. Schönenberger, *physica status solidi (b)* **252**, 2496 (2015).
- [32] A. Cottet, T. Kontos, S. Sahoo, H. T. Man, M.-S. Choi, W. Belzig, C. Bruder, A. F. Morpurgo, and C. Schönenberger, *Semiconductor Science and Technology* **21**, S78 (2006).
- [33] M. R. Buitelaar, W. Belzig, T. Nussbaumer, B. Babić, C. Bruder, and C. Schönenberger, *Physical Review Letters* **91** (2003), 10.1103/physrevlett.91.057005.
- [34] M. Friedl, K. Cervený, P. Weigele, G. Tütüncüoğlu, S. Martí-Sánchez, C. Huang, T. Patlatiuk, H. Potts, Z. Sun, M. O. Hill, L. Güniat, W. Kim, M. Zamani, V. G. Dubrovskii, J. Arbiol, L. J. Lauhon, D. M. Zumbühl, and A. F. i Morral, *Nano Letters* **18**, 2666 (2018).

- [35] J. Gooth, M. Borg, H. Schmid, V. Schaller, S. Wirths, K. Moselund, M. Luisier, S. Karg, and H. Riel, *Nano Letters* **17**, 2596 (2017).
- [36] S. R. Plissard, I. van Weperen, D. Car, M. A. Verheijen, G. W. G. Immink, J. Kammhuber, L. J. Cornelissen, D. B. Szombati, A. Geresdi, S. M. Frolov, L. P. Kouwenhoven, and E. P. A. M. Bakkers, *Nature Nanotechnology* **8**, 859 (2013).
- [37] F. Krizek, T. Kanne, D. Razmadze, E. Johnson, J. Nygård, C. M. Marcus, and P. Krogstrup, *Nano Letters* **17**, 6090 (2017).
- [38] S. Gazibegovic, D. Car, H. Zhang, S. C. Balk, J. A. Logan, M. W. A. de Moor, M. C. Cassidy, R. Schmits, D. Xu, G. Wang, P. Krogstrup, R. L. M. O. het Veld, K. Zuo, Y. Vos, J. Shen, D. Bouman, B. Shojaei, D. Pennachio, J. S. Lee, P. J. van Veldhoven, S. Koelling, M. A. Verheijen, L. P. Kouwenhoven, C. J. Palmstrøm, and E. P. A. M. Bakkers, *Nature* **548**, 434 (2017).
- [39] P. Krogstrup, N. L. B. Ziino, W. Chang, S. M. Albrecht, M. H. Madsen, E. Johnson, J. Nygård, C. M. Marcus, and T. S. Jespersen, *Nature Materials* **14**, 400 (2015).
- [40] M. Bjergfelt, D. J. Carrad, T. Kanne, M. Aagesen, E. M. Fiordaliso, E. Johnson, B. Shojaei, C. J. Palmstrøm, P. Krogstrup, T. S. Jespersen, and J. Nygård, *Nanotechnology* **30**, 294005 (2019).
- [41] D. J. Carrad, M. Bjergfelt, T. Kanne, M. Aagesen, F. Krizek, E. M. Fiordaliso, E. Johnson, J. Nygård, and T. S. Jespersen, *Advanced Materials* , 1908411 (2020).
- [42] M.-T. Deng, S. Vaitiekėnas, E. Prada, P. San-Jose, J. Nygård, P. Krogstrup, R. Aguado, and C. M. Marcus, *Physical Review B* **98**, 085125 (2018).
- [43] S. Vaitiekėnas, M.-T. Deng, J. Nygård, P. Krogstrup, and C. Marcus, *Physical Review Letters* **121**, 037703 (2018).
- [44] A. Pfund, I. Shorubalko, R. Leturcq, and K. Ensslin, *Applied Physics Letters* **89**, 252106 (2006).
- [45] A. Pfund, I. Shorubalko, R. Leturcq, and K. Ensslin, *Physica E: Low-dimensional Systems and Nanostructures* **40**, 1279 (2008).
- [46] S. D'Hollosy, G. Fábíán, A. Baumgartner, J. Nygård, and C. Schönenberger, *AIP Conf. Proc.* , 359 (2013).
- [47] S. Baba, C. Jünger, S. Matsuo, A. Baumgartner, Y. Sato, H. Kamata, K. Li, S. Jeppesen, L. Samuelson, H. Q. Xu, C. Schönenberger, and S. Tarucha, *New Journal of Physics* **20**, 063021 (2018).
- [48] M. Nilsson, L. Namazi, S. Lehmann, M. Leijnse, K. A. Dick, and C. Thelander, *Physical Review B* **93**, 195422 (2016).
- [49] K. A. Dick, C. Thelander, L. Samuelson, and P. Caroff, *Nano Letters* **10**, 3494 (2010).

- [50] C. Jünger, A. Baumgartner, R. Delagrance, D. Chevallier, S. Lehmann, M. Nilsson, K. A. Dick, C. Thelander, and C. Schönenberger, *Communications Physics* **2** (2019), 10.1038/s42005-019-0162-4.
- [51] C. Jünger, R. Delagrance, D. Chevallier, S. Lehmann, K. A. Dick, C. Thelander, J. Klinovaja, D. Loss, A. Baumgartner, and C. Schönenberger, *Physical Review Letters* **125** (2020), 10.1103/physrevlett.125.017701.
- [52] X. Jiang, Q. Xiong, S. Nam, F. Qian, Y. Li, and C. M. Lieber, *Nano Letters* **7**, 3214 (2007).
- [53] M. Nilsson, L. Namazi, S. Lehmann, M. Leijnse, K. A. Dick, and C. Thelander, *Physical Review B* **94**, 115313 (2016).
- [54] M. T. Björk, B. J. Ohlsson, T. Sass, A. I. Persson, C. Thelander, M. H. Magnusson, K. Deppert, L. R. Wallenberg, and L. Samuelson, *Nano Letters* **2**, 87 (2002).
- [55] V. Zannier, F. Rossi, D. Ercolani, and L. Sorba, *Nanotechnology* **30**, 094003 (2019).
- [56] M. Leijnse and K. Flensberg, *Physical Review B* **84**, 140501 (2011).
- [57] S. Hoffman, D. Chevallier, D. Loss, and J. Klinovaja, *Physical Review B* **96** (2017), 10.1103/physrevb.96.045440.
- [58] K. Gharavi, D. Hoving, and J. Baugh, *Physical Review B* **94**, 155417 (2016).
- [59] D. Chevallier, P. Szumniak, S. Hoffman, D. Loss, and J. Klinovaja, *Physical Review B* **97**, 045404 (2018).
- [60] H. Pan and S. D. Sarma, *Physical Review Research* **2** (2020), 10.1103/physrevresearch.2.013377.
- [61] M. T. Björk, C. Thelander, A. E. Hansen, L. E. Jensen, M. W. Larsson, L. R. Wallenberg, and L. Samuelson, *Nano Letters* **4**, 1621 (2004).
- [62] I.-J. Chen, S. Lehmann, M. Nilsson, P. Kivisaari, H. Linke, K. A. Dick, and C. Thelander, *Nano Letters* **17**, 902 (2017).
- [63] Y. V. Nazarov and Y. M. Blanter, *Quantum Transport* (Cambridge University Press, 2009).
- [64] T. Heinzel, *Mesoscopic Electronics in Solid State Nanostructures* (Wiley, 2006).
- [65] T. Ihn, *Semiconductor Nanostructures* (Oxford University Press, 2009).
- [66] D. J. Griffiths and D. F. Schroeter, *Introduction to Quantum Mechanics* (Cambridge University Press, 2018).
- [67] C. Crowell and S. Sze, *Solid-State Electronics* **9**, 1035 (1966).
- [68] R. T. Tung, *Applied Physics Reviews* **1**, 011304 (2014).

-
- [69] G. Binnig, H. Rohrer, C. Gerber, and E. Weibel, *Applied Physics Letters* **40**, 178 (1982).
- [70] K. K. Likharev, *Applied Physics Letters* **73**, 2137 (1998).
- [71] J. Weis, R. J. Haug, K. v. Klitzing, and K. Ploog, *Physical Review Letters* **71**, 4019 (1993).
- [72] L. P. Kouwenhoven, N. C. van der Vaart, A. T. Johnson, W. Kool, C. J. P. M. Harmans, J. G. Williamson, A. A. M. Staring, and C. T. Foxon, *Zeitschrift für Physik B Condensed Matter* **85**, 367 (1991).
- [73] L. J. Klein, K. A. Slinker, J. L. Truitt, S. Goswami, K. L. M. Lewis, S. N. Coppersmith, D. W. van der Weide, M. Friesen, R. H. Blick, D. E. Savage, M. G. Lagally, C. Tahan, R. Joynt, M. A. Eriksson, J. O. Chu, J. A. Ott, and P. M. Mooney, *Applied Physics Letters* **84**, 4047 (2004).
- [74] R. J. Warburton, *Nature Materials* **12**, 483 (2013).
- [75] Z. Wasilewski, S. Fafard, and J. McCaffrey, *Journal of Crystal Growth* **201-202**, 1131 (1999).
- [76] A. Baumgartner, A. Chaggar, A. Patanè, L. Eaves, and M. Henini, *Applied Physics Letters* **92**, 091121 (2008).
- [77] A. Fuhrer, L. E. Fröberg, J. N. Pedersen, M. W. Larsson, A. Wacker, M.-E. Pistol, and L. Samuelson, *Nano Letters* **7**, 243 (2007).
- [78] D. Prete, P. A. Erdman, V. Demontis, V. Zannier, D. Ercolani, L. Sorba, F. Beltram, F. Rossella, F. Taddei, and S. Roddaro, *Nano Letters* **19**, 3033 (2019).
- [79] E. D. Minot, F. Kelkensberg, M. van Kouwen, J. A. van Dam, L. P. Kouwenhoven, V. Zwiller, M. T. Borgström, O. Wunnicke, M. A. Verheijen, and E. P. A. M. Bakkers, *Nano Letters* **7**, 367 (2007).
- [80] L. Romeo, S. Roddaro, A. Pitanti, D. Ercolani, L. Sorba, and F. Beltram, *Nano Letters* **12**, 4490 (2012).
- [81] L. Hofstetter, S. Csonka, J. Nygård, and C. Schönberger, *Nature* **461**, 960 (2009).
- [82] M. T. Björk, A. Fuhrer, A. E. Hansen, M. W. Larsson, L. E. Fröberg, and L. Samuelson, *Physical Review B* **72**, 201307 (2005).
- [83] G. Fábíán, P. Makk, M. H. Madsen, J. Nygård, C. Schönberger, and A. Baumgartner, *Physical Review B* **94** (2016), 10.1103/physrevb.94.195415.
- [84] S. Cornia, F. Rossella, V. Demontis, V. Zannier, F. Beltram, L. Sorba, M. Affronte, and A. Ghirri, *Scientific Reports* **9** (2019), 10.1038/s41598-019-56053-2.
- [85] A. Das, Y. Ronen, M. Heiblum, D. Mahalu, A. V. Kretinin, and H. Shtrikman, *Nature Communications* **3** (2012), 10.1038/ncomms2169.

- [86] R. M. Lutchyn, E. P. A. M. Bakkers, L. P. Kouwenhoven, P. Krogstrup, C. M. Marcus, and Y. Oreg, *Nature Reviews Materials* **3**, 52 (2018).
- [87] F. S. Thomas, A. Baumgartner, L. Gubser, C. Jünger, G. Fülöp, M. Nilsson, F. Rossi, V. Zannier, L. Sorba, and C. Schönenberger, *Nanotechnology* **31**, 135003 (2020).
- [88] A. Bordoloi, V. Zannier, L. Sorba, C. Schönenberger, and A. Baumgartner, *Communications Physics* **3** (2020), 10.1038/s42005-020-00405-2.
- [89] Y. Hu, H. O. H. Churchill, D. J. Reilly, J. Xiang, C. M. Lieber, and C. M. Marcus, *Nature Nanotechnology* **2**, 622 (2007).
- [90] Z. S. Momtaz, S. Servino, V. Demontis, V. Zannier, D. Ercolani, F. Rossi, F. Rossella, L. Sorba, F. Beltram, and S. Roddaro, *Nano Letters* **20**, 1693 (2020).
- [91] A. C. Bleszynski-Jayich, L. E. Fröberg, M. T. Björk, H. J. Trodahl, L. Samuelson, and R. M. Westervelt, *Physical Review B* **77** (2008), 10.1103/physrevb.77.245327.
- [92] S. Dorsch, A. Svilans, M. Josefsson, B. Goldozian, M. Kumar, C. Thelander, A. Wacker, and A. Burke, arXiv e-prints, arXiv:2003.11357.
- [93] G. Fülöp, F. Domínguez, S. d’Hollósy, A. Baumgartner, P. Makk, M. Madsen, V. Guzenko, J. Nygård, C. Schönenberger, A. L. Yeyati, and S. Csonka, *Physical Review Letters* **115** (2015), 10.1103/physrevlett.115.227003.
- [94] L. B. Wang, D. Pan, G. Y. Huang, J. Zhao, N. Kang, and H. Q. Xu, *Nanotechnology* **30**, 124001 (2019).
- [95] S. Roddaro, A. Pescaglini, D. Ercolani, L. Sorba, and F. Beltram, *Nano Letters* **11**, 1695 (2011).
- [96] M. Bockrath, *Science* **275**, 1922 (1997).
- [97] M. Olek, T. Büsgen, M. Hilgendorff, and M. Giersig, *The Journal of Physical Chemistry B* **110**, 12901 (2006).
- [98] M. Eich, R. Pisoni, A. Pally, H. Overweg, A. Kurzmann, Y. Lee, P. Rickhaus, K. Watanabe, T. Taniguchi, K. Ensslin, and T. Ihn, *Nano Letters* **18**, 5042 (2018).
- [99] S. Caneva, M. Hermans, M. Lee, A. García-Fuente, K. Watanabe, T. Taniguchi, C. Dekker, J. Ferrer, H. S. J. van der Zant, and P. Gehring, *Nano Letters* **20**, 4924 (2020).
- [100] S. Wang, N. Kharche, E. C. Girão, X. Feng, K. Müllen, V. Meunier, R. Fasel, and P. Ruffieux, *Nano Letters* **17**, 4277 (2017).
- [101] M. E. Abbasi, M. L. Perrin, G. B. Barin, S. Sangtarash, J. Overbeck, O. Braun, C. J. Lambert, Q. Sun, T. Pechtl, A. Narita, K. Müllen, P. Ruffieux, H. Sadeghi, R. Fasel, and M. Calame, *ACS Nano* **14**, 5754 (2020).

-
- [102] L. P. Kouwenhoven, D. G. Austing, and S. Tarucha, *Reports on Progress in Physics* **64**, 701 (2001).
- [103] J. Gramich, *Andreev and Spin Transport in Carbon Nanotube Quantum Dot Hybrid Devices*, Ph.D. thesis, University of Basel (2016).
- [104] C. Jünger, *Transport Spectroscopy of Semiconductor Superconductor Nanowire Hybrid Devices*, Ph.D. thesis, University of Basel (2019).
- [105] H. van Houten, *Surface Science* **263**, 442 (1992).
- [106] S. d'Hollosy, *Locally Tunable InAs Nanowire Quantum Dots for Cooper Pair Splitting*, Ph.D. thesis, University of Basel (2014).
- [107] G. Abulizi, *Quantum transport in hexagonal boron nitride-carbon nanotube heterostructures*, Ph.D. thesis, University of Basel (2018).
- [108] G. Fábíán, *Engineered Magnetoconductance in InAs Nanowire Quantum Dots*, Ph.D. thesis, University of Basel (2015).
- [109] W. G. van der Wiel, S. D. Franceschi, J. M. Elzerman, T. Fujisawa, S. Tarucha, and L. P. Kouwenhoven, *Reviews of Modern Physics* **75**, 1 (2002).
- [110] T. Löfwander, V. S. Shumeiko, and G. Wendin, *Superconductor Science and Technology* **14**, R53 (2001).
- [111] T. Dirks, T. L. Hughes, S. Lal, B. Uchoa, Y.-F. Chen, C. Chialvo, P. M. Goldbart, and N. Mason, *Nature Physics* **7**, 386 (2011).
- [112] J. Bardeen, L. N. Cooper, and J. R. Schrieffer, *Physical Review* **108**, 1175 (1957).
- [113] D. Griffiths, *Introduction to quantum mechanics* (Pearson Prentice Hall, Upper Saddle River, NJ, 2005).
- [114] H. M. Rosenberg, *The solid state : an introduction to the physics of crystals for students of physics, materials science, and engineering* (Clarendon Press, Oxford England, 1975).
- [115] G. E. Blonder, M. Tinkham, and T. M. Klapwijk, *Physical Review B* **25**, 4515 (1982).
- [116] I. Kulik, *Quantum Mesoscopic Phenomena and Mesoscopic Devices in Microelectronics* (Springer Netherlands Imprint Springer, Dordrecht, 2000).
- [117] A. F. Andreev, *Soviet Physics Uspekhi* **19**, 137 (1976).
- [118] D. Rainis, L. Trifunovic, J. Klinovaja, and D. Loss, *Physical Review B* **87** (2013), 10.1103/physrevb.87.024515.
- [119] L. Fu, *Physical Review Letters* **104** (2010), 10.1103/physrevlett.104.056402.
- [120] A. Y. Kitaev, *Physics-Uspekhi* **44**, 131 (2001).

- [121] A. Das, Y. Ronen, Y. Most, Y. Oreg, M. Heiblum, and H. Shtrikman, *Nature Physics* **8**, 887 (2012).
- [122] S. Plugge, A. Rasmussen, R. Egger, and K. Flensberg, *New Journal of Physics* **19**, 012001 (2017).
- [123] S. Nadj-Perge, S. M. Frolov, J. W. W. van Tilburg, J. Danon, Y. V. Nazarov, R. Algra, E. P. A. M. Bakkers, and L. P. Kouwenhoven, *Physical Review B* **81** (2010), 10.1103/physrevb.81.201305.
- [124] D. Liang and X. P. Gao, *Nano Letters* **12**, 3263 (2012).
- [125] S. Nadj-Perge, S. M. Frolov, E. P. A. M. Bakkers, and L. P. Kouwenhoven, *Nature* **468**, 1084 (2010).
- [126] F. Vigneau, V. Prudkovkiy, I. Duchemin, W. Escoffier, P. Caroff, Y.-M. Niquet, R. Leturcq, M. Goiran, and B. Raquet, *Physical Review Letters* **112** (2014), 10.1103/physrevlett.112.076801.
- [127] S. Dhara, H. S. Solanki, V. Singh, A. Narayanan, P. Chaudhari, M. Gokhale, A. Bhattacharya, and M. M. Deshmukh, *Physical Review B* **79** (2009), 10.1103/physrevb.79.121311.
- [128] S. F. Karg, V. Troncale, U. Drechsler, P. Mensch, P. D. Kanungo, H. Schmid, V. Schmidt, L. Gignac, H. Riel, and B. Gotsmann, *Nanotechnology* **25**, 305702 (2014).
- [129] S. Upadhyay, R. Frederiksen, N. Lloret, L. D. Vico, P. Krogstrup, J. H. Jensen, K. L. Martinez, and J. Nygård, *Applied Physics Letters* **104**, 203504 (2014).
- [130] J. Du, D. Liang, H. Tang, and X. P. Gao, *Nano Letters* **9**, 4348 (2009).
- [131] P. Offermans, M. Crego-Calama, and S. Brongersma, *Sensors and Actuators B: Chemical* **161**, 1144 (2012).
- [132] Y. Chen, D. Liang, X. P. A. Gao, and J. I. D. Alexander, *Nano Letters* **13**, 3953 (2013).
- [133] R. R. LaPierre, M. Robson, K. M. Azizur-Rahman, and P. Kuyanov, *Journal of Physics D: Applied Physics* **50**, 123001 (2017).
- [134] A. D. Mallorquí, E. Alarcón-Lladó, E. Russo-Averchi, G. Tütüncüoğlu, F. Matteini, D. Ruffer, and A. F. i Morral, *Journal of Physics D: Applied Physics* **47**, 394017 (2014).
- [135] W. Wei, X.-Y. Bao, C. Soci, Y. Ding, Z.-L. Wang, and D. Wang, *Nano Letters* **9**, 2926 (2009).
- [136] Y. Han, X. Zheng, M. Fu, D. Pan, X. Li, Y. Guo, J. Zhao, and Q. Chen, *Physical Chemistry Chemical Physics* **18**, 818 (2016).
- [137] E. C. Garnett, M. L. Brongersma, Y. Cui, and M. D. McGehee, *Annual Review of Materials Research* **41**, 269 (2011).

- [138] G. Otnes and M. T. Borgström, *Nano Today* **12**, 31 (2017).
- [139] C. Yang, C. J. Barrelet, F. Capasso, and C. M. Lieber, *Nano Letters* **6**, 2929 (2006).
- [140] M. B. Rota, A. S. Ameruddin, H. A. Fonseka, Q. Gao, F. Mura, A. Polimeni, A. Miriametro, H. H. Tan, C. Jagadish, and M. Capizzi, *Nano Letters* **16**, 5197 (2016).
- [141] Y.-S. Kim, K. Hummer, and G. Kresse, *Physical Review B* **80**, 035203 (2009).
- [142] S. Csonka, L. Hofstetter, F. Freitag, S. Oberholzer, C. Schönenberger, T. S. Jespersen, M. Aagesen, and J. Nygård, *Nano Letters* **8**, 3932 (2008).
- [143] T. S. Jespersen, M. Aagesen, C. Sørensen, P. E. Lindelof, and J. Nygård, *Physical Review B* **74** (2006), 10.1103/physrevb.74.233304.
- [144] N. Gupta, Y. Song, G. W. Holloway, U. Sinha, C. M. Haapamaki, R. R. LaPierre, and J. Baugh, *Nanotechnology* **24**, 225202 (2013).
- [145] S. Dayeh, D. P. Aplin, X. Zhou, P. K. Yu, E. Yu, and D. Wang, *Small* **3**, 326 (2007).
- [146] A. C. Ford, J. C. Ho, Y.-L. Chueh, Y.-C. Tseng, Z. Fan, J. Guo, J. Bokor, and A. Javey, *Nano Letters* **9**, 360 (2009).
- [147] C. Fasth, A. Fuhrer, L. Samuelson, V. N. Golovach, and D. Loss, *Physical Review Letters* **98**, 266801 (2007).
- [148] R. S. Wagner and W. C. Ellis, *Applied Physics Letters* **4**, 89 (1964).
- [149] X. Yan, X. Zhang, X. Ren, H. Huang, J. Guo, X. Guo, M. Liu, Q. Wang, S. Cai, and Y. Huang, *Nano Letters* **11**, 3941 (2011).
- [150] M. Tchernycheva, L. Travers, G. Patriarche, F. Glas, J.-C. Harmand, G. E. Cirlin, and V. G. Dubrovskii, *Journal of Applied Physics* **102**, 094313 (2007).
- [151] L. E. Jensen, M. T. Björk, S. Jeppesen, A. I. Persson, B. J. Ohlsson, and L. Samuelson, *Nano Letters* **4**, 1961 (2004).
- [152] U. P. Gomes, D. Ercolani, V. Zannier, S. Battiato, E. Ubyivovk, V. Mikhailovskii, Y. Murata, S. Heun, F. Beltram, and L. Sorba, *Nanotechnology* **28**, 065603 (2017).
- [153] K. A. Dick, K. Deppert, T. Mårtensson, B. Mandl, L. Samuelson, and W. Seifert, *Nano Letters* **5**, 761 (2005).
- [154] P. Caroff, K. A. Dick, J. Johansson, M. E. Messing, K. Deppert, and L. Samuelson, *Nature Nanotechnology* **4**, 50 (2008).
- [155] M. E. Messing, K. Hillerich, J. Bolinsson, K. Storm, J. Johansson, K. A. Dick, and K. Deppert, *Nano Research* **3**, 506 (2010).
- [156] A. I. Hochbaum, R. Fan, R. He, and P. Yang, *Nano Letters* **5**, 457 (2005).

- [157] U. P. Gomes, D. Ercolani, V. Zannier, F. Beltram, and L. Sorba, *Semiconductor Science and Technology* **30**, 115012 (2015).
- [158] P. H. M. Böttger, Z. Bi, D. Adolph, K. A. Dick, L. S. Karlsson, M. N. A. Karlsson, B. A. Wacaser, and K. Deppert, *Nanotechnology* **18**, 105304 (2007).
- [159] T. Mårtensson, P. Carlberg, M. Borgström, L. Montelius, W. Seifert, and L. Samuelson, *Nano Letters* **4**, 699 (2004).
- [160] M. Nilsson, *Charge and Spin Transport in Parallel-Coupled Quantum Dots in Nanowires*, Ph.D. thesis, Faculty of Engineering, LTH (2018).
- [161] J. Johansson, K. A. Dick, P. Caroff, M. E. Messing, J. Bolinsson, K. Deppert, and L. Samuelson, *The Journal of Physical Chemistry C* **114**, 3837 (2010).
- [162] S. Lehmann, J. Wallentin, D. Jacobsson, K. Deppert, and K. A. Dick, *Nano Letters* **13**, 4099 (2013).
- [163] S. M. Albrecht, A. P. Higginbotham, M. Madsen, F. Kuemmeth, T. S. Jespersen, J. Nygård, P. Krogstrup, and C. M. Marcus, *Nature* **531**, 206 (2016).
- [164] D. Ercolani, F. Rossi, A. Li, S. Roddaro, V. Grillo, G. Salviati, F. Beltram, and L. Sorba, *Nanotechnology* **20**, 505605 (2009).
- [165] D. Ercolani, M. Gemmi, L. Nasi, F. Rossi, M. Pea, A. Li, G. Salviati, F. Beltram, and L. Sorba, *Nanotechnology* **23**, 115606 (2012).
- [166] J. Treu, M. Bormann, H. Schmeiduch, M. Döblinger, S. Morkötter, S. Matich, P. Wiecha, K. Saller, B. Mayer, M. Bichler, M.-C. Amann, J. J. Finley, G. Abstreiter, and G. Koblmüller, *Nano Letters* **13**, 6070 (2013).
- [167] J. W. W. van Tilburg, R. E. Algra, W. G. G. Immink, M. Verheijen, E. P. A. M. Bakkers, and L. P. Kouwenhoven, *Semiconductor Science and Technology* **25**, 024011 (2010).
- [168] C. Blömers, T. Rieger, P. Zellekens, F. Haas, M. I. Lepsa, H. Hardtdegen, . Gül, N. Demarina, D. Grützmacher, H. Lüth, and T. Schäpers, *Nanotechnology* **24**, 035203 (2012).
- [169] D. Kriegner, C. Panse, B. Mandl, K. A. Dick, M. Keplinger, J. M. Persson, P. Caroff, D. Ercolani, L. Sorba, F. Bechstedt, J. Stangl, and G. Bauer, *Nano Letters* **11**, 1483 (2011).
- [170] Z. Zanolli, F. Fuchs, J. Furthmüller, U. von Barth, and F. Bechstedt, *Physical Review B* **75** (2007), 10.1103/physrevb.75.245121.
- [171] L. C. O. Dacal and A. Cantarero, *Materials Research Express* **1**, 015702 (2014).
- [172] M. Speckbacher, J. Treu, T. J. Whittles, W. M. Linhart, X. Xu, K. Saller, V. R. Dhanak, G. Abstreiter, J. J. Finley, T. D. Veal, and G. Koblmüller, *Nano Letters* **16**, 5135 (2016).
- [173] V. E. Degtyarev, S. V. Khazanova, and N. V. Demarina, *Scientific Reports* **7** (2017), 10.1038/s41598-017-03415-3.

- [174] Z. Liu, Z. Zhang, R. Jiang, X. Li, M. Zhang, and D. Qiu, *Scripta Materialia* **121**, 79 (2016).
- [175] Y. Xiong, H. Tang, X. Wang, Y. Zhao, Q. Fu, J. Yang, and D. Xu, *Scientific Reports* **7** (2017), 10.1038/s41598-017-13792-4.
- [176] D. Lynall, S. V. Nair, D. Gutstein, A. Shik, I. G. Savelyev, M. Blumin, and H. E. Ruda, *Nano Letters* **18**, 1387 (2018).
- [177] H.-Y. Cheung, S. Yip, N. Han, G. Dong, M. Fang, Z. xing Yang, F. Wang, H. Lin, C.-Y. Wong, and J. C. Ho, *ACS Nano* **9**, 7545 (2015).
- [178] Q. Hang, F. Wang, P. D. Carpenter, D. Zemlyanov, D. Zakharov, E. A. Stach, W. E. Buhro, and D. B. Janes, *Nano Letters* **8**, 49 (2008).
- [179] S. Heedt, I. Otto, K. Sladek, H. Hardtdegen, J. Schubert, N. Demarina, H. Lüth, D. Grützmacher, and T. Schäpers, *Nanoscale* **7**, 18188 (2015).
- [180] M. J. L. Sourribes, I. Isakov, M. Panfilova, and P. A. Warburton, *Nanotechnology* **24**, 045703 (2013).
- [181] S. Heedt, W. Prost, J. Schubert, D. Grützmacher, and T. Schäpers, *Nano Letters* **16**, 3116 (2016).
- [182] Z. Scherübl, G. Fülöp, M. H. Madsen, J. Nygård, and S. Csonka, *Physical Review B* **94** (2016), 10.1103/physrevb.94.035444.
- [183] A. Iorio, M. Rocci, L. Bours, M. Carrega, V. Zannier, L. Sorba, S. Roddaro, F. Giazotto, and E. Strambini, *Nano Letters* **19**, 652 (2018).
- [184] S. Heedt, N. T. Ziani, F. Crépin, W. Prost, S. Trellenkamp, J. Schubert, D. Grützmacher, B. Trauzettel, and T. Schäpers, *Nature Physics* **13**, 563 (2017).
- [185] B. H. Hong, J. Y. Lee, T. Beetz, Y. Zhu, P. Kim, and K. S. Kim, *Journal of the American Chemical Society* **127**, 15336 (2005).
- [186] N. Mason, *Science* **303**, 655 (2004).
- [187] M. J. Biercuk, S. Garaj, N. Mason, J. M. Chow, and C. M. Marcus, *Nano Letters* **5**, 1267 (2005).
- [188] M. J. Biercuk, N. Mason, J. M. Chow, and C. M. Marcus, *Nano Letters* **4**, 2499 (2004).
- [189] H. Aurich, A. Baumgartner, F. Freitag, A. Eichler, J. Trbovic, and C. Schönenberger, *Applied Physics Letters* **97**, 153116 (2010).
- [190] J. Samm, J. Gramich, A. Baumgartner, M. Weiss, and C. Schönenberger, *Journal of Applied Physics* **115**, 174309 (2014).
- [191] J. Gramich, A. Baumgartner, and C. Schönenberger, *Applied Physics Letters* **108**, 172604 (2016).

- [192] J. Gramich, A. Baumgartner, and C. Schönenberger, *Physical Review B* **96** (2017), [10.1103/physrevb.96.195418](#).
- [193] J. Gramich, A. Baumgartner, and C. Schönenberger, *Physical Review Letters* **115** (2015), [10.1103/physrevlett.115.216801](#).
- [194] A. Eichler, M. Weiss, S. Oberholzer, C. Schönenberger, A. L. Yeyati, J. C. Cuevas, and A. Martín-Rodero, *Physical Review Letters* **99** (2007), [10.1103/physrevlett.99.126602](#).
- [195] J. Schindele, A. Baumgartner, R. Maurand, M. Weiss, and C. Schönenberger, *Physical Review B* **89** (2014), [10.1103/physrevb.89.045422](#).
- [196] J. Schindele, A. Baumgartner, and C. Schönenberger, *Physical Review Letters* **109** (2012), [10.1103/physrevlett.109.157002](#).
- [197] A. Javey, J. Guo, Q. Wang, M. Lundstrom, and H. Dai, *Nature* **424**, 654 (2003).
- [198] E. Pop, D. Mann, Q. Wang, K. Goodson, and H. Dai, *Nano Letters* **6**, 96 (2006).
- [199] E. A. Laird, F. Kuemmeth, G. A. Steele, K. Grove-Rasmussen, J. Nygård, K. Flensberg, and L. P. Kouwenhoven, *Reviews of Modern Physics* **87**, 703 (2015).
- [200] B. Braunecker, P. Simon, and D. Loss, *Physical Review B* **80** (2009), [10.1103/physrevb.80.165119](#).
- [201] R. Saito, G. Dresselhaus, and M. S. Dresselhaus, *Physical Properties of Carbon Nanotubes* (1998).
- [202] M. Yu, *Science* **287**, 637 (2000).
- [203] J. Furer, *Growth of Single-Wall Carbon Nanotubes by Chemical Vapor Deposition for Electrical Devices*, *Ph.D. thesis*, University of Basel (2006).
- [204] M. R. Graeber, *Accessing the quantum world through electronic transport in carbon nanotubes*, *Ph.D. thesis*, University of Basel (2006).
- [205] J. Kong, H. T. Soh, A. M. Cassell, C. F. Quate, and H. Dai, *Nature* **395**, 878 (1998).
- [206] X. Li, X. Tu, S. Zaric, K. Welsher, W. S. Seo, W. Zhao, and H. Dai, *Journal of the American Chemical Society* **129**, 15770 (2007).
- [207] A. H. C. Neto, F. Guinea, N. M. R. Peres, K. S. Novoselov, and A. K. Geim, *Reviews of Modern Physics* **81**, 109 (2009).
- [208] C. Handschin, *Quantum Transport in Encapsulated Graphene P-N junctions*, *Ph.D. thesis*, University of Basel (2017).
- [209] S. Zihlmann, *Spin and charge relaxation in graphene*, *Ph.D. thesis*, University of Basel (2018).

- [210] N. Saifuddin, A. Z. Raziah, and A. R. Junizah, *Journal of Chemistry* **2013**, 1 (2013).
- [211] T. Hasler, *Microwave noise detection of a quantum dot with stub impedance matching*, Ph.D. thesis, University of Basel (2016).
- [212] V. Ranjan, *Admittance and noise detection in mesoscopic systems via GHz impedance matching*, Ph.D. thesis, University of Basel (2017).
- [213] D. B. Suyatin, C. Thelander, M. T. Björk, I. Maximov, and L. Samuelson, *Nanotechnology* **18**, 105307 (2007).
- [214] S. Pournia, S. Linser, G. Jnawali, H. E. Jackson, L. M. Smith, A. Ameruddin, P. Caroff, J. Wong-Leung, H. H. Tan, C. Jagadish, and H. J. Joyce, *Nano Research* **13**, 1586 (2020).
- [215] A. R. Ullah, H. J. Joyce, H. H. Tan, C. Jagadish, and A. P. Micolich, *Nanotechnology* **28**, 454001 (2017).
- [216] F. Pobell, *Matter and Methods at Low Temperatures* (Springer Berlin Heidelberg, 2007).
- [217] J. M. Elzerman, R. Hanson, J. S. Greidanus, L. H. W. van Beveren, S. D. Franceschi, L. M. K. Vandersypen, S. Tarucha, and L. P. Kouwenhoven, *Physical Review B* **67** (2003), 10.1103/physrevb.67.161308.
- [218] R. Hanson, L. P. Kouwenhoven, J. R. Petta, S. Tarucha, and L. M. K. Vandersypen, *Reviews of Modern Physics* **79**, 1217 (2007).
- [219] B. Liu, A. Abbas, and C. Zhou, *Advanced Electronic Materials* **3**, 1700045 (2017).
- [220] S. Nadj-Perge, V. S. Pribiag, J. W. G. van den Berg, K. Zuo, S. R. Plissard, E. P. A. M. Bakkers, S. M. Frolov, and L. P. Kouwenhoven, *Physical Review Letters* **108** (2012), 10.1103/physrevlett.108.166801.
- [221] X.-X. Song, D. Liu, V. Mosallanejad, J. You, T.-Y. Han, D.-T. Chen, H.-O. Li, G. Cao, M. Xiao, G.-C. Guo, and G.-P. Guo, *Nanoscale* **7**, 16867 (2015).
- [222] K. Lee, G. Kulkarni, and Z. Zhong, *Nanoscale* **8**, 7755 (2016).
- [223] M. T. Björk, B. J. Ohlsson, T. Sass, A. I. Persson, C. Thelander, M. H. Magnusson, K. Deppert, L. R. Wallenberg, and L. Samuelson, *Applied Physics Letters* **80**, 1058 (2002).
- [224] Y.-M. Niquet and D. C. Mojica, *Physical Review B* **77**, 115316 (2008).
- [225] S. Aghaieimbodi, C.-M. Lee, M. A. Buyukkaya, C. J. K. Richardson, and E. Waks, *Applied Physics Letters* **114**, 071105 (2019).
- [226] F. Rossella, A. Bertoni, D. Ercolani, M. Rontani, L. Sorba, F. Beltram, and S. Roddaro, *Nature Nanotechnology* **9**, 997 (2014).
- [227] S. Lindemann, T. Ihn, S. Bieri, T. Heinzel, K. Ensslin, G. Hackenbroich, K. Maranowski, and A. C. Gossard, *Physical Review B* **66**, 161312 (2002).

- [228] Z. I. Alferov, *Semiconductors* **32**, 1 (1998).
- [229] J. K. Hyun, S. Zhang, and L. J. Lauhon, *Annual Review of Materials Research* **43**, 451 (2013).
- [230] M. Fox and R. Ispasoiu, in *Springer Handbook of Electronic and Photonic Materials* (Springer International Publishing, 2017) pp. 1–1.
- [231] K. Hirose and N. S. Wingreen, *Physical Review B* **59**, 4604 (1999).
- [232] C. W. J. Beenakker, *Physical Review B* **44**, 1646 (1991).
- [233] A. D. Stone and P. A. Lee, *Physical Review Letters* **54**, 1196 (1985).
- [234] M. Büttiker, *Physical Review B* **33**, 3020 (1986).
- [235] E. B. Foxman, P. L. McEuen, U. Meirav, N. S. Wingreen, Y. Meir, P. A. Belk, N. R. Belk, M. A. Kastner, and S. J. Wind, *Physical Review B* **47**, 10020 (1993).
- [236] J. P. Pekola, K. P. Hirvi, J. P. Kauppinen, and M. A. Paalanen, *Physical Review Letters* **73**, 2903 (1994).
- [237] M. Palma, C. P. Scheller, D. Maradan, A. V. Feshchenko, M. Meschke, and D. M. Zumbühl, *Applied Physics Letters* **111**, 253105 (2017).
- [238] T. Ihn, *Semiconductor Nanostructures*, 347 (Oxford University Press, 2009).
- [239] A. De and C. E. Pryor, *Physical Review B* **81**, 155210 (2010).
- [240] C. C. Escott, F. A. Zwanenburg, and A. Morello, *Nanotechnology* **21**, 274018 (2010).
- [241] M. Fuechsle, J. A. Miwa, S. Mahapatra, H. Ryu, S. Lee, O. Warschkow, L. C. L. Hollenberg, G. Klimeck, and M. Y. Simmons, *Nature Nanotechnology* **7**, 242 (2012).
- [242] G. P. Lansbergen, R. Rahman, C. J. Wellard, I. Woo, J. Caro, N. Collaert, S. Biesemans, G. Klimeck, L. C. L. Hollenberg, and S. Rogge, *Nature Physics* **4**, 656 (2008).
- [243] S. J. Angus, A. J. Ferguson, A. S. Dzurak, and R. G. Clark, *Nano Letters* **7**, 2051 (2007).
- [244] M. Möttönen, K. Y. Tan, K. W. Chan, F. A. Zwanenburg, W. H. Lim, C. C. Escott, J.-M. Pirkkalainen, A. Morello, C. Yang, J. A. van Donkelaar, A. D. C. Alves, D. N. Jamieson, L. C. L. Hollenberg, and A. S. Dzurak, *Physical Review B* **81** (2010), 10.1103/physrevb.81.161304.
- [245] P. Gehring, J. K. Sowa, J. Cremers, Q. Wu, H. Sadeghi, Y. Sheng, J. H. Warner, C. J. Lambert, G. A. D. Briggs, and J. A. Mol, *ACS Nano* **11**, 5325 (2017).
- [246] C. Rössler, B. Küng, S. Dröscher, T. Choi, T. Ihn, K. Ensslin, and M. Beck, *Applied Physics Letters* **97**, 152109 (2010).

-
- [247] T. Ihn, S. Gustavsson, U. Gasser, B. Küng, T. Müller, R. Schleser, M. Sigrist, I. Shorubalko, R. Leturcq, and K. Ensslin, *Solid State Communications* **149**, 1419 (2009).
- [248] L. Viti, M. S. Vitiello, D. Ercolani, L. Sorba, and A. Tredicucci, *Nanoscale Research Letters* **7**, 159 (2012).
- [249] C.-X. Liu, J. D. Sau, T. D. Stanescu, and S. D. Sarma, *Physical Review B* **96** (2017), 10.1103/physrevb.96.075161.
- [250] N. A. Court, A. J. Ferguson, and R. G. Clark, *Superconductor Science and Technology* **21**, 015013 (2007).
- [251] S. Guéron, H. Pothier, N. O. Birge, D. Esteve, and M. H. Devoret, *Physical Review Letters* **77**, 3025 (1996).
- [252] V. Cherkez, J. Cuevas, C. Brun, T. Cren, G. Ménard, F. Debontridder, V. Stolyarov, and D. Roditchev, *Physical Review X* **4** (2014), 10.1103/physrevx.4.011033.
- [253] A. L. Yeyati, J. C. Cuevas, A. López-Dávalos, and A. Martín-Rodero, *Physical Review B* **55**, R6137 (1997).
- [254] R. C. Dynes, V. Narayanamurti, and J. P. Garno, *Physical Review Letters* **41**, 1509 (1978).
- [255] P. F. Bagwell, *Physical Review B* **46**, 12573 (1992).
- [256] J. D. Sau, R. M. Lutchyn, S. Tewari, and S. D. Sarma, *Physical Review Letters* **104** (2010), 10.1103/physrevlett.104.040502.
- [257] C. Reeg, O. Dmytruk, D. Chevallier, D. Loss, and J. Klinovaja, *Physical Review B* **98** (2018), 10.1103/physrevb.98.245407.

A Fabrication Recipes

The fabrication techniques used in this thesis are discussed in Chapter 4. This appendix provides details of the fabrication recipes.

A.1. Bottom gate structures

Wafer Characteristics

- **Substrate:** Undoped silicon
- **Resistivity:** $>5000 \Omega \text{ m}$
- **Caping Layer:** 170 nm thick thermally grown SiO_2

Wafer Cleaning

1. Dice the wafer into 2.5 x 2.5 cm pieces
2. Sonicate in acetone for 15 min.
3. Sonicate in IPA for 15 min.
4. Dry with N_2
5. 5 min min UV cleaning

E-beam Lithography

- **Resist:** PMMA 950K dissolved in Chlorobenzene
- **Spin Coating:** 4000 RPM for 40 s results in a thickness of $\sim 300 \text{ nm}$
- **Hardening:** 180°C on a hotplate for 3 min
- **Area Dose:** $230 \mu\text{C}/\text{cm}^2$ at 20 kV and high current mode
- **Development:** 3 : 1 IPA/MIBK at -15°C for 60 s

Evaporation

- **Evaporator:** Sharon
- **Material:** 5 nm Ti and 45 nm Au
- **Liftoff:** in Aceton at 50 °C for 1 h

Si₃N₄ deposition

- **Material:** 50 nm of Si₃N₄
- **Deposition:** Plasma enhanced CVD (PE-CVD) at PSI.

Si₃N₄ etching

- **Resist:** PMMA dissolved in Chlorobenzene
- **Spin Coating:** 4000 RPM for 40 s results in a thickness of ~500 nm
- **Hardening:** 180 °C on a hotplate for 3 min
- **Area Dose:** 200 $\mu\text{C}/\text{cm}^2$ at 20 kV
- **Development:** 3 : 1 IPA/MIBK for 60 s
- **Plasma etching in Oxford RIE:**
 - Parameters: CHF₃ 25 sccm, O₂ 4 sccm, 50 mTorr, 50 W, 2 min

A.2. Carbon nanotube stamps

Wafer Characteristics

- **Substrate:** Undoped Silicon
- **Resistivity:** >5000 $\Omega\text{ m}$
- **Caping Layer:** 170 nm thick thermally grown SiO₂

Patterning pillers

- **Electron beam lithography with PMMA/HSQ bilayer:**
 - Spin-coat 1 μm PMMA
 - Bake at 180 °C for 3 min
 - Spin-coat HSQ (6000 rpm for 60 s)

- Bake at 90 °C for 5 min
- Use 20 kV acceleration voltage and 120 μm aperture
- Area dose: 200 $\mu\text{C}/\text{cm}^2$

- **Development:**

- 25 s in TMAH (25% solution)
- Stop in H_2O and blow dry with N_2

Pillar etching

- **PMMA removal in RIE**

- Parameters: O_2 16 sccm, 250 mTorr, 100 W, 10 min

- **SiO_2 etching**

- Wet etch in buffered HF (5%) for 7 min
- Etch rate: 35 nm min^{-1}

- **Si etching in RIE**

- Parameters: SF_6 13 sccm, O_2 5 sccm, 75 mTorr, 100 W, 5 min
- Resulting pillar height: 4 μm

Carbon nanotube growth

- **Catalyst solution:**

- 30 mg of Al_2O_3 , 93 mg of $\text{Fe}(\text{NO}_3)_3 \cdot 9\text{H}_2\text{O}$, and 27 mg of MoO_2Cl_2 dissolved in 60 mL of IPA
- Sonicate in high-power cell disrupter for 1 h
- Spin-coat one droplet of the solution onto the CNT stamps at 4000 rpm for 30 s. Repeat this five times.

- **CNT Growth:**

- Place stamps into CVD oven and heat to 950 °C under Ar (1500 sccm) and H_2 (500 sccm) flow.
- Growth: replace Ar by CH_4 (1000 sccm) for 10 min
- Cooldown CVD oven under Ar and H_2 flow

- **Carbon nanotube stamping:**

- With the mask aligner, align the bottom gate structure chip with the CNT stamp chip using the optical microscope

- Bring both chips into contact and press them together
- Repeat until a sufficient amount of CNTs are on the bottom gate structure

Nanowire placement

- Micromanipulator: Narishige MMO-202 ND

A.3. Integrated tunnel barrier devices

Wafer Characteristics

- **Substrate:** Highly doped silicon
- **Dopant:** Boron (p-doped)
- **Resistivity:** 0.003 Ω m to 0.005 Ω m
- **Caping Layer:** 300 nm thick thermally grown SiO₂

Wafer Cleaning

1. Dice the wafer into 2.5 x 2.5 cm pieces
2. Sonicate in acetone for 15 min.
3. Sonicate in IPA for 15 min.
4. Dry with N₂
5. 5 min min UV cleaning

E-beam Lithography

- **Resist:** PMMA 950K dissolved in Chlorobenzene
- **Spin Coating:** 4000 RPM for 40 s results in a thickness of \sim 230 nm
- **Hardening:** 180 °C on a hotplate for 3 min
- **Area Dose:** 230 μ C/cm² at 20 kV and high current mode
- **Development:** 3 : 1 IPA/MIBK for 60 s
- **Liftoff:** 1 h in 50 °C acetone

O₂ Plasma Etching

- **Parameters:**
 - **O₂ Flow:** 60 %
 - **RF Power:** 30 W
 - **Process Pressure:** 250 Torr
 - **Time:** 60 s
- **Etch Rates:**
 - **SiO₂:** negligible
 - **PMMA:** ~20 nm/min

Sulphur passivation

Sulphur passivation was used for **all** InAs nanowire devices presented in this thesis.

1. Dilute 0.961 95 g sulfur in 10 mL of 20% NH₄S_x
2. Mix for at least 12 h at 35 °C
3. Heat 25 mL of H₂O on hotplate at 40 °C for minimum 10 min
4. Add NH₄S_x mixture to the warm H₂O
5. Etch for 2 min
6. Stop etching by rigourously stirring in H₂O for 15 s
7. Blow dry with N₂
8. Build into vacuum chamber within 5 min

Metalization

- **Ti/Au contacts:**
 - Evaporator: Sharon (e-beam)
 - Pressure: 2×10^{-7} Pa
 - Thickness: 5 nm Ti and 55 nm Au
- **Ti/Al contacts:**
 - Evaporator: Balzers (e-beam)
 - Pressure: 2×10^{-7} Pa
 - Thickness: 5 nm Ti and 55 nm Al

B Additional data of InAs/InP heterostructure nanowires with short InP segments

This section shows the results of a InAs/InP heterostructure nanowire devices with shorter InP segment widths, $\ell_{1,2} \approx 2$ nm to 3 nm. The nanowire growth batch is NW68340.

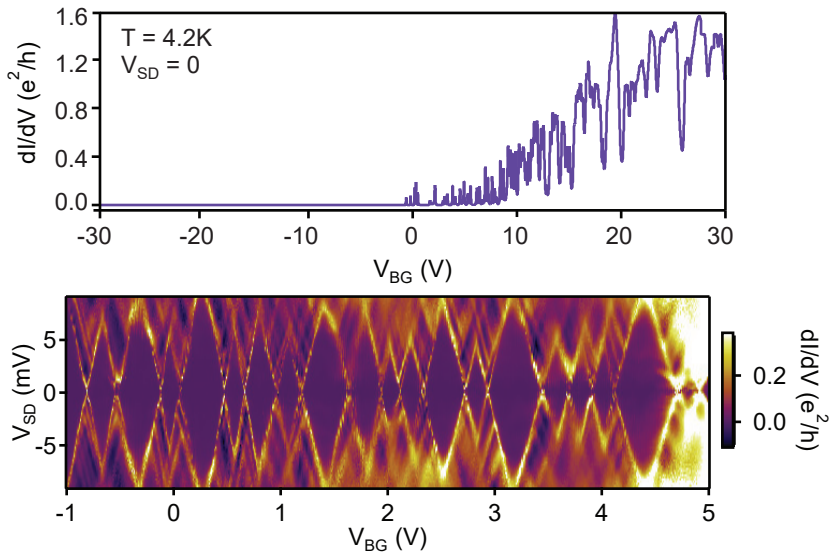


Figure B.1. Pinch-off and Coulomb blockade diamonds: (a) Differential conductance, dI/dV , as a function of back gate voltage, V_{BG} for zero source-drain voltage, V_{SD} , and at a temperature of 4.2 K. The nanowire becomes depleted around 0 V and opens around 30 V. (b) dI/dV as a function of V_{SD} and V_{BG} . Regular and stable Coulomb diamonds over a gate range of 6 V.

Figure B.1(b) shows the differential conductance, dI/dV , as a function of back gate voltage, V_{BG} for zero source-drain voltage, V_{SD} , and at a temperature of 4.2 K. We observe that the nanowire becomes depleted around 0 V and opens with $dI/dV \approx 1.4 e^2/h$ at 30 V. Figure B.1(b) shows dI/dV as a function of V_{BG} and source drain bias voltage, V_{SD} . Similarly, to the InAs/InP heterostructure devices with $\ell_{1,2} \approx 5.5$ nm, we observe very regular Coulomb blockade diamonds over a gate range of at least 6 V.

Further analysis on the integrated InP tunnel barriers was not conducted.

C Additional data of InAs/InP heterostructure nanowires

This section shows the results of another InAs/InP heterostructure nanowire device with similar geometry as the one included in Chapter 6.

Figure C.1 shows the differential conductance, dI/dV , as a function of source drain bias voltage, V_{SD} , and back gate voltage, V_{BG} . Similarly, to the previously reported device, we observe very regular Coulomb blockade diamonds over a large gate range of ~ 15 V.

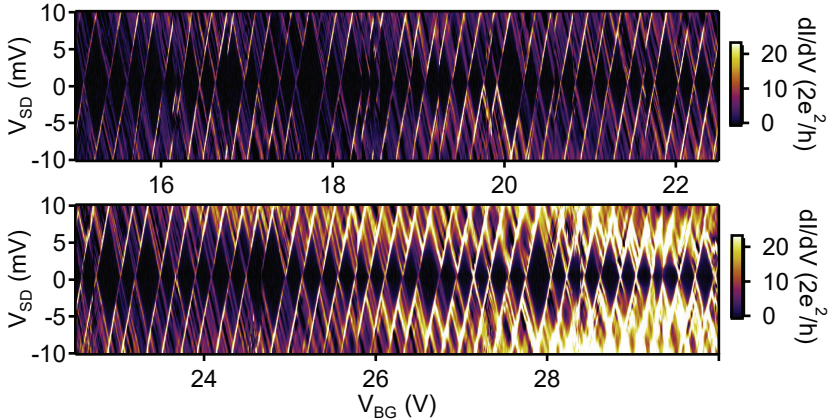


Figure C.1. Coulomb blockade diamonds: Differential conductance, dI/dV , as a function of the bias, V_{SD} , and the back gate voltage, V_{BG} . Regular and stable Coulomb diamonds were observed over a gate range of 15 V.

Further analysis on the integrated InP tunnel barriers was not conducted.

D Additional data of spectroscopy of the local density of states in nanowire leads

This section shows the model parameters for device A included in Chapter 7.

LS1 resonances	E_{LS1} (meV) (Meas.)	s_{LS1} (Meas.)	δE_{LS1} (meV) (Meas.)	Γ_{LS1} (meV) (Model)
1	0.750	0.033	0.750	0.15
2	1.30	0.035	0.55	0.40
3	2.40	0.032	1.1	0.80
4	3.30	0.034	0.9	0.50
5	4.30	0.034	1.0	1.30
6	5.40	0.034	1.1	0.10
-1	-0.45	0.031	0.45	0.15
-2	-0.80	0.033	0.35	0.4
-3	-1.20	0.035	0.40	0.2
-4	-1.70	0.034	0.50	0.2
-5	-3.0	0.032	-1.30	0.2

LS2 resonances	E_{LS2} (meV) (Meas.)	s_{LS2} (Meas.)	δE_{LS2} (meV) (Meas.)	Γ_{LS2} (meV) (Model)
1	1.0	-0.031	1	0.2
2	1.30	-0.033	0.3	0.1
3	1.70	-0.035	0.4	0.4
4	2.1	-0.034	0.4	0.4
-1	-0.70	-0.033	0.70	0.1
-2	-0.90	-0.031	0.2	0.02
-3	-1.70	-0.034	0.6	0.2
-4	-2.10	-0.031	0.4	0.1
-5	-3.30	-0.032	1.2	0.4

Table D.1. Table of each resonance in Fig. 7.8(b) with the extracted values of the absolute energies, $E_{LS1/2}$, slopes, $s_{LS1/2}$, level spacings, $\delta E_{LS1/2}$, and level broadening, $\Gamma_{LS1/2}$, for lead resonances in $LS1$ and $LS2$.

Curriculum Vitae

Frederick Stephen Thomas

Born on July 11th, 1990 in West Palm Beach, Florida, USA

Education

2016–2020 **Doctor of Philosophy in Experimental Physics at the University of Basel, Switzerland**

- Dissertation in the group of Prof. Dr. Christian Schö-
nenberger
*“Deterministic Tunnel Barriers in 1D Quantum Elec-
tronic Systems”*

2013–2015 **Master of Science in Physics at the Free University of Berlin, Germany**

- Master thesis in the group of Prof. Dr. Stefan Eisebitt
*“Characterization of sputter-deposited thin-films for
all-optical switching”*

2008–2013 **Bachelor of Science in Physics and Mathematics at Florida State University**

2004–2008 **Palm Beach Central High School, West Palm Beach, Florida, USA**

Positions

5/2016–7/2020 *Teaching assistant for physics at the University of Basel*

6/2012–9/2012 *Visiting scholar under Dr. Ruben Hühne at the Leibniz In-
stitute for Solid State and Materials Research in Dresden,
Germany*

5/2011–7/2011 *Visiting scholar under Dr. Ruben Hühne at the Leibniz In-
stitute for Solid State and Materials Research in Dresden,
Germany*

8/2009–7/2012 *Lab technician under Mr. Van Griffin at the National High
Magnetic Field Laboratory in Tallahassee, Florida*

Publications

- *“Tunnel spectroscopy of the local density of states in integrated quantum dot devices”*
F. S. Thomas, M. Nilsson, C. Ciaccia, A. Baumgartner, C. Jünger, F. Rossi, V. Zannier, L. Sorba and C. Schönenberger
in preparation
- *“Highly symmetric and tunable tunnel couplings in InAs/InP nanowire heterostructure quantum dots”*
F. S. Thomas, A. Baumgartner, L. Gubser, C. Jünger, G. Fülöp, M. Nilsson, F. Rossi, V. Zannier, L. Sorba and C. Schönenberger
[Nanotechnology](#) **31**, 135003 (2020)

Talks

- *“Electrical properties of quantum dots that are defined during growth in InAs-based nanowires using InP as barrier material”*
QCQT Research Seminar, University of Basel, Basel (Switzerland), April 2019

Poster Contributions

- *“Novel quantum transport features in low-dimensional systems”*
QSIT Winter School, Arosa (Switzerland), February 2017
- *“Towards the Helical State in Carbon Nanotubes”*
QCIT poster session, University of Basel, Basel (Switzerland), November 2017

Acknowledgements

This PhD thesis would not have been possible without the help and support from many great scientists, collaborators, colleagues, friends, and family that I have had the pleasure to meet over my life. In the following, I would like to thank everyone for supporting me in different ways in the thesis.

First of all, I would like to express my deepest gratitude to my thesis advisor Prof. Dr. Christian Schönenberger for giving me the opportunity to take part in world class research in his group. I could not imagine a better advisor and mentor for my PhD. He guided me along my entire PhD and continuously pushed me to become better. His endless passion for science and his commitment to each project was a great inspiration to me throughout my four years in his group. It never ceased to amaze me how much energy and enthusiasm he has for science. I believe this excitement and passion for science rubs off onto the entire group, leading to a wonderful working environment. I sincerely appreciate the freedom he gave to explore new projects and am extremely thankful for the opportunity to switch projects after two years. I also had the opportunity to work first hand with him in the lab setting up the new Helium-3 system. Despite both of us having to work in uncomfortable positions underneath the cryostat for several days, it was a great time that I will never forget. I feel privileged to have spent the last four years learning from such an exceptional person and the lessons I have learned during these last four years from him will leave an everlasting impression on me.

I am very thankful for Prof. Dr. Szabolcs Csonka, Prof. Dr. Stefano Roddaro, and Prof. Dr. Dominik Zumbühl for being part of my PhD defense committee. I sincerely appreciate you for reading my thesis and taking the time to attend my defense. It was an honor to have such exceptional scientists as part of my PhD committee.

This thesis could not have been written without the continuous help of Dr. Andreas Baumgartner over the past four years. His expertise in lock-in measurements, dilution refrigerators, scientific writing, and programming helped in every aspect of this thesis. He constantly pushed my understanding the limit, then expanded it further. Outside of physics, he was always very involved in the group, taking time out of his very busy schedule to speak with us about current events during the coffee break.

I had the pleasure of two other very good Postdocs throughout my PhD

that I am extremely grateful for: Dr. Raphaëlle Delagrangé and Dr. Malin Nilsson. Both of you have helped guide me through the day-to-day work guidance throughout the my PhD. Thank you!

I am very thankful for all the hard work that went into creating the high quality nanowires we received by our colleagues, Lucia Sorba and Valentina Zannier, at NEST in Pisa. This thesis would not have been possible without them.

A few people gladly volunteered to the please of proofreading this thesis: Dr. Andreas Baumgartner, Dr. Christian Jünger, Dr. Malin Nilsson, Alessia Pally, and Carlo Ciaccia. I am extremely grateful for them taking the time to find the mistakes written in this thesis.

I would also like to thank Arunav Bordoloi and Dr. Christian Jünger for their scientific help throughout my PhD. Both were always available when I had trouble during fabrication or with small problems with the measurement. Also Dr. Gergő Fülöp and Dr. Joost Ridderbos for all the time they spent working on QCodes for our group.

I am extremely thankful for all of the friendships that I have made over the last four years with my colleagues. Dr. Christian Jünger and I spent countless hours enjoying Basel and life. Arunav Bordoloi and I shared a lot of time outside of the lab and had a great time skiing in Kandersteg. Hopefully, we can do it again next year. David Indolese and I spent a wonderful two weeks in Cargèse in the beginning of our PhDs. A postcard of our time together there will probably hang on the wall of our office for eternity. I am also very thankful for Dr. Lujun Wang, Roy Haller, Martin Endres, Dr. Dennis Chevallier, Alessia Pally, and Carlo Ciaccia. It was great spending time together with y'all outside of the lab. The PhD life would not have been the same without you and I am thankful to consider you good friends.

Furthermore, I would like to thank all former and current members of the Nanoelectronics group: Simon Zihlmann, Gergő Fülöp, Jörg Gramich, Thomas Hasler, Clevin Handschin, Vishal Ranjan, Kishan Todkar, Gulibusitan Abulizi, Peter Makk, Maria El Abbassi, Mihai-Cezar Harabula, Jann Overbeck, Anton Vladyka, Michel Calame, Artem Kononov, Blesson Varghese, Luk Yi Cheung, Ian Correa Sampaio, Olivier Faist, Lukas Gubser, Zarina Mingazheva, Mehdi Ramezani, Jann Ungerer, Dario Sufra, Melissa Osterwalder, Blesson-sam Varghese, Libin Wang, Han Zheng, and Matthijs Hermans.

There are many people behind the scenes at the Physics department whom without their help and support this would not have been possible. Barbara Kammerrmann and Astrid Kalt were extremely helpful with administrative work. I am thankful for Dominik Sifrig for taking care of the helium supply for the entire department. I am especially thankful to Sascha Martin and his team at the mechanical workshop and Daniel Sacker for the help with fixing machines.

I also thank everyone at Curling Club Aarau for welcoming me into their

club and all the friends that I met there. I thank Sandra Popp, Regula Schär, and Laurence Bidaud, as well as my team: Thomas Isenring, Marianne Eichenberger, and Sandra Wehrt.

This thesis would not have been possible without all my childhood friends I met way back: Dr. med. Matthew Kaufman, Zack Neeld, and Viet Le.

I also thank Robert Egger for always being by my side throughout the last four years.

I am very grateful to my parents, Patricia and Todd Thomas, and my sisters, Heather Caudill and Kristin Thomas, for their unlimited support in all aspects throughout my life.

Without all these people I would not be where I am today.